

1996

## Variational inverse methods for transport problems

Zhaoqing Yang

*College of William and Mary - Virginia Institute of Marine Science*

Follow this and additional works at: <https://scholarworks.wm.edu/etd>



Part of the [Environmental Sciences Commons](#), and the [Oceanography Commons](#)

---

### Recommended Citation

Yang, Zhaoqing, "Variational inverse methods for transport problems" (1996). *Dissertations, Theses, and Masters Projects*. William & Mary. Paper 1539616917.

<https://dx.doi.org/doi:10.25773/v5-48qc-5348>

This Dissertation is brought to you for free and open access by the Theses, Dissertations, & Master Projects at W&M ScholarWorks. It has been accepted for inclusion in Dissertations, Theses, and Masters Projects by an authorized administrator of W&M ScholarWorks. For more information, please contact [scholarworks@wm.edu](mailto:scholarworks@wm.edu).

## INFORMATION TO USERS

This manuscript has been reproduced from the microfilm master. UMI films the text directly from the original or copy submitted. Thus, some thesis and dissertation copies are in typewriter face, while others may be from any type of computer printer.

**The quality of this reproduction is dependent upon the quality of the copy submitted.** Broken or indistinct print, colored or poor quality illustrations and photographs, print bleedthrough, substandard margins, and improper alignment can adversely affect reproduction.

In the unlikely event that the author did not send UMI a complete manuscript and there are missing pages, these will be noted. Also, if unauthorized copyright material had to be removed, a note will indicate the deletion.

Oversize materials (e.g., maps, drawings, charts) are reproduced by sectioning the original, beginning at the upper left-hand corner and continuing from left to right in equal sections with small overlaps. Each original is also photographed in one exposure and is included in reduced form at the back of the book.

Photographs included in the original manuscript have been reproduced xerographically in this copy. Higher quality 6" x 9" black and white photographic prints are available for any photographs or illustrations appearing in this copy for an additional charge. Contact UMI directly to order.

# UMI

A Bell & Howell Information Company  
300 North Zeeb Road, Ann Arbor MI 48106-1346 USA  
313/761-4700 800/521-0600



**VARIATIONAL INVERSE METHODS FOR TRANSPORT PROBLEMS**

---

**A Dissertation**

**Presented to**

**The Faculty of the School of Marine Science**

**The College of William and Mary**

**In Partial Fulfillment**

**Of the Requirements for the Degree of**

**Doctor of Philosophy**

---

**by**

**Zhaoqing Yang**

**1996**

**UMI Number: 9709107**

---

**UMI Microform 9709107**  
**Copyright 1996, by UMI Company. All rights reserved.**

**This microform edition is protected against unauthorized  
copying under Title 17, United States Code.**

---

**UMI**  
**300 North Zeeb Road**  
**Ann Arbor, MI 48103**

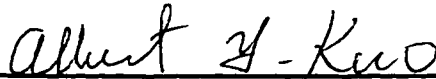
**APPROVAL SHEET**

**This dissertation is submitted in partial fulfillment of  
the requirements for the degree of  
Doctor of Philosophy**

---

**Zhaoqing Yang**

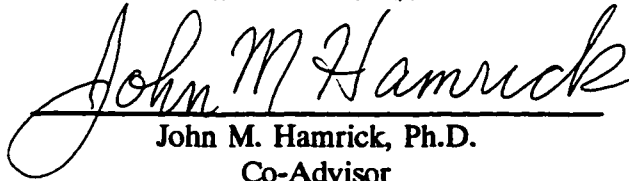
**Approved, August 1996**



---

**Albert Y. Kuo, Ph.D.**

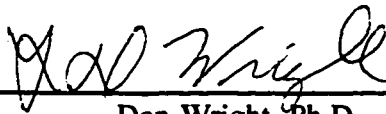
**Committee Chairman/Advisor**



---

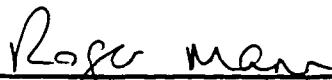
**John M. Hamrick, Ph.D.**

**Co-Advisor**



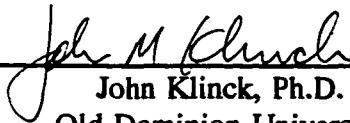
---

**Don Wright, Ph.D.**



---

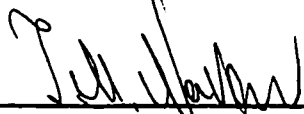
**Roger Mann, Ph.D.**



---

**John Klinck, Ph.D.**

**Old Dominion University  
Norfolk, Virginia**



---

**Michael I. Navon, Ph.D.**

**Florida State University  
Tallahassee, Florida**

*In Memory of My Father...*

## TABLE OF CONTENTS

|  | Page |
|--|------|
| ACKNOWLEDGMENT .....   | vii  |
| LIST OF TABLES .....   | viii |
| LIST OF FIGURES .....  | ix   |
| LIST OF SYMBOLS .....  | xiv  |
| ABSTRACT.....  | xvii |
| 1 INTRODUCTION .....   | 2    |
| 2 THE GENERIC INVERSE PROBLEM FOR TRANSPORT MODELS .....         | 9    |
| 3 THE TRACER INVERSE PROBLEM                                     |      |
| 3.1 Introduction .....   | 12   |
| 3.2 Governing Equation for The Long-Term Transport Problem ..... | 15   |
| 3.3 Adjoint Model And Gradient of The Cost Function .....        | 18   |
| 3.4 Descent Algorithms .....                                     | 23   |
| 3.5 Model Tests in An Idealized Vertical 2-D Estuary .....       | 25   |
| 3.5.1 Model Setup .....  | 25   |
| 3.5.2 Basic Experiment .....                                     | 28   |
| 3.5.3 Experiments with Sparse Data .....                         | 30   |
| 3.5.4 Experiments with Noisy Data .....                          | 32   |
| 3.6 Some Discussion on The 3-D Problem .....                     | 32   |
| 3.7 Conclusions .....  | 36   |



## 4 DETERMINATION OF THE TRACER OPEN

|   |    |
|---|----|
| BOUNDARY CONDITION .....                                  | 51 |
| 4.1 Introduction .....                                    | 51 |
| 4.2 Model Description .....                               | 53 |
| 4.3 Adjoint Model And Gradient of The Cost Function ..... | 54 |
| 4.4 Model Tests in An Idealized 3-D Estuary .....         | 56 |
| 4.4.1 Model Setup .....                                   | 56 |
| 4.4.2 Scaling And Preconditioning .....                   | 59 |
| 4.4.3 Test with Initial Guess I .....                     | 61 |
| 4.4.4 Test with Initial Guess II .....                    | 63 |
| 4.5 Conclusions And Future Studies .....                  | 64 |

## 5 PARAMETER ESTIMATION IN A COHESIVE

|   |     |
|---|-----|
| SEDIMENT TRANSPORT MODEL .....                            | 83  |
| 5.1 Introduction .....                                    | 83  |
| 5.2 Sediment Transport Models .....                       | 86  |
| 5.3 Adjoint Model and Gradient of The Cost Function ..... | 90  |
| 5.4 Model Tests in An Idealized 3-D Estuary .....         | 93  |
| 5.4.1 Forward Problem .....                               | 93  |
| 5.4.2 Inverse Problem .....                               | 95  |
| 5.5 Model Application in The James River .....            | 109 |
| 5.5.1 Physical Background of The James River.....         | 109 |
| 5.5.2 Numerical Model Setup .....                         | 110 |

|   |     |
|---|-----|
| 5.5.3 Modeling Hydrodynamics and Sediment Transport ..... | 111 |
| 5.5.4 Inverse Experimental Results .....                  | 114 |
| 5.6 Conclusions and Future Studies .....                  | 115 |
| 6 SUMMARY AND FUTURE STUDIES .....                        | 135 |
| LITERATURE CITED .....                                    | 140 |
| VITA .....  | 150 |

## ACKNOWLEDGMENT

First I like to express my great appreciation to my dissertation co-advisor Dr. John M. Hamrick for his continuous guidance on the research, especially his tireless help for using the VIMS 3-D Environmental Fluid Dynamic Code (EFDC). Without his friendly help and advise, this dissertation would not be finished by this time. I also thank my advisor Dr. Albert Kuo, for his many helpful advices, and administration effort in the final stage of the completion of this dissertation. Dr. Michael Navon is especially thanked for kindly providing the minimization subroutine and useful comments on the data assimilation aspect. I like to thank Dr. Klinck for his many valuable comments on this study. Thanks also go to Dr. Wright for his supportive suggestions on the sediment transport part and to Dr. R. Mann for taking time to serve on the dissertation committee. I am very grateful for all the committee members to review the manuscript. I would like to thank Nancy Wilson, Buddy Matthew, Suzanne Alexander and other members of the computer center for their help and support in my using the computer facilities. Also, many thanks extend to Mac Sisson, Jian Shen, Sarah Rennie and many other VIMS fellows for their warm friendship and help.

Finally, special thank goes to my wife, Hong Li, for her long time support and deep understanding throughout this research.

## LIST OF TABLES

| Table  | Page |
|--|------|
| 1. Verification of the gradient of the cost function .....   | 38   |
| 2. Initial salinity misfits (initial guess I) .....  | 67   |
| 3. Final salinity misfits without penalty (initial guess I) .....                                  | 67   |
| 4. Final salinity misfits with penalty (initial guess I) .....                                     | 67   |
| 5. Initial salinity misfits (initial guess II) .....   | 68   |
| 6. Final salinity misfits without penalty (initial guess II) .....                                 | 68   |
| 7. Final salinity misfits with penalty (initial guess II) .....                                    | 68   |
| 8. Comparisons of parameters in cohesive sediment transport models used in the<br>literature ..... | 98   |
| 9. Physical and hydrodynamic characteristics of the James River estuary .....                      | 118  |

## LIST OF FIGURES

| Figure  | Page |
|---|------|
| 1. Schematic of the geometry of an idealized estuary .....  | 39   |
| 2. Variation of function $\Phi(\alpha)$ .....   | 40   |
| 3. Residual of function $\Phi(\alpha)$ .....  | 40   |
| 4. True solution of y-component of vector potential $A_y$ (m <sup>3</sup> /s) .....   | 41   |
| 5. Distribution of vector potential transport field (m/s) .....   | 41   |
| 6. Distribution of the Eulerian mean transport field (m/s) .....  | 42   |
| 7. Distribution of the Lagrangian mean transport field (m/s) .....  | 42   |
| 8. Distribution of 'observed' salinity (ppt) .....  | 43   |
| 9. Distribution of initial salinity (ppt) .....   | 43   |
| 10. Initial salinity misfit (ppt) for basic model test ( <i>case 1</i> ) .....  | 44   |
| 11. Variations of $\ J_\pi/J_0\ $ and $\ \nabla J_\pi/\nabla J_0\ $ in terms of number of iterations .....  | 44   |
| 12. Final estimated $A_y$ for <i>case 1</i> .....   | 45   |
| 13. Final distribution of error ( $E_{t,k}$ ) of estimated $A_y$ for <i>case 1</i> .....  | 45   |
| 14. Final salinity misfit (ppt) for <i>case 1</i> .....   | 46   |
| 15. Distribution of the advection term due to $A_y$ .....   | 46   |
| 16. Final estimated $A_y$ for <i>case 2</i> without including a penalty term .....  | 47   |
| 17. Final estimated $A_y$ for <i>case 2</i> with a penalty $\beta=0.1$ .....  | 47   |
| 18. Comparisons of the final estimated $A_y$ along the river at mid-level for <i>case 2</i><br>with different values of penalty coefficient $\beta$ : long dashed line for true |      |

|  |    |
|--|----|
| solution; solid line for $\beta=0$ ; dashed and dotted line for $\beta=0.01$ ; dotted line<br>for $\beta=0.1$ ; short dashed line for $\beta=10$ .....   | 48 |
| 19. Final estimated $A_y$ for <i>case 3</i> without including a penalty term .....   | 49 |
| 20. Final estimated $A_y$ for <i>case 3</i> with a penalty $\beta=10$ .....  | 49 |
| 21. Comparisons of the final estimated $A_y$ along the river at mid-level for <i>case 3</i><br>with different values of penalty coefficient $\beta$ : long dashed line for true<br>solution; solid line for $\beta=0$ ; dashed and dotted line for $\beta=1$ ; dotted line for<br>$\beta=10$ ; short dashed line for $\beta=100$ ..... | 50 |
| 22. Specification of salinity open boundary condition .....  | 69 |
| 23. Depth profiles at the head (a) and at the mouth (b) .....  | 70 |
| 24. Schematic of a 3-D idealized estuary .....   | 71 |
| 25. Horizontal physical grid of the 3-D idealized estuary .....  | 72 |
| 26. “Observed” salinity distribution (ppt) at four tidal phases<br>(T/4, T/2, 3T/4 and T) along the axis of the estuary channel .....  | 73 |
| 27. “Observed” salinity distribution (ppt) at four tidal phases<br>(T/4, T/2, 3T/4 and T) at the cross section I=50 .....  | 74 |
| 28. Variations of $\ J_r/J_0\ $ and $\ \nabla J_r/\nabla J_0\ $ without penalty (initial guess I) .....  | 75 |
| 29. Variations of the maximum salinity boundary value $C_{bmax}$ (a) and the recovery<br>time $t_R$ (b) without penalty (initial guess I) at grid cell $G_1$ (dashed),<br>$G_2$ (dotted) and $G_3$ (solid) .....   | 76 |
| 30. Variations of $\ J_r/J_0\ $ and $\ \nabla J_r/\nabla J_0\ $ with penalty (initial guess I) .....   | 77 |
| 31. Variations of the maximum salinity boundary value $C_{bmax}$ (a) and the recovery  |    |

|   |     |
|---|-----|
| time $t_R$ (b) with penalty (initial guess I) at grid cell $G_1$ (dashed),<br>$G_2$ (dotted) and $G_3$ (solid) .....  | 79  |
| 32. Variations of $\ J_r/J_0\ $ and $\ \nabla J_r/\nabla J_0\ $ without penalty (initial guess II) .....  | 79  |
| 33. Variations of the maximum salinity boundary value $C_{bmax}$ (a) and the recovery<br>time $t_R$ (b) without penalty (initial guess II) at grid cell $G_1$ (dashed),<br>$G_2$ (dotted) and $G_3$ (solid) ..... | 80  |
| 34. Variations of $\ J_r/J_0\ $ and $\ \nabla J_r/\nabla J_0\ $ with penalty (initial guess II) .....   | 81  |
| 35. Variations of the maximum salinity boundary value $C_{bmax}$ (a) and the recovery<br>time $t_R$ (b) with penalty (initial guess II) at grid cell $G_1$ (dashed),<br>$G_2$ (dotted) and $G_3$ (solid) .....    | 82  |
| 36 “Observed” suspended sediment distribution (mg/l) at four tidal phases<br>(T/4, T/2, 3T/4 and T) along the axis of the estuary channel .....   | 99  |
| 37. “Observed” suspended sediment distribution (mg/l) at four tidal phases<br>(T/4, T/2, 3T/4 and T) at the cross section I=25 .....  | 100 |
| 38. The Lagrangian mean velocity (m/s) at the cross section I=25: longitudinal<br>component (a) and transverse component (b) .....  | 101 |
| 39. Mean salinity distribution (ppt) at the cross section I=25 .....  | 102 |
| 40. Initial suspended sediment distribution (mg/l) at four tidal phases (T/4, T/2,<br>3T/4 and T) along the axis of the estuary channel (initial guess I) .....   | 103 |
| 41. Variations of $\ J_r/J_0\ $ and $\ \nabla J_r/\nabla J_0\ $ (initial guess I) .....   | 104 |
| 42. Variations of settling velocity $w_s$ (a) and erosion constant $M_o$ (b)<br>(initial guess I) .....   | 105 |

|  |     |
|--|-----|
| 43. Initial suspended sediment distribution (mg/l) at four tidal phases (T/4, T/2, 3T/4 and T) along the axis of the estuary channel (initial guess II) .....      | 106 |
| 44. Variations of $\ J_r/J_o\ $ and $\ \nabla J_r/\nabla J_o\ $ (initial guess II) .....   | 107 |
| 45. Variations of settling velocity $w_s$ (a) and erosion constant $M_o$ (b) (initial guess II) .....  | 108 |
| 46. Location of the James River estuary in the Chesapeake Bay region .....   | 119 |
| 47. Grid map of the James River model .....  | 120 |
| 48. "Observed" surface salinity distribution (ppt) in the James River at four tidal phases (T/4, T/2, 3T/4, T) .....   | 121 |
| 49. "Observed" bottom salinity distribution (ppt) in the James River at four tidal phases (T/4, T/2, 3T/4, T) .....  | 122 |
| 50. Surface salinity distribution in the James River at high water (left panel) and low water (right panel) on 2 September 1950 (from D. W. Pritchard, 1952) ..... | 123 |
| 51. Calculated vertical profile of salinity (ppt) at phase before flood at the mouth in the James River .....  | 124 |
| 52. Observed vertical profile of salinity (ppt) at slack water before flood in the James River in June 19, 1985 (from Hepworth and Kuo, 1989) .....                | 125 |
| 53. "Observed" surface suspended sediment distribution (mg/l) in the James River at four tidal phases (T/4, T/2, 3T/4, T) .....                                    | 126 |
| 54. "Observed" bottom suspended sediment distribution (mg/l) in the James River at four tidal phases (T/4, T/2, 3T/4, T) .....                                     | 127 |



|  |     |
|--|-----|
| 55. Surface Eulerian mean velocity (cm/s) in the James River .....   | 128 |
| 56. Bottom Eulerian mean velocity (cm/s) in the James River .....  | 129 |
| 57. Patterns of deposition and erosion in the James River estuary determined from<br>depth change over a 70-year period (from M. M. Nichols, 1972) ..... | 130 |
| 58. Variations of $\ J_{\pi}/J_0\ $ and $\ \nabla J_{\pi}/\nabla J_0\ $ (initial guess I) .....  | 131 |
| 59. Variations of settling velocity $w_s$ (a) and erosion constant $M_o$ (b)<br>(initial guess I) .....  | 132 |
| 60. Variations of $\ J_{\pi}/J_0\ $ and $\ \nabla J_{\pi}/\nabla J_0\ $ (initial guess II) .....   | 133 |
| 61. Variations of settling velocity $w_s$ (a) and erosion constant $M_o$ (b)<br>(initial guess II) .....   | 134 |

## LIST OF SYMBOLS

|   |  |
|---|--|
| $C$   | Tracer concentration   |
| $\langle C \rangle$                                       | Long-term tracer concentration                                     |
| $H$   | (= $h+\zeta$ ) Total water depth                                   |
| $h$   | Still water depth  |
| $\zeta$   | Free surface elevation   |
| $\langle H \rangle$                                       | Time-average mean of $H$   |
| $H'$  | Zero-mean total water depth fluctuation ( $=H-\langle H \rangle$ ) |
| $m_x, m_y$  | Horizontal coordinate scales                                       |
| $D_H$   | Horizontal diffusion coefficient                                   |
| $D_v$   | Vertical diffusion coefficient                                     |
| $\langle D_v \rangle$                                     | Time-average mean of $D_v$   |
| $u, v, w$   | Instantaneous Eulerian velocity                                    |
| $\langle u \rangle, \langle v \rangle, \langle w \rangle$ | Time-average mean of $u, v, w$                                     |
| $u', v', w'$  | Zero-mean velocity fluctuations after time averages are removed    |
| $u_{ET}, v_{ET}, w_{ET}$                                  | Eulerian mean transport velocity                                   |
| $u_m, v_m, w_m$   | Lagrangian mean transport velocity                                 |
| $A_x, A_y, A_z$   | Vector potential   |
| $J$   | Cost function  |
| $\nabla J$  | Gradient of the cost function                                      |
| $L$   | The Lagrange function  |

|                           |  |
|---------------------------|--|
| $\lambda$                 | The Lagrange multiplier  |
| $C^{obs}$                 | Observation of tracer $C$  |
| $B$                       | Observation operator   |
| $W$                       | Weight matrix  |
| $\varepsilon$             | Convergence criterion parameter  |
| $\phi$                    | Scalar function for checking the correctness of the gradient                               |
| $\chi, \psi$              | Scalar functions introduced in the decomposition of the Lagrangian mean transport velocity |
| $\alpha$                  | parameter for gradient checking  |
| $E_{L,k}$                 | Error of the Estimated $A_y$ defined by Eq.(36)  |
| $\beta, \beta_1, \beta_2$ | Penalty coefficient  |
| $C_b$                     | Tracer concentration at open boundary  |
| $C_E$                     | Tracer concentration at slack water after ebb at open boundary                             |
| $C_{bmax}$                | Maximum inflow tracer concentration at open boundary                                       |
| $t_R$                     | Recovery time for inflow tracer concentration at open boundary condition                   |
| $t_E$                     | Time at slack water after ebb  |
| $t_F$                     | Time at slack water after flood  |
| $B_o$                     | Surface width of the idealized 3-D estuary   |
| $h_c$                     | Still water depth at the center of the channel of the idealized 3-D estuary                |
| $h_s$                     | Still water depth at both sides of the idealized 3-D estuary                               |
| $\Delta t$                | time step  |
| $N_R$                     | number of time step for the recovery of inflow tracer concentration at open                |

boundary condition ( $N_R = t_R / \Delta t$ )

|             |  |
|-------------|--|
| $M_o$       | Resuspension constant                  |
| $w_s$       | Settling velocity                      |
| $\tau$      | Bottom shear stress                    |
| $\tau_{cd}$ | Critical shear stress for deposition   |
| $\tau_{cr}$ | Critical shear stress for resuspension |

## ABSTRACT

Variational inverse data assimilation schemes are developed for three types of parameter identification problems in transport models: 1) the tracer inverse for the Lagrangian mean transport velocity in a long-term advection-diffusion transport model; 2) determination of inflow salinity open boundary condition in an intra-tidal salinity transport model and 3) determination of settling velocity and resuspension rate for a cohesive sediment transport model. A limited-memory quasi-Newton conjugate gradient algorithm is used in the minimization processes. The gradient of the cost function with respect to the control variables is obtained by the adjoint model. A series of twin experiments are conducted to test the inverse models for the three types of problems. Results show that variational data assimilation can successfully retrieve poorly known parameters in transport models.

The first problem is associated with the long-term advective transport, represented by the Lagrangian mean transport velocity which can be decomposed into two parts: the Eulerian transport velocity and the curl of a 3-D vector potential  $A$ . The vector potential  $A$  is treated as a poorly known parameter in the long-term transport model and the optimal long-term advection transport field is obtained through adjusting the vector potential using a variational data assimilation method to best fit the model output to the observation data. Experiments are performed in an idealized estuary. Observation data are generated at every grid point and assumed to be perfect. Results show that the variational data assimilation method can successfully retrieve the effective Lagrangian mean transport velocity in a long-term transport model. Results also show that the smooth best fit model state can still be retrieved using a penalty method when observations are too sparse or contain noisy signals.

A variational inverse model for optimally determining open boundary condition is developed and tested in a 3-D intra-tidal salinity transport model. The maximum inflow salinity open boundary value and its recovery time from outflow condition are treated as control variables. Effects of scaling, preconditioning and penalty are investigated. It is shown that proper scaling and preconditioning can greatly speed up the convergence rate of the minimization process. The spatial oscillations in the recovery time of the inflow boundary condition can be effectively eliminated by an penalty technique.

In modeling of cohesive sediment transport problems, one of the major difficulties is to determine the settling velocity, resuspension rate and the critical shear stresses for erosion and deposition. A variational inverse model is developed to estimate the settling velocity and resuspension constant. The settling velocity  $w_s$  and resuspension constant  $M_o$  are assumed to be constant in the whole model domain. The inverse model is tested in an idealized 3-D estuary and the James River, a tributary of the Chesapeake Bay. Experimental results demonstrate that the variational inverse model can be used to identify the poorly known parameters in cohesive sediment transport modeling.

## **VARIATIONAL INVERSE METHODS FOR TRANSPORT PROBLEMS**

## 1. INTRODUCTION

Variational inverse data assimilation is a process which combines information from field observations with equations of a dynamical model to yield better estimates of the model parameters and simultaneously improve the model state. It is based on the theory of optimal control of distributed parameters in partial differential equations. Variational inverse data assimilation methods have been widely used in meteorology forecast models for many years since Sasaki (1955, 1958, 1970) first introduced the idea to the area of meteorology, *e.g.*, Hoffman (1986), Harland and O'Brien (1986), Talagrand and Courtier (1987), Derber (1985, 1987), Lewis and Derber (1985), Navon (1986), Navon *et al.* (1992), Le Dimet and Talagrand (1986), Zou *et al.* (1992a, 1993). The goal of data assimilation in meteorology is to obtain the best estimation of the initial condition for the weather forecasting models. Although data assimilation has long been used in numerical weather forecasting, it has only attracted attention in oceanography in recent years. There have been a great number of applications of variational data assimilation methods in oceanography coinciding with the development of advanced observation techniques (Wunch, 1978; Provost and Salmon, 1986; Tziperman and Thacker, 1989; Yu and O'Brien, 1991; Brasseur, 1991; Ezer and Mellor, 1993; Schlitzer, 1993; Lardner and Das, 1994). One of the ways that oceanography may differ from weather forecasting is that there is less emphasis on ocean forecasting. To a considerable extent, the role of data assimilation in the ocean may be more as a means of obtaining information about uncertain parameters and the deeper structure of ocean physics.

The earliest sophisticated data assimilation models in oceanography could be found in Stommel and Schott's (1977) beta spiral method for determining the absolute velocity field and Wunsch's (1978) inverse method for determining the north Atlantic mean large-scale circulation. Wunsch (1985) demonstrated that the interpretation of the solution to an underdetermined problem is possible if inverse procedures are applied. In his study, the flow fields and mixing rates from chemical tracer distributions in an ideal rectangular channel were determined. McIntosh and Veronis (1993) also showed that mass conservation equations can be inverted to determine the large scale steady-state ocean flow field from the known tracer distributions by using inverse methods. Brasseur (1991) reconstructed the continuous fields of the general circulation using a variational inverse model based on the local measurement such as CTD profiles. Horizontal distributions of temperature, salinity, nutrients, chlorophyll and other chemical tracers, as well as the horizontal transport of water are constructed by using synoptic data. A variational data assimilation formalism for fitting dynamic forecast models to data was described by Thacker and Long (1988). It showed how surface elevation and wind stress observations might be used to recover the model state. Thacker and Long discussed whether the meager synoptic observations are sufficient to determine the fit and concluded that observational systems must be designed so that every event is sampled somewhere in time and such widespread coverage of the oceans requires a data collection system which relies heavily on satellites. Hurlburt (1986) used a two-active layer, free surface primitive equation model on a  $\beta$ -plane to investigate the dynamic transfer of surface to subsurface information. Perfect altimeter data were simulated by the free surface of the



two layer model. The results showed that the maximum update interval that provided success was about half the shortest major time scale in the model. Provost and Salmon (1986) presented a variational technique for estimating the three-dimensional field of geostrophic velocity from hydrographic station data (temperature and salinity). They determined the smoothest velocity field which is consistent with the data and the selected prescribed misfits. These misfits represent errors in the observations and in the approximated dynamical constraints. The admission of the errors necessitates the choice of weights. By varying the misfits relative to one another in their respective admissible ranges, the full envelope of physically plausible estimates of geostrophic flow is explored. Smedstad and O'Brien (1991) developed a variational data assimilation and parameter estimation method for a reduced gravity model applied to the equatorial Pacific Ocean. In their model, the phase speed is used as a controlled parameter and an optimal spatial structure giving the best fit of the model prediction to the observation data is determined. Marshall (1985) used estimation theory to assimilate simulated data from satellite altimetry into an ocean model and improve the geoid. Using altimeter observations of the ocean surface, Webb and Moor (1986) investigated projection methods of estimation theory to determine the deeper structure of the ocean. The result of their study was that the determination of the deeper structure of the ocean was limited by the phase separation that develops over each assimilation cycle between modes of the ocean with the same horizontal wave number but differing vertical structure. Malanotte-Rizzoli and Holland (1986) used a quasi-geostrophic general circulation model to investigate the effect of data insertion into a numerical model, and also demonstrated how the dynamics spread the

inserted information to different regions. Malanotte-Rizzoli and Holland (1988) extended their results from the 1986 paper to the transient eddy-resolving case. It is shown that in the transient case a single data section is very ineffective to drive the model towards the reference ocean over time scales of about 100 days. Derber and Rosati (1989) developed a global oceanic data assimilation system for use in initializing coupled ocean-atmosphere general circulation models. Data of conventional sea surface temperature observations and vertical temperature profiles are inserted into the model continuously by updating the model's temperature solution every timestep. Schroter and Wunsch (1986) studied the effect of observational errors in the driving of the models. From their algorithm it is possible to calculate the qualitative sensitivity of the objective function to change in the data errors and to find an optimization technique capable of dealing with data uncertainty. In the paper by Thacker (1988), the process of fitting a model to inadequate data is discussed and results show that for the simple three wave model (Thacker and Long, 1988), a reasonable fit can be obtained even if the number of observations is less than the number of the degrees of freedom of the model. A three-dimensional data assimilation scheme is developed and tested using Geosat altimeter data and the Princeton Ocean Model (POM) in the Gulf Stream region (Ezer & Mellor, 1993). The assimilation scheme is based on an optimal interpolation approach in which data along satellite tracks are continuously interpolated into the model grid and assimilated with model prognostic fields. Experiments showed that at sea surface, the error of temperature anomalies is greatly reduced due to the assimilation of SST (Sea Surface Temperature) and deeper than 100 m, the error is reduced due to the assimilation of SSH

(Sea Surface Height).

Even though numerical general circulation models (GCM) have become quite sophisticated in recent years, many parameters for the models are still poorly known, such as eddy-mixing coefficients, surface forcing by heat and momentum fluxes, and boundary tracer fluxes. Recently, there have been some developments in the variational inverse data assimilation in general circulation models which show that inverse methods can successfully improve the model state and reduce the errors of the model outputs from the observations (Tziperman and Thacker, 1989; Marotzke and Wunsch, 1993; Tziperman, *et al.*, 1992a & 1992b). Yu and O'Brien (1991) used the adjoint method to estimate the vertical eddy viscosity and wind stress drag coefficient from data in a wind-forced Ekman layer. Schroter (1989) developed a simple algorithm (adjoint method) to reduce a chosen cost function toward a smaller value that nevertheless might not be a minimum. It was shown that the adjoint method could be used to provide sensitivity analysis for complicated, time dependent non-linear models. Schlitzer (1993) developed an adjoint formalism to obtain the mean, large scale ocean circulation together with coefficients of iso- and diapycnal mixing and air-sea heat and freshwater fluxes based on the adjoint formalism to assimilate large sets of hydrographic data into the model. In his model, the flow fields, air-sea fluxes and mixing coefficients are forced to reproduce the observed distribution of temperature and salinity, and also the vertical velocity shear of the horizontal flows is required to be close to the vertical shear of the initial geostrophic profile. The optimal model solution is obtained iteratively starting with geostrophic horizontal flows which are calculated from the initial guess of dynamic heights. This

method is a new approach to the classical problem of determining the reference velocity left unknown by pure geostrophic calculations. Moore (1991) applied the adjoint data assimilation method in a quasi-geostrophic (QG) open-ocean model of the Gulf Stream region to determine the initial condition. It is shown that the adjoint data assimilation scheme has the ability to correct for large error in the speed and position of the Gulf Stream jet when simulated AXBT and satellite altimeter observations are assimilated into the QG model.

In contrast to numerous applications of variational inverse methods in meteorology and the problem of re-constructing large scale oceanic mean circulation patterns, there are not many applications of inverse methods in estuarine and coastal hydrodynamic models. Bennett and McIntosh (1982) used a weighted variational method in the investigation of tidal motion. Their results show that the choice of data weights is of great importance. Panchang and O'Brien (1988) determined friction factors and water depth in tidal channels in hydraulic model using adjoint method. Das and Lardner (1991) estimated parameters in a two-dimensional numerical tidal model by assimilation of periodic tidal data. The parameters to be estimated are bottom friction coefficient and water depth which are assumed to be spatially dependent. It is shown that a satisfactory numerical minimization can be completed using a quasi-Newton algorithm or the truncated Newton algorithm. Panchang and Richardson (1993) used adjoint inverse methods to estimate the vertical eddy viscosity in a three-dimensional coastal circulation model. The cost function they constructed consists of two terms: one describes the misfit between the model results and available data and the other measures the variance of the

eddy viscosity with depth. The later term is introduced with a view to eliminate the instabilities commonly associated with inverse methods. Reviews of variational data assimilation in meteorology and oceanography have been presented by Le Dimet and Navon (1988), Ghil and Malanotte-Rizzoli (1991) and Bennett (1992).

To date, very few applications have been directed towards to constructing Lagrangian mean velocity and many other model parameters in coastal and estuarine transport problems. The objective of this study is to develop variational inverse schemes for parameter identification for three different types of transport problems: 1) the tracer inverse for determining the Lagrangian mean transport velocity in a long-term advection-diffusion transport model; 2) determination of inflow salinity open boundary condition in an intra-tidal salinity transport model and 3) determination of settling velocity and resuspension rate for a cohesive sediment transport problem. The structure of the dissertation is arranged as follows. The generic inverse problem for transport models is described in Chapter 2. The tracer inverse problem for Lagrangian mean transport velocity is presented in Chapter 3. The determination of inflow salinity open boundary condition and the parameter estimation in cohesive sediment transport problem are investigated in Chapter 4 and Chapter 5, respectively. Summary and future studies are given in Chapter 6.

## 2. THE GENERIC INVERSE PROBLEM FOR TRANSPORT MODELS

In transport problems, the tracer field is constrained to satisfy the transport equation and the transport flow field is subject to the mass conservation constraint. The intra-tidal biogeochemical transport equation for a conservative tracer  $C_i$  with settling velocity  $w_{s,i}$  can be described by a Reynold's averaged advection-diffusion equation (in horizontal curvilinear-orthogonal and vertical sigma stretched coordinates):

$$\begin{aligned}
 & \partial_t (mHC_i) + \partial_x (m_y Hu C_i) + \partial_y (m_x H v C_i) + \partial_z (m w C_i) \\
 & = \partial_x (m_y m_x^{-1} H D_H \partial_x C_i) + \partial_y (m_x m_y^{-1} H D_H \partial_y C_i) \\
 & + \partial_z (m H^{-1} D_V \partial_z C_i) + \partial_z (m w_{s,i} C_i) + m H Q_i
 \end{aligned} \tag{1}$$

where  $C_i$  represents the concentration of type  $i$  tracer,  $Q_i$  represents the rate of source or sink terms.  $m_x$  and  $m_y$  are the coordinate scale factors and  $m = m_x m_y$ .  $H = \zeta + h$  is the water column depth ( $\zeta$  is the free surface elevation and  $h$  is the still water depth).  $u$ ,  $v$  and  $w$  are three components of the instantaneous Eulerian velocity field.  $D_H$  and  $D_V$  are the horizontal and vertical turbulent diffusivities, respectively. The velocity field ( $u$ ,  $v$ ,  $w$ ) must satisfy the continuity equation:

$$\partial_t (mH) + \partial_x (m_y H u) + \partial_y (m_x H v) + \partial_z (m w) = 0 \tag{2}$$

The governing equation (1) is also subject to tracer boundary conditions and initial conditions if problems are transient.

In order to model transport processes in estuarine and coastal waters correctly, the

following information should be provided: 1) hydrodynamics (*i.e.*, transport flow field); 2) initial/boundary conditions and 3) model parameters, such as  $D_H$ ,  $D_V$ ,  $w_{si}$  and  $Q_i$ . In an intra-tidal transport model, the transport flow field ( $u$ ,  $v$ ,  $w$ ) and diffusivities ( $D_H$ ,  $D_V$ ) generally can be obtained from outputs of a hydrodynamic model and turbulence closure model in the same modeling domain. However, the input of boundary conditions and model parameters strongly rely on field observations, previous knowledge and laboratory experiments. Poorly known parameters may vary over a wide range in real applications for different modeling domains. If ( $u$ ,  $v$ ,  $w$ ),  $D_H$  and  $D_V$  are all known, then with the information of a single type tracer  $C_i$ , we can determine the tracer open boundary conditions by variational inverse methods with Eq. (1). For cohesive sediment transport problems, the poorly known parameters are settling velocity  $w_{si}$ , erosion constant  $M_o$ , critical shear stresses for deposition  $\tau_{cd}$  and for erosion  $\tau_{cr}$ . Theoretically,  $w_{si}$  can vary in the whole spatial domain, *i.e.*, every grid cell in horizontal and vertical, while  $M_o$ ,  $\tau_{cd}$  and  $\tau_{cr}$  can vary at every horizontal grid cell. In order to determine a unique solution, the number of independent observation of tracer  $C_i$  must be equal to or greater than the number of parameters to be estimated (Gill *et al.*, 1981; Thacker, 1988). So if  $w_{si}$  varies in every grid cell, then observations of  $C_i$  at every grid cell are required to determine  $w_{si}$ . To determine either one of  $M_o$ ,  $\tau_{cd}$  and  $\tau_{cr}$  the number of observations of  $C_j$  should be equal to or greater than the number of horizontal grid cells. Apparently, if  $w_{si}$ ,  $M_o$ ,  $\tau_{cd}$  and  $\tau_{cr}$  are all spatially (grid cell) dependent, the problem of estimation of these four parameters at the same time will become underdetermined because the number of total sediment observations is always less than the number of parameters. However, for

constant or regionally dependent  $w_{si}$ ,  $M_o$ ,  $\tau_{cd}$  and  $\tau_{cr}$ , it is possible to determine all of the four parameters at the same time with limited sediment observations.

In an intra-tidal transport model  $(u, v, w)$ ,  $D_H$  and  $D_V$  can be provided by a hydrodynamic model and turbulent closure model, but in an inter-tidal transport model, which has a time scale of several tidal cycles or longer, the effective Lagrangian mean transport flow field  $(u_m, v_m, w_m)$  and mean diffusivities  $\langle D_H \rangle$  and  $\langle D_V \rangle$  are still not well known (see Chapter 3). As one considers a long-term transport problem for a neutral buoyant tracer  $C_i$ , then if the effective Lagrangian mean transport flow field  $(u_m, v_m, w_m)$  is known, observations of one tracer  $C_i$  ( $i=1$ ) will be sufficient to determine either one of  $\langle D_H \rangle$  and  $\langle D_V \rangle$ , or observations of two different tracer  $C_i$  ( $i=1,2$ ) will determine both  $\langle D_H \rangle$  and  $\langle D_V \rangle$  at the same time. If  $\langle D_H \rangle$  and  $\langle D_V \rangle$  are known, then to estimate a 3-D effective Lagrangian mean transport flow field, observations of two different tracer are required since the three velocity components  $u_m$ ,  $v_m$  and  $w_m$  must satisfy the continuity equation (Eq. (11)), which provides one more dynamic constraint to the inverse problem. For a 2-D problem, observations of one tracer are enough to determine the long-term mean transport flow field.



### 3. THE TRACER INVERSE PROBLEM

#### 3.1 Introduction

In coastal and estuarine zones, the spectrum of flow generally consists of a wide range of time scale components, from seconds (high frequency turbulent flow) to days (tidal current), and even to months (low frequency flow). Even though all of these different time scale processes are present in the coastal and estuarine waters, the long term low frequency velocity field or residual current usually plays the most important role in the biogeochemical transport processes in coastal and estuarine zones since biogeochemical processes generally take place over several tidal cycles or longer. However, it is very difficult to quantify residual currents and long-term transport due to the fact that the residual variables are the results of nonlinear interaction of tidal variables and are not directly measurable. Nearly all field results of residual currents are derived from field observations by applying a low pass filter. So numerical modeling of long-term biogeochemical transport has been attracting the interest of coastal physical oceanographers in recent years in response to increasing demands for the optimized management of resources in the marine ecosystem. In addition to providing an advective transport field for long-term transport modeling, the Lagrangian mean velocity may also provides insight into the net transport patterns in the region of interest. In order to drive the long-term transport model, the effective long-term transport flow field must be known. In recent years, the concept of Lagrangian mean velocity, which is defined as the average of the velocity of an identified water particle over a long time span, has been used to

study the long-term transport problems in estuarine and coastal waters (Hamrick, 1990, 1994; Cheng & Casulli, 1982, 1992 and Feng, *et al.*, 1986a, 1986b). However, the difficulty faced is that the model equations are constructed in the Eulerian form and all the numerical variables directly solved from the model equations are the Eulerian variables. Therefore, a linkage (or transfer formalism) between the Eulerian mean velocity and the Lagrangian mean velocity must be established. Many studies have attempted to seek the analytical solutions for the Lagrangian mean velocity as a function of the Eulerian variables using perturbation methods. The pioneering work on this problem was done by Longuet-Higgins (1969). He showed that the Lagrangian mean velocity can be expressed as the sum of the Eulerian mean velocity and the Stokes' drift. More detailed analytical extensions to this work have been reported (Zimmerman, 1979; Cheng & Casulli, 1982; Feng *et al.*, 1986a). Zimmerman (1979) pointed out that analytical solutions may become questionable under moderately nonlinear or strongly nonlinear dynamic conditions due to the convergent restriction of the expansion of the Taylor series in perturbation approaches. Zimmerman (1979) and Cheng and Casulli (1982) also pointed out that the Lagrangian mean velocity is a function of tidal phase. Using the perturbation method, Feng *et al.* (1986a) showed that the first-order truncation error of the approximation is a so-called Lagrangian drift term which is dependent on phase. Under the weakly nonlinear approximation, Feng *et al.* (1986b) also showed that the first-order tidally-averaged transport equation for a conservative solute is a pure convective equation, in which the flow field is the first order Lagrangian mean velocity, which is the same as the mass transport velocity given by Longuet-Higgins (1969).

Apparently, under the weakly nonlinear approximation, the first order Lagrangian mean velocity or mean mass transport velocity is independent of tidal phase, and it is the flow field which has a direct impact on the long term transport processes.

In moderately nonlinear or strongly nonlinear cases, the Lagrangian mean velocity strongly depends on the tidal phase because the time-dependent Lagrangian drift term becomes comparably large. In this case the Lagrangian mean velocity becomes questionable (Zimmerman, 1979; Cheng & Casulli, 1982, 1986 and Hamrick, 1994). Cheng and Casulli (1992) presented a new definition of Lagrangian mean velocity without invoking the weakly nonlinear approximation. They derived a general governing inter-tidal transport equation for conservative solute based on such a definition of Lagrangian mean velocity. This governing inter-tidal transport equation is a convection-dispersion equation in which the convective velocity is Lagrangian mean velocity and the inter-tidal dispersion coefficient is defined by a dispersion patch. The mean Lagrangian velocity and the inter-tidal dispersion coefficient are determined numerically. However, in strongly nonlinear flows, the dispersion patch can be highly distorted and the proposed Lagrangian mean velocity and governing inter-tidal transport equation may also become questionable. Hamrick (1994) defined an exact averaged Lagrangian mean velocity which is the average of a number of exact Lagrangian mean velocities at different phases over a tidal cycle. But such an exact averaged Lagrangian mean velocity may also not satisfy the continuity equation. Apparently, a time dependent Lagrangian mean velocity field is not the true flow field representing long term transport processes, hence it is not suitable to be used to describe the long term transport problems.

To date, most of studies on the Lagrangian mean velocity invoke the weakly nonlinear approximation, and few publications have been found on moderately nonlinear or strongly nonlinear transport problems. The analytical solution for the Lagrangian mean velocity under moderately nonlinear or strongly nonlinear conditions does not exist. In order to describe the long-term transport process in any dynamical conditions, seeking numerical solutions of the Lagrangian mean velocity field without invoking weakly nonlinear approximation is highly desirable. In this chapter, a variational inverse parameter estimation scheme is developed to determine the Lagrangian mean transport field for a long-term transport model without invoking a weakly nonlinear approximation.

### 3.2 Governing Equation for The Long-Term Transport Problem

Considering the transport process for a single neutral buoyant tracer  $C$  ( $w_s=0$ ), the intra-tidal biogeochemical transport equation (1) then is simplified as:

$$\begin{aligned} \partial_t (mHC) + \partial_x (m_y H u C) + \partial_y (m_x H v C) + \partial_z (m w C) \\ = \partial_x (m H^{-1} D_v \partial_z C) + m H Q \end{aligned} \quad (3)$$

Horizontal turbulent diffusion has been omitted from Eq. (3) since it can be shown to be an order of magnitude less important than the horizontal advection.

There are two possible ways to get the solutions of inter-tidal transport of a conservative solute over a time span of several tidal periods or longer. A straightforward approach is the direct integration of the governing intra-tidal transport equation over a long period of time, such as several tidal cycles. The tidally-averaged solute concentration is derived from time-averaging the time dependent solution, or by applying

a low pass filter to remove tidal fluctuations. An alternative approach is to apply a time-averaging operator (or low pass filter) directly to the intra-tidal governing equation to obtain the long-term transport equation. Under the weakly nonlinear approximation, the long-term biogeochemical transport equation can be derived from Eq. (3) by a multiple time scale perturbation analysis (Hamrick, 1990, 1994):

$$\begin{aligned} \partial_t (m \langle H \rangle \langle C \rangle) + \partial_x (m_y \langle H \rangle u_m \langle C \rangle) + \partial_y (m_x \langle H \rangle v_m \langle C \rangle) + \partial_z (m w_m \langle C \rangle) \\ = \partial_x (m \langle H^{-1} \rangle \langle D_v \rangle \partial_x \langle C \rangle) \end{aligned} \quad (4)$$

where  $\langle \rangle$  is a temporal average operator with an interval of one or several tidal cycles.  $(u_m, v_m, w_m)$  are the components of the Lagrangian mean transport field which can be decomposed into the sum of Eulerian mean transport field and the curl of a vector potential  $A$ :

$$\begin{Bmatrix} m_y \langle H \rangle u_m \\ m_x \langle H \rangle v_m \\ m w_m \end{Bmatrix} = \begin{Bmatrix} m_y \langle H \rangle u_{ET} \\ m_x \langle H \rangle v_{ET} \\ m w_{ET} \end{Bmatrix} + \begin{Bmatrix} \partial_y A_z - \partial_z A_y \\ \partial_z A_x - \partial_x A_z \\ \partial_x A_y - \partial_y A_x \end{Bmatrix} \quad (5)$$

where  $(u_{ET}, v_{ET}, w_{ET})$  are the known Eulerian mean transport field defined by Cheng and Casulli (1982):

$$\begin{Bmatrix} m_y \langle H \rangle u_{ET} \\ m_x \langle H \rangle v_{ET} \\ m w_{ET} \end{Bmatrix} = \begin{Bmatrix} m_y (\langle H \rangle \langle u \rangle + \langle H' u' \rangle) \\ m_x (\langle H \rangle \langle v \rangle + \langle H' v' \rangle) \\ m \langle w \rangle \end{Bmatrix} \quad (6)$$

with  $(u', v', w', H')$  representing the zero mean tidal fluctuations defined by:

$$(u', v', w', H') = (u, v, w, H) - (\langle u \rangle, \langle v \rangle, \langle w \rangle, \langle H \rangle) \quad (7)$$

Given the time scale of salinity response to the fresh water inflow, the Lagrangian mean

transport field, Eq.(5), and the long-term transport equation, Eq.(4), are valid in the time scale of weeks to months. Under the weakly-nonlinear approximation, the effective transport velocity  $(u_m, v_m, w_m)$  in Eq. (5) is equivalent to the mass transport velocity defined by Longuet-Higgins (1969) (also see Feng *et al.*, 1986b and Hamrick, 1994) and the vector potential  $\mathbf{A}$  is given by:

$$\{A_x, A_y, A_z\} = \left\{ m_x \left\langle v' \int_0^t w' dt \right\rangle, m_y \left\langle w' \int_0^t u' dt \right\rangle, \langle H \rangle \left\langle u' \int_0^t v' dt \right\rangle \right\} \quad (8)$$

Taking a temporal average on Eq. (2), it can be shown that the Eulerian mean transport velocity satisfies the continuity equation:

$$\partial_t (m \langle H \rangle) + \partial_x (m_y \langle H \rangle u_{ET}) + \partial_y (m_x \langle H \rangle v_{ET}) + \partial_z (m w_{ET}) = 0 \quad (9)$$

Due to the nondivergent characteristic of the vector potential  $\mathbf{A}$ , *i.e.*:

$$\partial_x (\partial_y A_z - \partial_z A_y) + \partial_y (\partial_z A_x - \partial_x A_z) + \partial_z (\partial_x A_y - \partial_y A_x) = 0 \quad (10)$$

it can be easily shown that the Lagrangian mean transport velocity also satisfies the continuity equation by summing Eqs. (9) and (10):

$$\partial_t (m \langle H \rangle) + \partial_x (m_y \langle H \rangle u_m) + \partial_y (m_x \langle H \rangle v_m) + \partial_z (m w_m) = 0 \quad (11)$$

Thus, the optimal Lagrangian mean transport velocity can be obtained by adjusting the vector potential  $\mathbf{A}$  using a variational data assimilation technique. The mass conservation constraint is always satisfied during the evolution of the vector potential. The Eulerian advection field is considered as a known flow field, which can be calculated from a hydrodynamic model based on Eq. (6). It should be pointed out that the Eulerian mean

transport can be poorly known, such as from field observations, and the total transport misfit will be corrected by the vector potential  $A$ .

### 3.3 Adjoint Model and Gradient of The Cost Function

The basic idea of variational inverse analysis is to seek the best fit solution of model equations by minimizing the cost function  $J$  which consists of a weighted square sum of the differences between the observed data and the model counterparts over the entire time and spatial domains (Navon, 1986; Le Dimet and Navon, 1988):

$$J = \frac{1}{2} \int_T \int_V [B(C) - C^{obs}]^T W [B(C) - C^{obs}] dV dt \quad (12)$$

in which  $V$  represents the three-dimensional model region volume,  $T$  represents the total time interval,  $C^{obs}$  is the observed data and  $C$  is the model counterpart of  $C^{obs}$ ,  $B$  is the observation operator which maps the model counterpart  $C$  to observation  $C^{obs}$  and  $W$  is a symmetric and positive weighing matrix.  $W$  generally can be calculated as the inverse of the error covariance matrix of observations, which reflects confidence in the quality of observed data. If all observations are independent and their errors are uncorrelated, then  $W$  should be diagonal. The best fit model state is defined by the model parameters, or initial and boundary conditions that correspond to a minimum of the cost function  $J$  measuring the misfit between observations and model counterparts. The minimization of the cost function  $J$  (Eq(12)) is subject to a dynamical constraint  $F(C, V, t)=0$ , which is the dynamical model equation. For long-term steady-state problems, the cost function  $J$  is constructed in the spatial domain only:

$$J = \frac{1}{2} \int_V [B(C) - C^{obs}]^T W [B(C) - C^{obs}] dV \quad (13)$$

The problem of extracting the dynamical state from observations can be identified as the mathematical problem of seeking optimal solutions of initial or boundary conditions and model parameters (control variables) that minimize the cost function. There are various methods to seek the extremum of a function. Apparently, in order to determine the minimum of the cost function, it is necessary that the functional relationship of tracer  $C$  to the control variables be specified and the gradients of the cost function with respect to the control variables be given. The fact that the cost function is generally a complicated implicit function of control variables complicates the problem of minimizing the cost function. Adjoint methods, part of the optimal control of partial differential equations theory, which integrate model equations backward in time, are found to be the most powerful and efficient tools to obtain the gradients of the cost function with respect to the control variables (Schroter, 1989; Thacker, 1990; Yu and O'Brien, 1991; Schlitzer, 1993). The adjoint methods have been widely used in many studies in the fields of meteorology and oceanography to obtain the gradients of the cost function. In order to avoid repeated application of the chain rule when computing the gradient of the cost function, the gradient computation can be greatly simplified by the use of a Lagrange function constructed by appending the model equations to the cost function as dynamic constraints (Navon and deVilliers, 1983; Thacker, 1987; Ghil and Malanotte-Rizzoli, 1991):



$$L = J + \int_T \int_V \lambda \left\{ \begin{array}{l} \partial_t (m \langle H \rangle \langle C \rangle) + \partial_x [ (m_y \langle H \rangle u_{ET} + \partial_y A_z - \partial_z A_y) \langle C \rangle ] \\ + \partial_y [ (m_x \langle H \rangle v_{ET} + \partial_z A_x - \partial_x A_z) \langle C \rangle ] \\ + \partial_z [ (m w_{ET} + \partial_x A_y - \partial_y A_x) \langle C \rangle ] - \partial_z (m \langle H^{-1} \rangle \langle D_v \rangle \partial_z \langle C \rangle) \end{array} \right\} dv dt \quad (14)$$

The Lagrange function Eq. (14) is a function of all model variables and the Lagrange multiplier. The dynamical constraint thus is enforced by introducing the Lagrange multipliers. The adjoint technique yields estimates of gradients of the cost function with respect to control variables, permitting use of local descent algorithms to seek a minimum cost function. Since the stationary point of the Lagrange function coincides with the minimum of the cost function, the problem of minimizing the cost function  $J$  subject to a dynamic constraint of the model equation is now transformed into a problem of minimizing the unconstrained Lagrange function  $L$ . The governing equations for the best fit solution require that all first partial derivatives of the Lagrange function vanish (Thacker, 1987):

$$\partial_\lambda L = 0 \quad (15)$$

$$\partial_{\langle C \rangle} L = 0 \quad (16)$$

$$\partial_{A_x} L = 0 \quad (17)$$

$$\partial_{A_y} L = 0 \quad (18)$$

$$\partial_{A_z} L = 0 \quad (19)$$

Differentiating  $L$  with respect to  $\lambda$ , Eq. (15) simply recovers the model equation (3).

Differentiating  $L$  with respect to  $\langle C \rangle$ , Eq. (16) results in the adjoint equation:

$$\begin{aligned}
& -m\langle H \rangle \partial_t \lambda - (m_y \langle H \rangle u_{ET} + \partial_y A_z - \partial_z A_y) \partial_x \lambda \\
& - (m_x \langle H \rangle v_{ET} + \partial_z A_x - \partial_x A_z) \partial_y \lambda - (mw_{ET} + \partial_x A_y - \partial_y A_x) \partial_z \lambda \quad (20) \\
& -\partial_z (m\langle H^{-1} \rangle \langle D_v \rangle \partial_z \lambda) = -\partial_c J = W(\langle C \rangle^{obs} - B(\langle C \rangle))
\end{aligned}$$

Using Eq. (11), Eq. (20) can be further arranged into the following form:

$$\begin{aligned}
& -\partial_t (m\langle H \rangle \lambda) - \partial_x [(m_y \langle H \rangle u_{ET} + \partial_y A_z - \partial_z A_y) \lambda] \\
& -\partial_y [m_x \langle H \rangle v_{ET} + \partial_z A_x - \partial_x A_z] \lambda - \partial_z [(mw_{ET} + \partial_x A_y - \partial_y A_x) \lambda] \quad (21) \\
& -\partial_z (m\langle H^{-1} \rangle \langle D_v \rangle \partial_z \lambda) = W(\langle C \rangle^{obs} - B(\langle C \rangle))
\end{aligned}$$

From Eq. (20) we can solve for the Lagrange multiplier  $\lambda$  by integrating the equation backward in time. Note that the adjoint equation is always linear in the adjoint variables (Lagrange multipliers), even when the dynamical model is nonlinear. The signs of temporal and advection terms in the adjoint model Eq. (20) are reversed, which indicates the Lagrange multipliers serve to collect information from the data and to propagate it back to the initial time where it can be used to improve the initial guess of the vector potential  $A$  that defines the best fit. On the other hand, the sign of the vertical diffusive term is not reversed.

In a long-term steady state problem, the gradients of the cost function  $J$  are calculated in the spatial domain only. Therefore the gradients of the cost function  $J$  with respect to the vector potential field can be derived from Eqs. (17-19):

$$\partial_{A_x} \mathcal{J} = [\partial_y (\langle C \rangle \partial_z \lambda) - \partial_z (\langle C \rangle \partial_y \lambda)] \quad (22)$$

$$\partial_{A_y} \mathcal{J} = [\partial_z (\langle C \rangle \partial_x \lambda) - \partial_x (\langle C \rangle \partial_z \lambda)] \quad (23)$$

$$\partial_{A_z} \mathcal{J} = [\partial_x (\langle C \rangle \partial_y \lambda) - \partial_y (\langle C \rangle \partial_x \lambda)] \quad (24)$$

and combined into a simple vector form:

$$\nabla_A \mathcal{J} = \nabla \times (\langle C \rangle \nabla \lambda) \quad (25)$$

Thus, with solutions for the multiplier  $\lambda$  and tracer concentration  $\langle C \rangle$ , the gradients of the cost function with respect to  $A$  can be calculated by Eqs. (22-24).

Now the variational inverse method for inverting the tracer field to the Lagrangian mean velocity field in a conservative tracer long-term transport problem can be stated as: given the initial guess of the vector potential  $A$ , solve the forward problem Eq. (4); then adjust the vector potential  $A$  by assimilating the observation data into the transport model so as to reduce iteratively the misfit between observation data and the model counterparts to a minimum. The procedure for solving this system Eqs. (15, 21-24) includes the following steps:

1. Assume an initial guess for the vector potential  $A$ ;
2. Calculate tracer distribution in the entire spatial domain from the long-term transport model Eq. (4);
3. Construct the cost function  $J$  and the adjoint model Eq. (21);
4. Integrate the adjoint model Eq. (21) backward in time to compute the Lagrange multipliers and evaluate the gradients of the cost function by Eqs. (22-24);

5. Conduct a line search to find the descent optimal step size and get an improved guess of the vector potential  $\mathbf{A}$ ;
6. Check whether the solution is convergent under a convergence criterion given by:

$$\|\nabla J\| / \|\nabla J_0\| \leq \epsilon \quad (26)$$

where  $\nabla J_0$  is the gradient norm of the cost function at the initial iteration and  $\epsilon$  is the convergence criterion;

7. If the convergence criterion is not satisfied, repeat from step 2 with the newly adjusted vector potential until the convergence criterion is reached.

### 3.4 Descent Algorithm

To find the minimum of the cost function, an optimization method must be applied after evaluating the gradients of the cost function. One of the most widely used methods for the minimization problem is the conjugate-gradient method (Navon and Legler, 1987; Thacker, 1990; Smedstad and O'Brien, 1991). The conjugate-gradient algorithm, which was initiated by Hestenes and Stiefel (1952), is an iterative method for unconstrained minimization of a function of many variables. During each iteration, a best adjustment is made to change each variable in order to produce the maximum reduction in the function. The descent direction is found by combining the information of the gradients of the function with the information from earlier integrations to generate a new search direction. The conjugate-gradient method has been successfully applied in meteorology for many years. Navon and Legler (1987) compared four different conjugate-gradient

methods by applying them to two different meteorological problems and concluded that the most consistent and best performing method was the Shanno and Phua (1980) limited-memory quasi-Newton (LMQN) conjugate-gradient algorithm (also see Nocedal, 1980; Liu and Nocedal, 1989). Zou *et al.* (1993a) further compared four limited-memory quasi-Newton and two truncated Newton methods for a variety tested and real-life problems. They concluded that among the tested LMQN methods, the L-BFGS method (Limited Broyden-Fletcher-Goldfarb-Shanno method) has the best overall performance (also see Navon *et al.*, 1992a, 1992b). It uses the fewest iterations and function calls, and it can be greatly improved by a simple scaling or a more accurate line search. The L-BFGS implementation will be used in the present study. The basic structure of the LMQN method for minimizing  $J(\mathbf{x})$  as a function of vector  $\mathbf{x}$  can be described as follows (Navon and Legler, 1987; Zou *et al.*, 1993a):

1. Choose an initial guess  $\mathbf{x}_0$  and approximation of inverse Hessian matrix  $\mathbf{H}_0$  which is taken as the identity matrix.

2. Compute the gradient of  $J(\mathbf{x}_0)$ :

$$\mathbf{g}_0 = \nabla J(\mathbf{x}_0) \quad (27)$$

and set the descent direction to be:

$$\mathbf{d}_0 = -\mathbf{H}_0 \mathbf{g}_0 \quad (28)$$

3. Set the new vector  $\mathbf{x}_{k+1}$  for  $k=0,1,2,\dots$ ,

$$\mathbf{x}_{k+1} = \mathbf{x}_k + \alpha_k \mathbf{d}_k \quad (29)$$

where  $\alpha_k$  is a positive step size.

4. Check for restart.

5. Update the inverse Hessian matrix  $H_k$ . The most popular updating method is the BFGS formula:

$$H_{k+1} = H_k - \frac{H_k y_k p_k^T + p_k y_k^T H_k}{p_k^T y_k} + \left( 1 + \frac{y_k^T H_k y_k}{p_k^T y_k} \right) \frac{p_k p_k^T}{p_k^T y_k} \quad (30)$$

where  $p_k = x_{k+1} - x_k$  and  $y_k = g_{k+1} - g_k$ . For problems with a large number of variables, it is often impossible to store an approximation to the inverse Hessian matrix. Shanno (1978a,b) developed an alternative method (limited-memory quasi-Newton method) in which  $H_k$  is set to be the identity matrix in Eq. (30) and thus the new descent direction is defined as:

$$d_{k+1} = -g_{k+1} - \left[ \left( 1 + \frac{y_k^T y_k}{p_k^T y_k} \right) \frac{p_k^T g_{k+1}}{p_k^T y_k} - \frac{y_k^T g_{k+1}}{p_k^T y_k} \right] p_k + \frac{p_k^T g_{k+1}}{p_k^T y_k} y_k \quad (31)$$

6. Stop if the convergence criterion is satisfied:

$$\frac{\|g_{k+1}\|}{\|g_0\|} \leq \epsilon \quad (32)$$

where  $\| \cdot \|$  represents the gradient norm and  $\epsilon$  is the convergence criterion parameter.

### 3.5 Model Tests in An Idealized Vertical 2-D Estuary

#### 3.5.1 Model Setup

The inverse model is tested in an idealized vertical two-dimensional semi-enclosed estuary. The geometry is shown in Fig. 1. The total length of the estuary is 85 km. The width and depth of the estuary are 1 km and 10 m, respectively, at the head and linearly

increase to 3 km and 15 m, respectively, 80 km from the head and then become constant. There are 85 grid cells longitudinally and 10 layers vertically. In the vertical two-dimensional case, if the  $x$ -coordinate is chosen in the longitudinal direction and the  $z$ -coordinate upward, then the  $x$ - and  $z$ - components (*i.e.*  $A_x$  and  $A_z$ ) of the vector potential  $A$  become zero and  $A$  is reduced to a scalar function  $A_y$ , which is equivalent to a stream function. The Lagrangian mean velocity then can be expressed as:

$$\begin{Bmatrix} m_y \langle H \rangle u_m \\ 0 \\ mw_m \end{Bmatrix} = \begin{Bmatrix} m_y \langle H \rangle u_{ET} \\ 0 \\ mw_{ET} \end{Bmatrix} + \begin{Bmatrix} -\partial_z A_y \\ 0 \\ \partial_x A_y \end{Bmatrix} \quad (33)$$

In the present experiment, the vector potential transport (the second term on the right hand side of Eq.(33)) is about 20 percent of the Eulerian mean transport (the first term on the right hand side of Eq.(33)).

The estuary is subject to the  $M_2$  tide forcing at the open boundary (mouth) and a constant freshwater discharge (200 m<sup>3</sup>/s) from the head. Salinity is used as the observed tracer. Three experiments are carried out: *case 1*) basic model test for recovering vector potential with salinity observation available at every grid cell; *case 2*) test with reduced observation data; *case 3*) test with noisy observation data.

The Eulerian mean transport velocity ( $u_{ET}$ ,  $v_{ET}$ ,  $w_{ET}$ ) can be calculated by (5) from a real time hydrodynamic model. Under the weakly nonlinear approximation, the vector potential  $A$  can be computed based on Eq. (8). The mean vertical diffusivity  $\langle D_v \rangle$  can be obtained by taking the time average of the intratidal vertical diffusivity. The real time hydrodynamic model used in the present study is the three-dimensional Environmental

Fluid Dynamic Computer Code (EFDC) developed at the Virginia Institute of Marine Science (Hamrick, 1992a; Hamrick and Wu, 1996). The model solves the three-dimensional primitive equations of motion for turbulent flow in a horizontal curvilinear-orthogonal and vertical sigma-stretched coordinate system. A second moment turbulent closure model (Mellor and Yamada, 1982; Galperin *et al.*, 1988) is used to relate the turbulent viscosity and diffusivity to the turbulence intensity and length scale. Transport equations for turbulence intensity and turbulence length scale as well as for salinity, temperature, suspended sediment and a dye tracer are solved. The horizontal momentum equations and continuity equations are solved using an external-internal mode splitting.

Before applying the adjoint model in the variational inverse data assimilation experiments, the correctness of the adjoint model must be first checked using a Taylor expansion (Navon *et al.*, 1992):

$$J(A + \alpha \nabla J) = J(A) + \alpha (\nabla J)^T (\nabla J) + O(\alpha^2) \quad (34)$$

where  $\alpha$  is a small scalar but not too close to machine zero. From (34) we have:

$$\Phi(\alpha) = \frac{J(A + \alpha \nabla J) - J(A)}{\alpha (\nabla J)^T (\nabla J)} = 1 + O(\alpha) \quad (35)$$

Therefore, function  $\Phi(\alpha)$  is defined in terms of  $\alpha$ , the cost function  $J$  and the gradient of the cost function  $\nabla J$ . If the gradient of the cost function is calculated correctly, the value of  $\Phi(\alpha)$  should linearly approach 1 as  $\alpha$  decreases in a range covering several orders of magnitude. Table 1 shows that for  $\alpha$  between  $10^{-8}$  to  $10^{-15}$ , a unit value of  $\Phi(\alpha)$  is found. Fig. 2 shows the variation of function  $\Phi(\alpha)$  with decreasing values of  $\alpha$ . The residual of  $\Phi(\alpha)$  (*i.e.*,  $|\Phi(\alpha) - 1|$ ) is shown in Fig. 3. It can be seen that the residual approaches zero



due to the characteristics of the Taylor expansion. The correctness of the gradient of the cost function is therefore verified and the adjoint model can be safely used in the variational inverse data assimilation experiments.

### 3.5.2 Basic Experiment

In the present study, the  $y$ -component of vector potential ( $A_y$ ) calculated from the hydrodynamic model based on Eq. (8), serves as the true solution. The Eulerian mean transport field is calculated by Eq. (6) while the Lagrangian mean transport field is calculated by Eq. (5) and is used to generate salinity observations for the twin experiments with the long-term transport model Eq. (4). The model was run for 100 tidal cycles to insure a steady state. Distributions of  $A_y$  and the corresponding vector potential transport field along the estuary are shown in Figs. 4 and 5 respectively. The Eulerian mean transport and the Lagrangian mean transport are plotted in Figs. 6 and 7. We can see clearly that a two-layer mean circulation pattern is presented in both the Eulerian mean transport field (Fig. 6) and Lagrangian mean transport field (Fig. 7). In this experiment, the vector potential transport field (Fig. 5) is about 10 percent and 25 percent of the Eulerian mean transport in the surface layer and in the bottom layer, respectively. The distribution of the observed salinity is given in Fig. 8. All the data are assumed to be perfect. The weighing matrix  $W$  is set to be unity because the observation data used in this study are generated by the same model and assumed to be perfect everywhere.

In this experiment, salinity observations are assumed to be available at every grid

point. Since the locations of observation data and the model counterpart are identical, the observation operator  $B$  becomes unity. In order to test the capability of the scheme to recover the vector potential, we simply set the initial guess of  $A_y$  equal to zero. The initial salinity distribution is shown in Fig. 9. The initial salinity misfit (*i.e.*, the difference between Figs. 8 and 9) is shown in Fig. 10. The variations of the relative cost function  $\|J_n\|/\|J_0\|$  (dashed line) and gradient norm  $\|\nabla J_n\|/\|\nabla J_0\|$  (solid line) in terms of number of iterations are shown in Fig. 11. Convergence occurs after 30 iterations when the convergence criterion is set at  $10^{-3}$  and about 250 iterations when the convergence criterion is  $10^{-5}$ . From Fig. 11 we can see that the minimization process converges fast in the first 50 iterations or so and then slows down thereafter. The estimated vector potential  $A_y$  is shown in Fig. 12. In order to see how accurate the estimated solution is, the error of the estimated  $A_y$  is calculated by the following formula:

$$E_{l,k} = \frac{(A_y)_{l,k}^E - (A_y)_{l,k}^T}{\max[(A_y)_{l,k}^T]} \quad (36)$$

where  $(A_y)_{l,k}^E$  and  $(A_y)_{l,k}^T$  denote the estimated and true solutions of  $A_y$  at cell  $(l, k)$  respectively.  $l$  and  $k$  are the horizontal and vertical grid cell indices. The distribution of  $E_{l,k}$  is given in Fig. 13. This figure shows that  $E_{l,k}$  is below 5% in the whole region. The maximum discrepancy is observed in the river head area. Fig. 14 shows the final salinity misfit. We can see that in the area corresponding to the maximum  $E_{l,k}$  the salinity misfit is also a maximum. This feature can be explained by the importance of the advection due to the vector potential term on the transport process in this area. Pearlstein and Carpenter (1995) pointed out that in general cases when the advection term  $\mathbf{u} \cdot \nabla C$  vanishes in some

area, the observed scalar field provides no information about the velocity  $\mathbf{u}$ . To demonstrate this, we calculated the portion of the advective transport contributed from the vector potential, *i.e.*  $(\nabla \times \mathbf{A}) \cdot \nabla C$ . The result is shown in Fig. 15. Apparently, in the area close to the river head,  $(\nabla \times \mathbf{A}) \cdot \nabla C$  approaches zero. Hence the observations in that area actually provides little information on  $A_y$ , so that the inverse model does not work efficiently in this area. This may also be the reason that the convergence speed of the minimization process decreases.

### 3.5.3 Experiments with Sparse Data

In reality, it is impractical to have observation data available at every model grid cell. It is important to test the capability of the inverse scheme to recover the vector potential in cases where the number of the observed data values is less than the number of control variables to be estimated. The objective of this experiment is to examine whether the inverse model can still retrieve a reasonable solution in such a situation.

In this experiment, observation data are sampled at every five grid points in the horizontal and at every layer in the vertical. The recovered solution is given in Fig. 16. We can see that strong spatial oscillations occur in the solution. This indicates that the number of degrees of freedom of the problem is much greater than the number of the observations. One way to eliminate the spatial oscillations and recover the model dynamics in the case of inadequate data is to use bogus data to enforce the smoothness of the solution. The spatial smoothness can be implemented by appending a penalty term in the cost function to form a penalized cost function. The idea of the penalty method

has been used in many applications. Thacker (1988) found that reasonable fits can be obtained by using smoothness penalties in a simple three-wave model when the number of real data is considerably less than the model degrees of freedom. Provost and Salmon (1986) penalized kinetic energy and entropy to insure smoothness in inverting hydrographic data. Zou *et al.* (1992a) showed that the penalty method can efficiently control gravity waves in a shallow water equations model. They also showed that the inclusion of penalty terms in the cost function can improve the conditioning of the Hessian of the cost function in the case of inadequate data by convexifying the cost functional, therefore leading to a unique solution. Lardner and Das (1994) pointed out a penalty term must be included in the cost function to smooth out the instabilities associated with noisy data when estimating the eddy viscosity in a quasi-three-dimensional numerical tidal and storm surge model.

In this study, the first order horizontal penalty on the y-component of vector potential ( $A_y$ ) is considered and the penalized cost function is constructed as:

$$J_p = J + \frac{1}{2} \beta (\partial_x A_y)^2 \quad (37)$$

where  $\beta$  is the penalty coefficient. The smoothness increases as  $\beta$  becomes larger. The gradient of the penalty cost function with respect to  $A_y$  can be calculated by appending an additional term

$$\beta \partial_x A_y \quad (38)$$

to the gradient of the nonpenalized cost function (Zou *et al.*, 1993b; Lardner and Das, 1994).

Experiments with different values of the penalty coefficient  $\beta$  were conducted. The final results showed that a satisfactory solution is obtained when  $\beta=0.1$  (Fig. 17). A comparison among the results of estimated  $A_y$  along the river at mid-level for different values of  $\beta$  is given in Fig. 18. We can see that  $\beta=0.01$  does not provide enough smoothness while  $\beta=10$  produces overly smooth results.

### 3.5.4 Experiments with Noisy Data

In reality, observations more or less contain noise. The purpose of this experiment is to test how well the model can retrieve the true solution with noisy data. The noisy data are generated by appending a set of normally distributed random data with zero mean and 0.15 standard deviation to the perfect data at every grid point. Results show that the recovered solution has strong spatial random oscillation and the main pattern is highly distorted (Fig. 19) even though observations are available at every grid point. So the vector potential is very sensitive to noise. Similar to Section 3.5.3, a penalty term is also added to the nonpenalized cost function to smooth noisy oscillations. We found in this case, the penalty term has to be larger than that used in Section 3.5.3. The reasonable solution is shown in Fig. 20 with a penalty coefficient  $\beta=10$ . Experimental results along the river channel with different values of  $\beta$  are shown in Fig. 21. It can be seen that stronger penalty ( $\beta=10$ ) is required to retrieve a reasonable result compared to the experiments for sparse data.

## 3.6 Some Discussions on the 3-D Problem

Now let us look at the 3-D problem of inverting a tracer field into the Lagrangian mean transport velocity. In order to determine a unique 3-D Lagrangian mean transport field, as Pearlstein and Carpenter (1995) pointed out, one continuity equation and two transport equations for two different tracers are required. However, when decomposing the 3-D Lagrangian mean transport field by Eq. (5) and transforming the inverse problem into seeking the vector potential  $\mathbf{A}$ , we lose the continuity constraint but still have three unknowns ( $A_x, A_y, A_z$ ). This indicates that ( $A_x, A_y, A_z$ ) are actually not solely independent but related. Therefore, the problem for solving the 3-D vector potential  $\mathbf{A}$  with two tracer transport equations becomes underdetermined. Another way to seek an unconstrained solution for the Lagrangian mean transport velocity is to consider an alternative form of the Helmholtz decomposition for the Lagrangian mean transport velocity involving the Eulerian mean transport field and two scalar functions  $\psi$  and  $\chi$  (Aris, 1989):

$$\begin{pmatrix} m_y \langle H \rangle u_m \\ m_x \langle H \rangle v_m \\ m w_m \end{pmatrix} = \begin{pmatrix} m_y \langle H \rangle u_{ET} \\ m_x \langle H \rangle v_{ET} \\ m w_{ET} \end{pmatrix} + \begin{pmatrix} \partial_y \psi \partial_z \chi - \partial_z \psi \partial_y \chi \\ \partial_z \psi \partial_x \chi - \partial_x \psi \partial_z \chi \\ \partial_x \psi \partial_y \chi - \partial_y \psi \partial_x \chi \end{pmatrix} \quad (39)$$

It can be shown that the second term on the right hand side of Eq. (39) always satisfies the continuity equation:

$$\partial_x (\partial_y \psi \partial_z \chi - \partial_z \psi \partial_y \chi) + \partial_y (\partial_z \psi \partial_x \chi - \partial_x \psi \partial_z \chi) + \partial_z (\partial_x \psi \partial_y \chi - \partial_y \psi \partial_x \chi) = 0 \quad (40)$$

Thus, the inverse problem for seeking the Lagrangian mean transport velocity subject to continuity constraint is transformed into seeking two unconstrained scalar functions  $\psi$  and  $\chi$  with two transport equations:

$$\begin{aligned}
& \partial_t (m \langle H \rangle \langle C_i \rangle) + \partial_x [ (m_y \langle H \rangle u_{ET} + \partial_y \psi \partial_z \chi - \partial_z \psi \partial_y \chi) \langle C_i \rangle ] \\
& + \partial_y [ (m_x \langle H \rangle v_{ET} + \partial_z \psi \partial_x \chi - \partial_x \psi \partial_z \chi) \langle C_i \rangle ] \\
& + \partial_z [ (mw_{ET} + \partial_x \psi \partial_y \chi - \partial_y \psi \partial_x \chi) \langle C_i \rangle ] \\
& = \partial_z (m \langle H^{-1} \rangle \langle D_v \rangle \partial_z \langle C_i \rangle) \qquad i=1, 2
\end{aligned} \tag{41}$$

The Lagrange function is constructed by introducing two sets of lagrange multipliers  $\lambda_i$  ( $i=1,2$ ):

$$L = J + \int_T \int_V \sum_{i=1}^2 \lambda_i \left\{ \begin{aligned} & \partial_t (m \langle H \rangle \langle C_i \rangle) - \partial_z (m \langle H^{-1} \rangle \langle D_v \rangle \partial_z \langle C_i \rangle) \\ & + \partial_x [ (m_y \langle H \rangle u_{ET} + \partial_y \psi \partial_z \chi - \partial_z \psi \partial_y \chi) \langle C_i \rangle ] \\ & + \partial_y [ (m_x \langle H \rangle v_{ET} + \partial_z \psi \partial_x \chi - \partial_x \psi \partial_z \chi) \langle C_i \rangle ] \\ & + \partial_z [ (mw_{ET} + \partial_x \psi \partial_y \chi - \partial_y \psi \partial_x \chi) \langle C_i \rangle ] \end{aligned} \right\} dv dt \tag{42}$$

where the cost function  $J$  is defined as:

$$J = \frac{1}{2} \int_V \sum_{i=1}^2 [B_i(\langle C_i \rangle) - \langle C_i^{obs} \rangle]^T W_i [B_i(\langle C_i \rangle) - \langle C_i^{obs} \rangle] dv \tag{43}$$

The adjoint equations for  $\psi$  and  $\chi$  can be obtained by substituting Eq. (42) into Eq. (16) and further rearranging using the relationship of Eq. (40):

$$\begin{aligned}
& -\partial_t (m \langle H \rangle \lambda_i) - \partial_x ( (m_y \langle H \rangle u_{ET} + \partial_y \psi \partial_z \chi - \partial_z \psi \partial_y \chi) \lambda_i ) \\
& - \partial_y ( (m_x \langle H \rangle v_{ET} + \partial_z \psi \partial_x \chi - \partial_x \psi \partial_z \chi) \lambda_i ) \\
& - \partial_z ( (mw_{ET} + \partial_x \psi \partial_y \chi - \partial_y \psi \partial_x \chi) \lambda_i ) \\
& - \partial_z (m \langle H^{-1} \rangle \langle D_v \rangle \partial_z \lambda_i) = W_i (\langle C_i^{obs} \rangle - B_i(\langle C_i \rangle))
\end{aligned} \tag{44}$$

The gradients of the cost function  $J$  with respect to  $\psi$  and  $\chi$  then can be derived in a similar way to  $(A_x, A_y, A_z)$ :

$$\begin{aligned}
\partial_{\psi} J = \sum_{i=1}^2 [ & -\partial_z \chi \partial_y (\langle C_i \rangle \partial_x \lambda_i) + \partial_y \chi \partial_z (\langle C_i \rangle \partial_x \lambda_i) \\
& -\partial_x \chi \partial_z (\langle C_i \rangle \partial_y \lambda_i) + \partial_z \chi \partial_x (\langle C_i \rangle \partial_y \lambda_i) \\
& -\partial_y \chi \partial_x (\langle C_i \rangle \partial_z \lambda_i) + \partial_x \chi \partial_y (\langle C_i \rangle \partial_z \lambda_i) ]
\end{aligned} \tag{45}$$

and

$$\begin{aligned}
\partial_{\chi} J = \sum_{i=1}^2 [ & -\partial_y \psi \partial_z (\langle C_i \rangle \partial_x \lambda_i) + \partial_z \psi \partial_y (\langle C_i \rangle \partial_x \lambda_i) \\
& -\partial_z \psi \partial_x (\langle C_i \rangle \partial_y \lambda_i) + \partial_x \psi \partial_z (\langle C_i \rangle \partial_y \lambda_i) \\
& -\partial_x \psi \partial_y (\langle C_i \rangle \partial_z \lambda_i) + \partial_y \psi \partial_x (\langle C_i \rangle \partial_z \lambda_i) ]
\end{aligned} \tag{46}$$

Even though Eq. (41) provides a system for solving  $\psi$  and  $\chi$  and thus gives the solution of the Lagrangian mean transport velocity by Eq. (39), the form of Eq. (41) indicates that  $\psi$  and  $\chi$  are nonlinearly coupled, which might lead to an ill-conditioned problem and slow down the convergence rate in the minimization process. Another shortcoming of this approach is that if the two scalar gradients are parallel or one of the gradients vanishes in a region (*i.e.*,  $\nabla C_1 \times \nabla C_2 = 0$ ), the scalar measurements do not provide sufficient information to determine the transport velocity (Pearlstein and Carpenter, 1995). In other words, the distributions of two tracers should not be similar or homogeneous in order to provide sufficient information to retrieve the transport velocity. Unfortunately in estuarine systems, the gradient of candidates for the second tracer field, such as temperature and suspended sediment, in addition to having vertical boundary fluxes are generally parallel to that of salinity in a similar spatial manner. The major dissimilarity of the gradients of temperature or suspended sediment and salinity is in the very surface or the bottom layer due to the vertical boundary conditions.



### 3.7 Conclusions

In this Chapter, a variational data assimilation formalism for retrieving the effective transport flow field is developed with a long-term transport model. The variational inverse method is tested in a idealized vertical two-dimensional estuary in a series of twin experiments. A vector potential, which can be considered as the compensation of the Eulerian transport flow to the Lagrangian transport flow is introduced and chosen as the control variable in the inverse model. The long-term tracer distribution is used as observation data. We have demonstrated that the proposed inverse formalism can successfully retrieve the true solution for vector potential and well reproduce the tracer distribution. We also found that the inverse model works most efficiently wherever the advection transport is important in the tracer data distribution. In the area where advective transport is not important, the accuracy of the recovered solution will be decreased and the minimization convergence speed may strongly be affected.

Experiments with sparse data showed that the inverse model has the capability to retrieve very satisfactory solutions when a penalty term is introduced to smooth out the spatial oscillations. The impact of different values of the penalty coefficient on the retrieved solution is investigated. Experiments with sparse data are important because in reality we need to decide the data density required for the inverse model to work effectively. Experiments with noisy data showed that the inverse model is very sensitive to the accuracy of the data. However, reasonable solutions still can be retrieved when a stronger penalty term is considered. It is noteworthy that in reality, the choice of the penalty coefficient has to be made in a careful manner since in real applications, the true

solution is actually unknown. Difficulties could be encountered in determining the best penalty coefficient in applications using field data.

For the 3-D problem, measurements of two different tracers are required to provide sufficient information to retrieve the Lagrangian mean transport velocity. However, the decomposition form (4) for the Lagrangian mean transport velocity leads to the inverse problem being underdetermined because there are three unknowns ( $A_x, A_y, A_z$ ) but only two transport constraints. When an alternative Helmholtz decomposition (37) is considered, two scalars  $\psi$  and  $\chi$  are introduced to define a unique solution system. With this approach, which merits further investigation, difficulties may arise in the minimization process due to the fact that  $\psi$  and  $\chi$  are nonlinearly coupled in (39) and the distributions of two tracers are required to be different ( $\nabla C_1 \times \nabla C_2 \neq 0$ ).

Table 1 Verification of the gradient  
of the cost function

| $\alpha$   | $\Phi(\alpha)$ |
|------------|----------------|
| $10^{-6}$  | 1.4794832852   |
| $10^{-7}$  | 1.0482399890   |
| $10^{-8}$  | 1.0050569468   |
| $10^{-9}$  | 1.0007380842   |
| $10^{-10}$ | 1.0003061296   |
| $10^{-11}$ | 1.0002623018   |
| $10^{-12}$ | 1.0002515838   |
| $10^{-13}$ | 1.0001872050   |
| $10^{-14}$ | .9995498386    |
| $10^{-15}$ | .9931691676    |
| $10^{-16}$ | .9296191924    |
| $10^{-17}$ | .2893962624    |

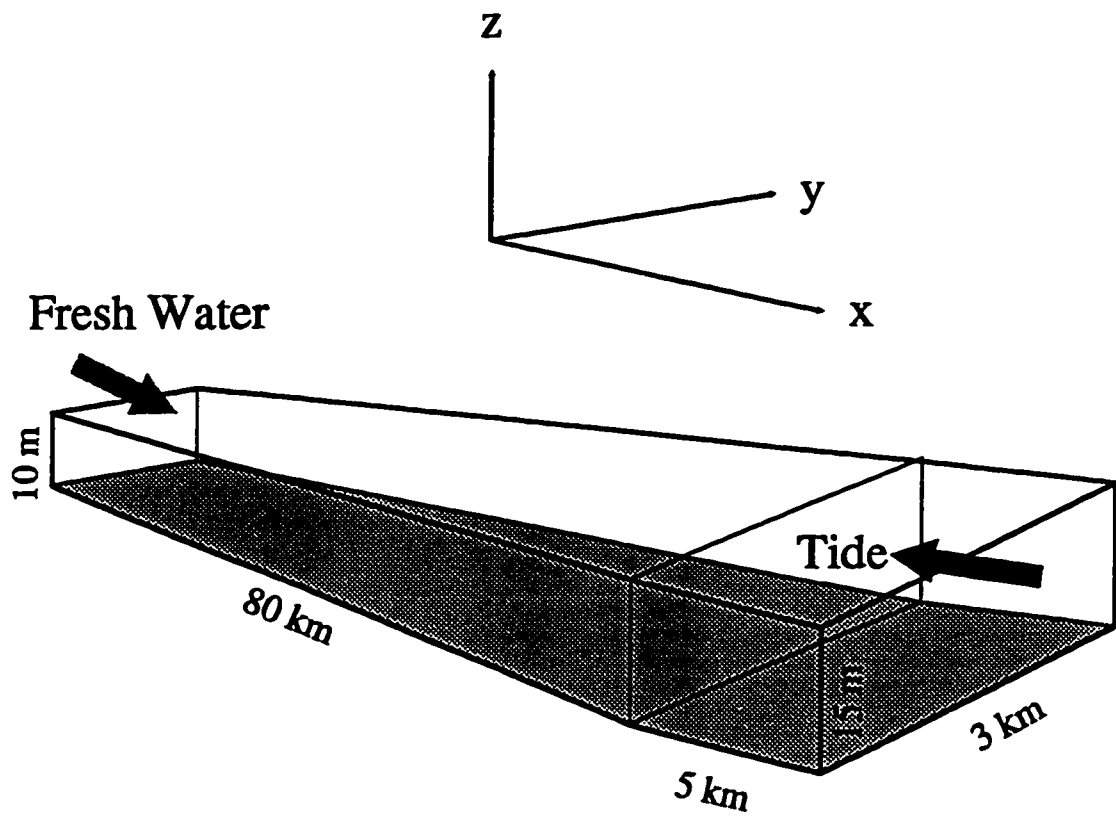
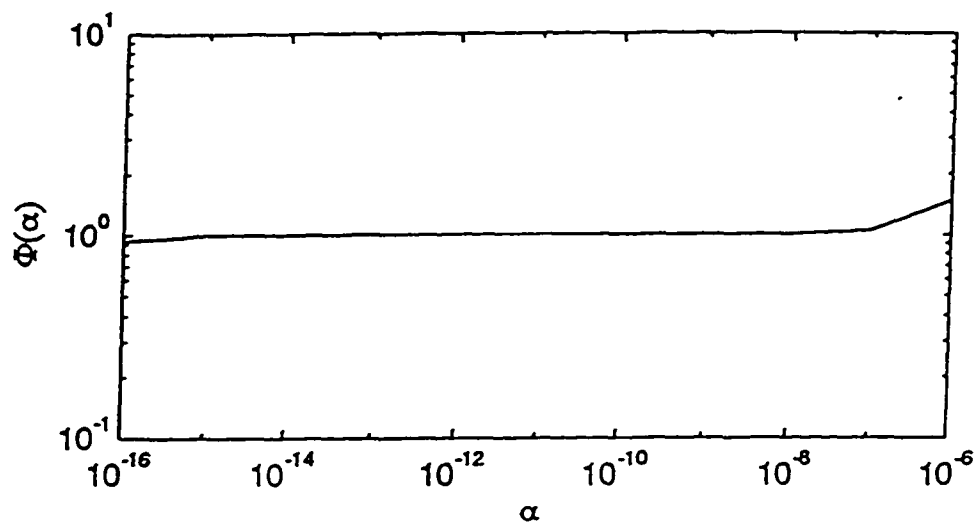
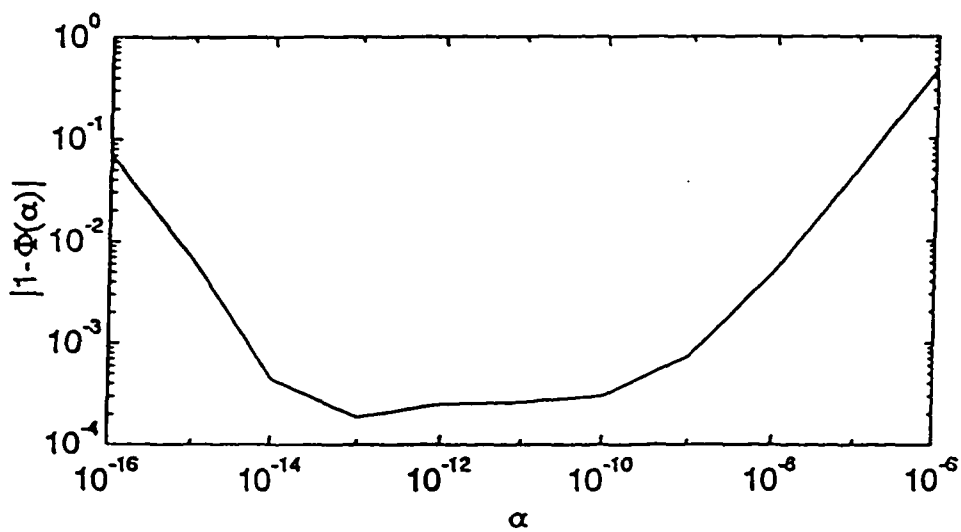


Fig. 1 Schematic of the geometry of an idealized estuary

Fig. 2 Variation of function  $\Phi(\alpha)$ Fig. 3 Residual of function  $\Phi(\alpha)$

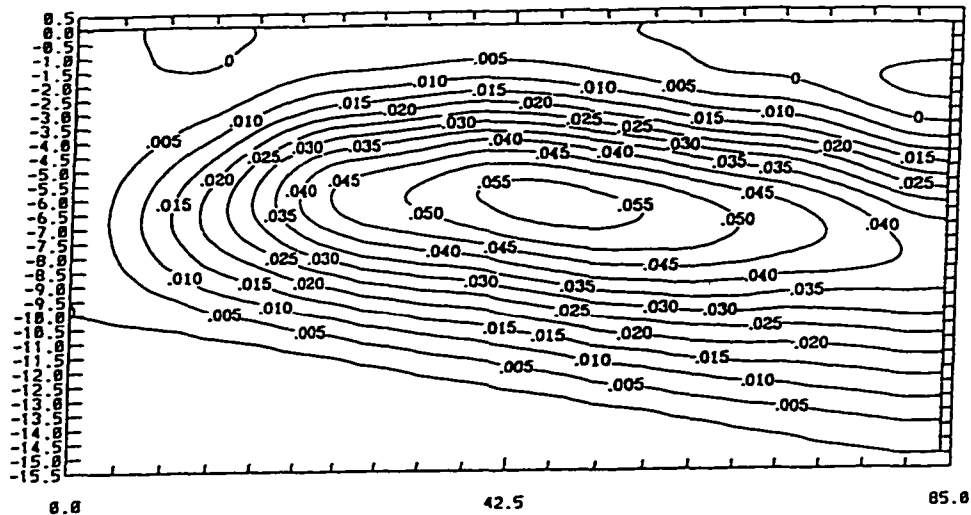


Fig. 4 True solution of y-component of vector potential  $A_y$  ( $\text{m}^3/\text{s}$ )

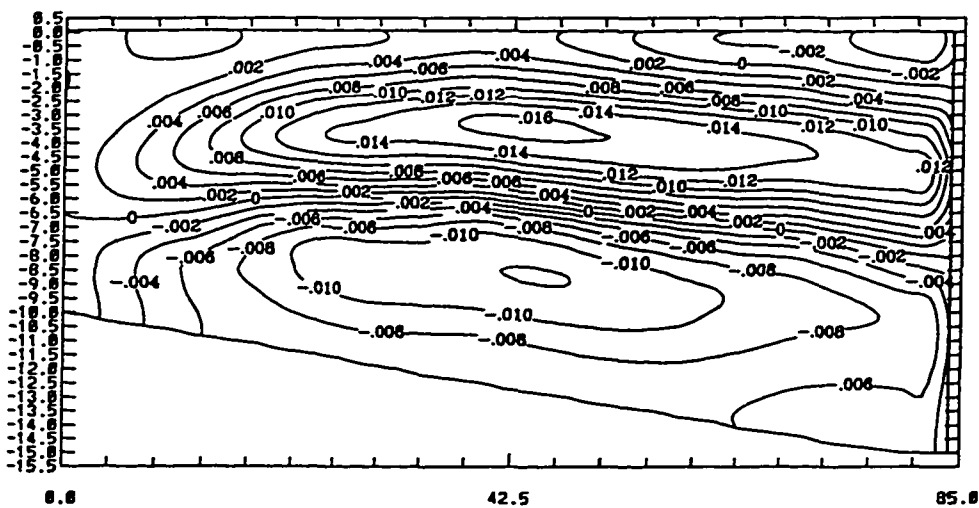


Fig. 5 Distribution of vector potential transport field ( $\text{m}/\text{s}$ )

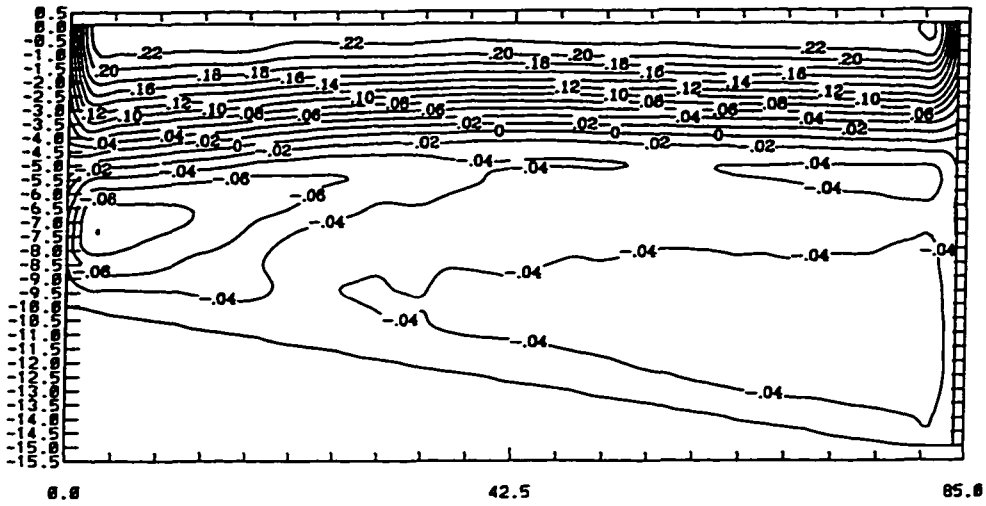


Fig. 6 Distribution of the Eulerian mean transport field (m/s)

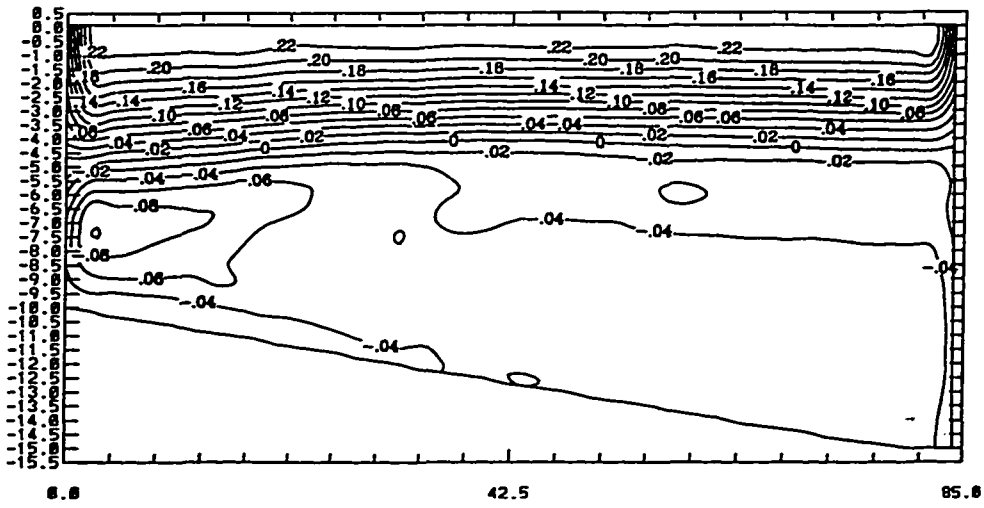


Fig. 7 Distribution of the Lagrangian mean transport field (m/s)

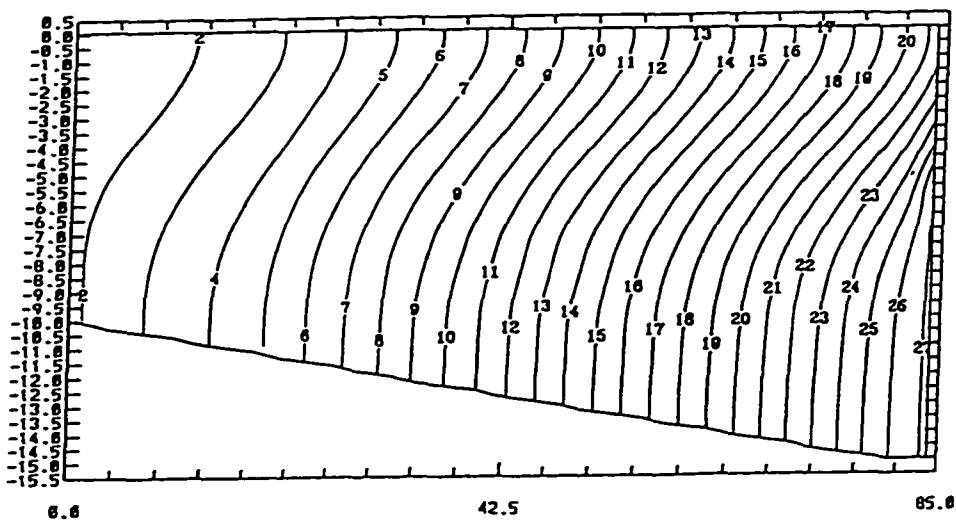


Fig. 8 Distribution of 'observed' salinity (ppt)

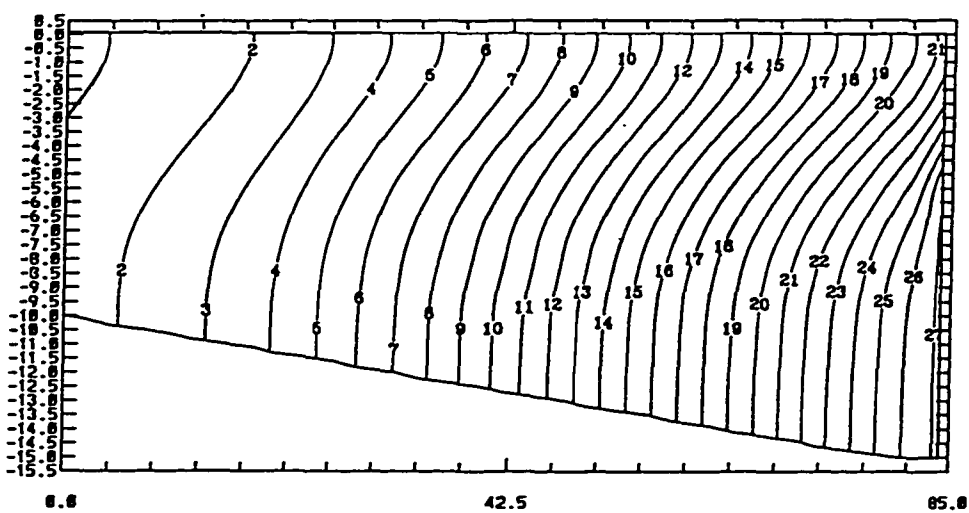


Fig. 9 Distribution of initial salinity (ppt)



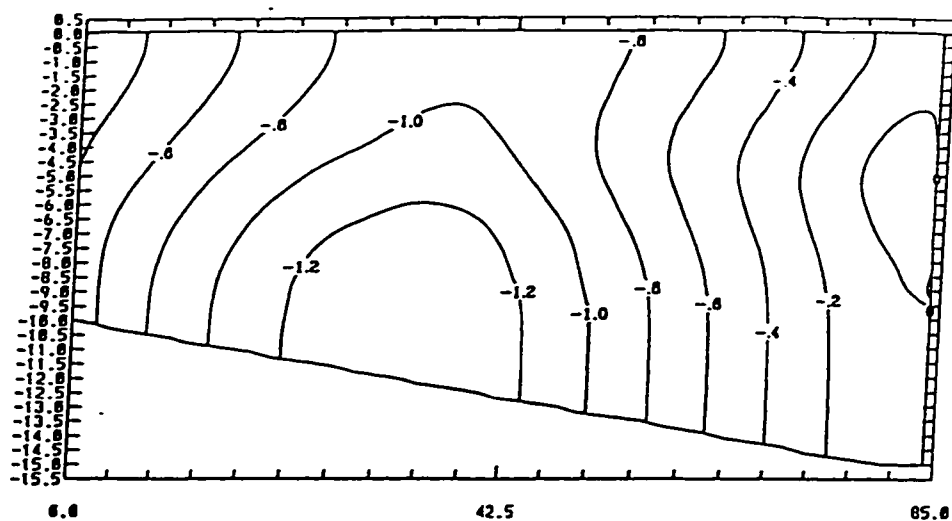


Fig. 10 Initial salinity misfit (ppt) for basic model test (case 1)

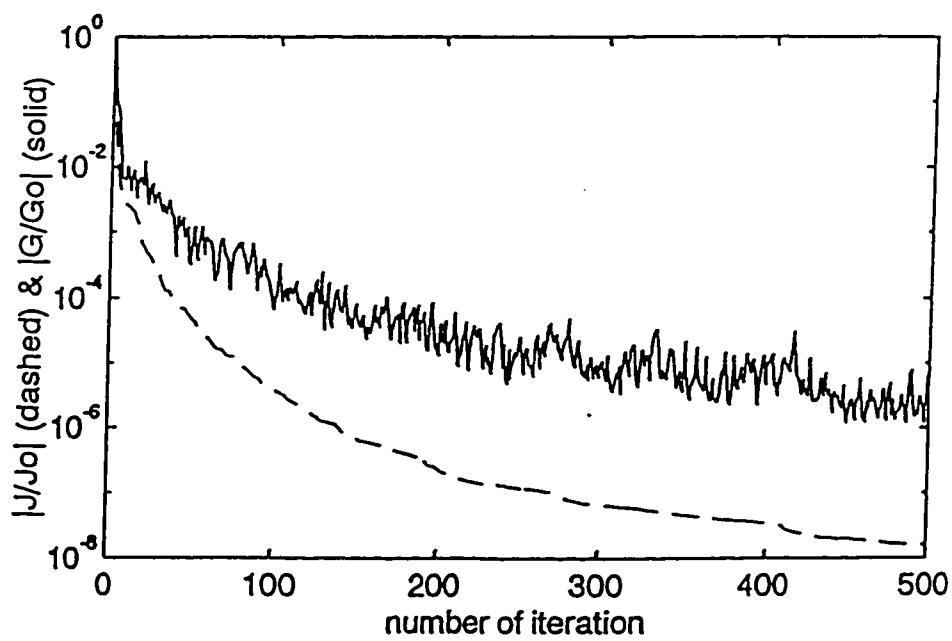


Fig. 11 Variations of  $|J/J_0|$  and  $|\nabla J/\nabla J_0|$  in terms of number of iterations

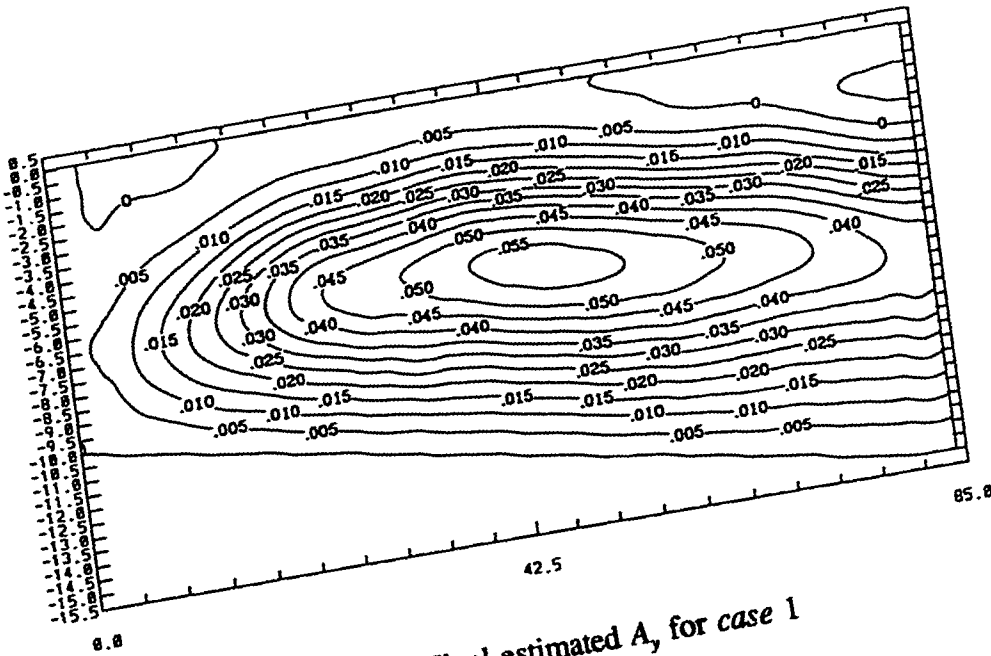


Fig. 12 Final estimated  $A_y$  for case 1

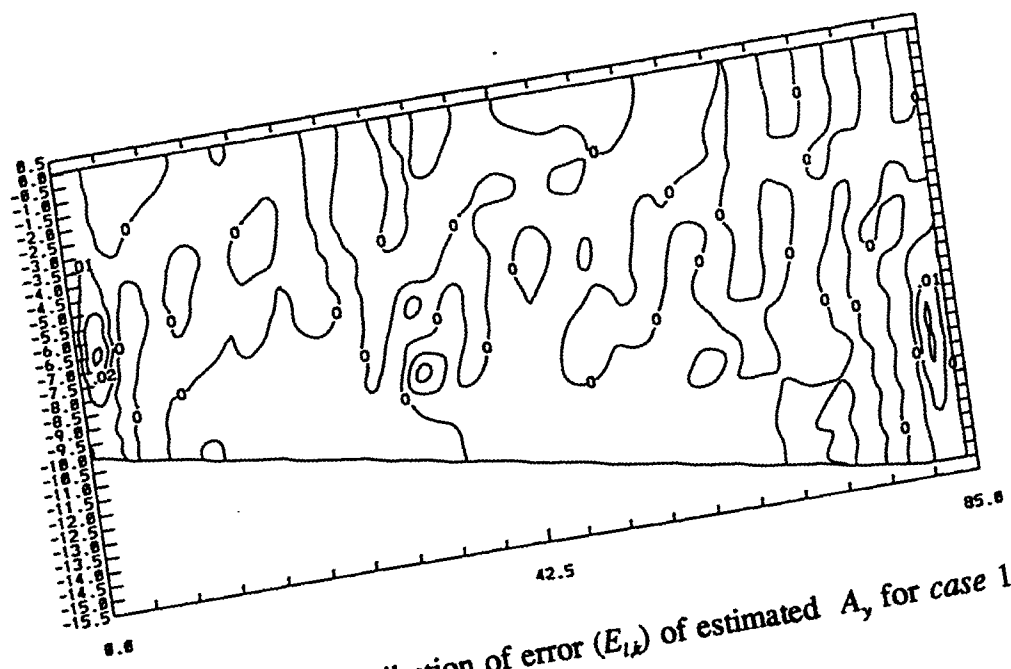


Fig. 13 Final distribution of error ( $E_{ik}$ ) of estimated  $A_y$  for case 1

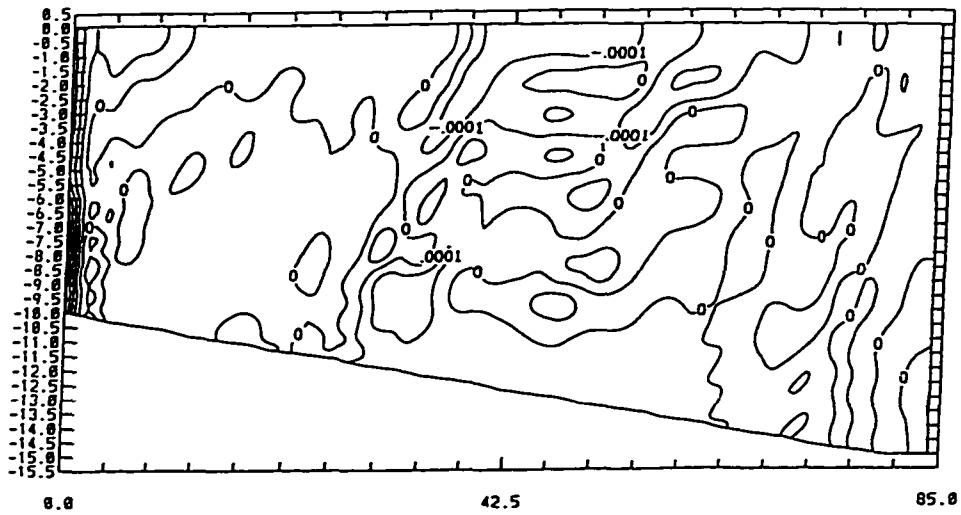


Fig. 14 Final salinity misfit (ppt) for case 1

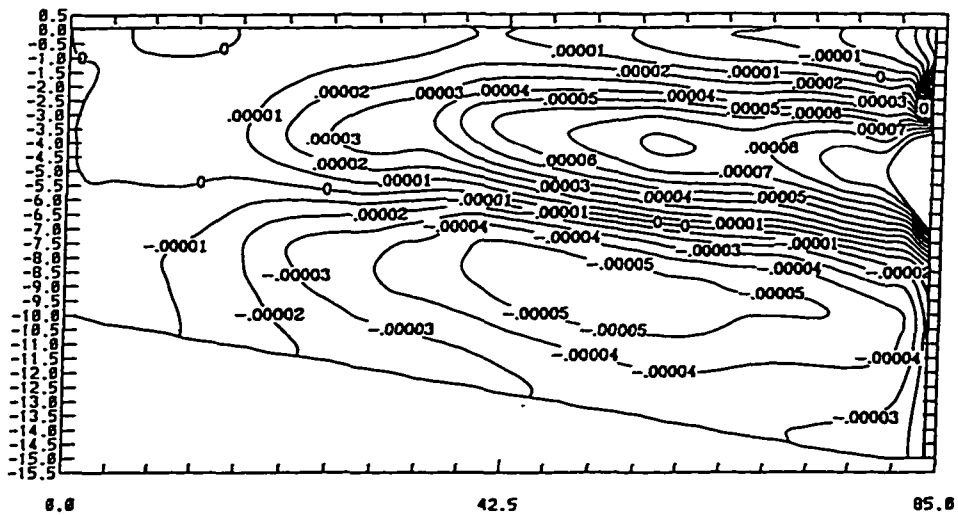


Fig. 15 Distribution of the advection term due to  $A_y$

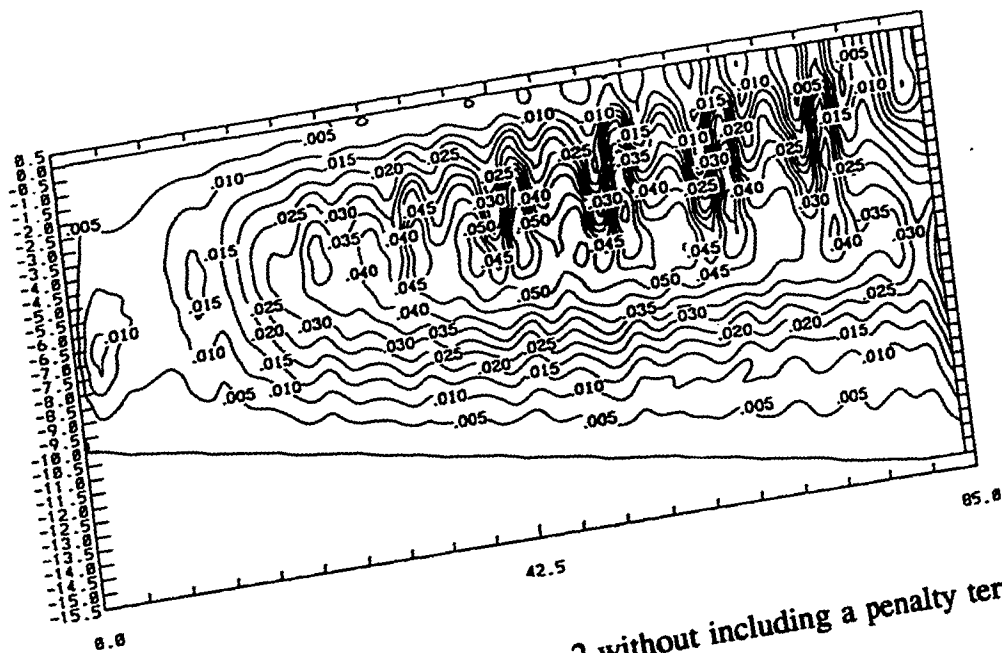


Fig. 16 Final estimated A, for case 2 without including a penalty term

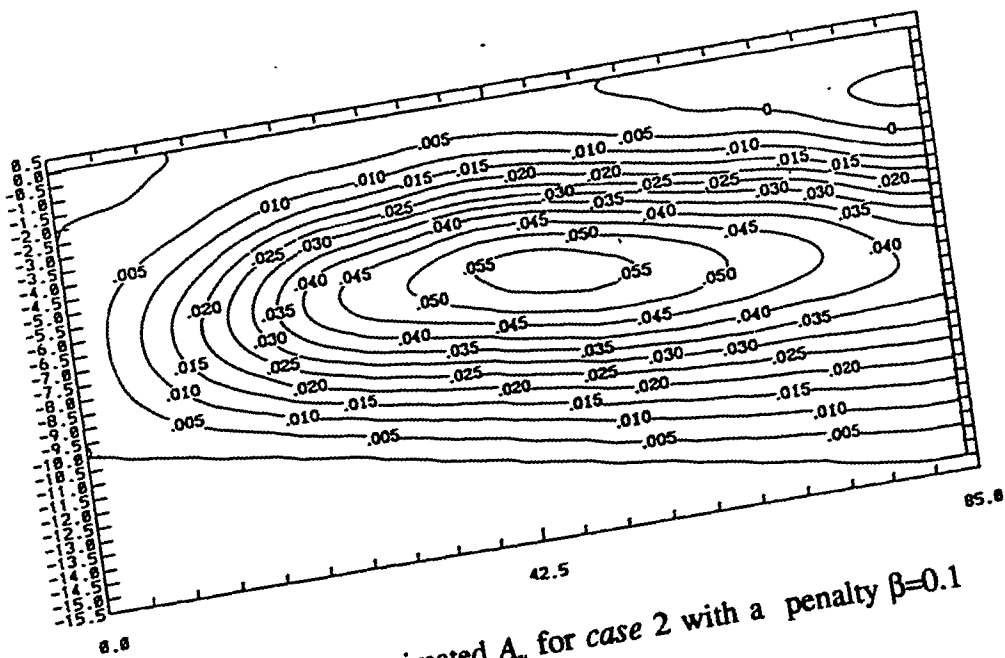


Fig. 17 Final estimated A, for case 2 with a penalty  $\beta=0.1$

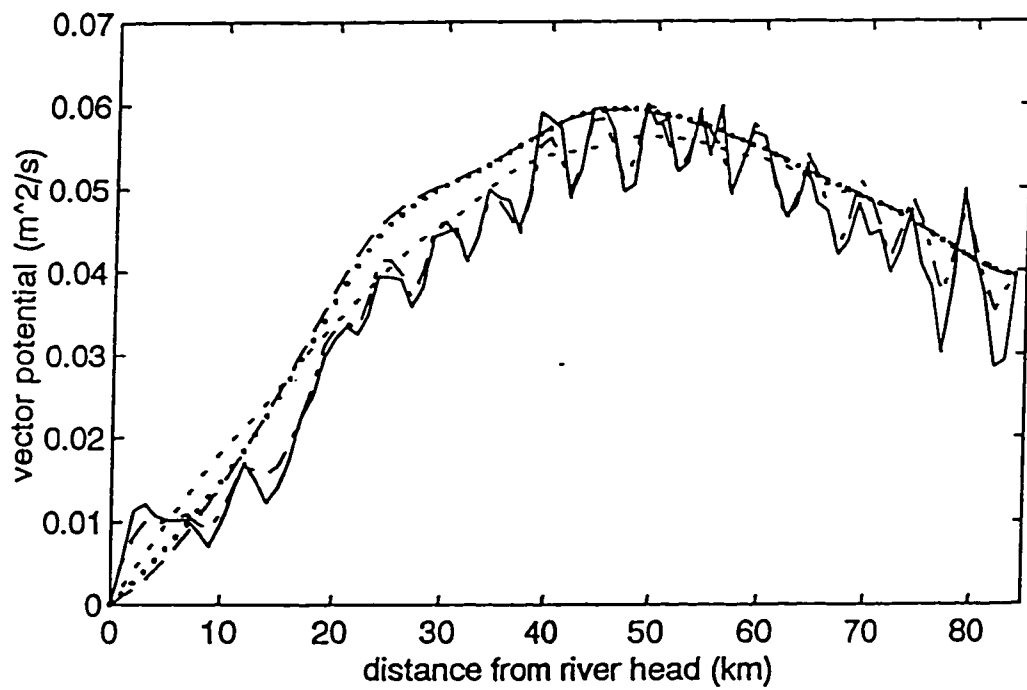


Fig. 18 Comparisons of the final estimated  $A_1$  along the river at mid-level for *case 2* with different values of penalty coefficient  $\beta$ : long dashed line for true solution; solid line for  $\beta=0$ ; dashed and dotted line for  $\beta=0.01$ ; dotted line for  $\beta=0.1$ ; short dashed line for  $\beta=10$

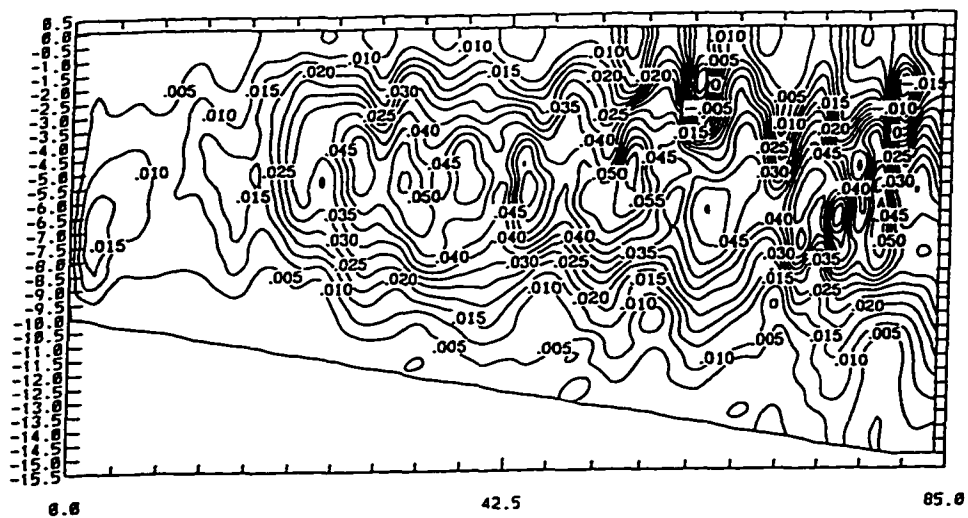


Fig. 19 Final estimated  $A_y$  for case 3 without including a penalty term

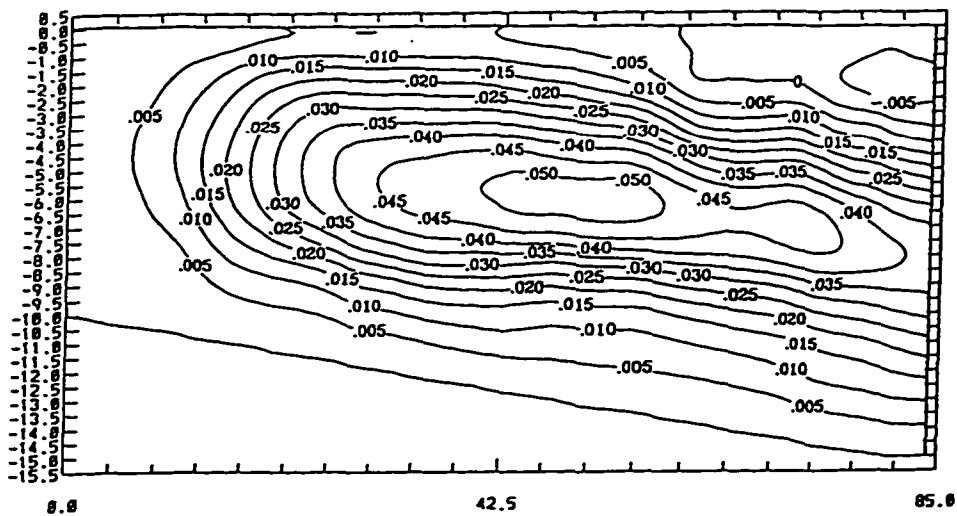


Fig. 20 Final estimated  $A_y$  for case 3 with a penalty  $\beta=10$

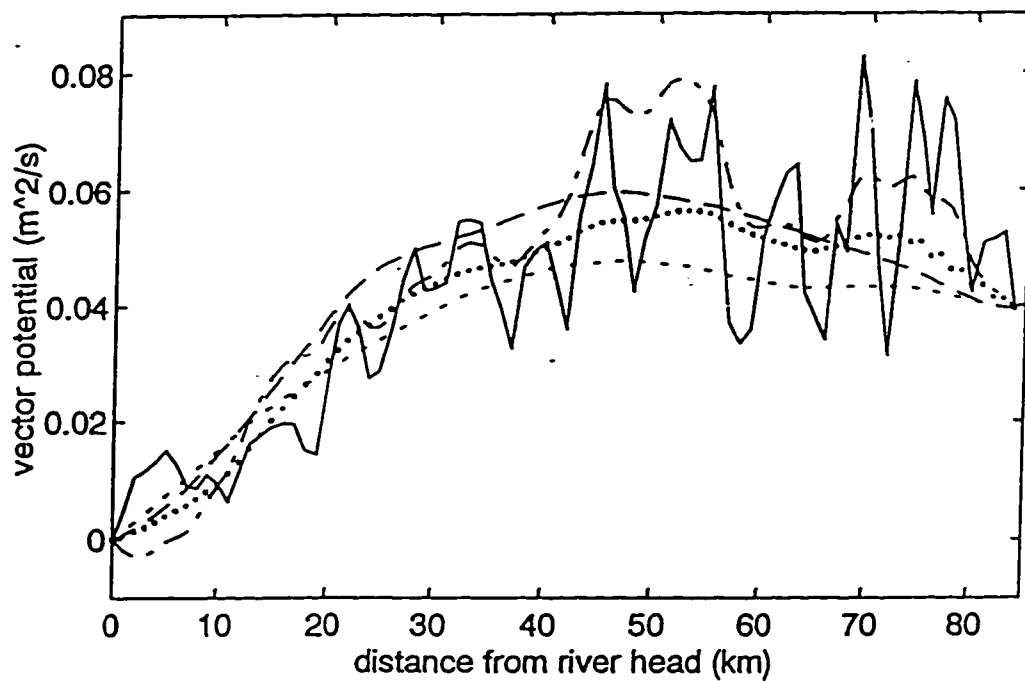


Fig. 21 Comparisons of the final estimated  $A_y$  along the river at mid-level for *case 3* with different values of penalty coefficient  $\beta$ : long dashed line for true solution; solid line for  $\beta=0$ ; dashed and dotted line for  $\beta=1$ ; dotted line for  $\beta=10$ ; short dashed line for  $\beta=100$

## 4 DETERMINATION OF THE TRACER OPEN BOUNDARY CONDITION

### 4.1 Introduction

One of the critical factors affecting open-ocean or coastal and estuarine modeling is the specification of open boundary conditions. Improper specifications of open boundary conditions can result in ill-posed problems and such problems are notorious for primitive-equation models (Bennett, 1992). There have been some studies to seek better specifications of open boundary conditions by using a data assimilation approaches to improve model outputs. For example, Bennett and McIntyre (1982) applied a weighted variational formulation to retrieve the optimal boundary conditions in a open-ocean tidal model. Shulman and Lewis (1995) used a data assimilation approach to prescribe the open boundary conditions for barotropic models. In their studies, minimization is based on the change of flux of energy through the open boundary. Evensen (1993) used the extended Kalman filter to assimilate data in the quasi-geostrophic Ocean Model to achieve a well-posed boundary value problem, in which the stream function must be specified at all boundaries and the vorticity must be specified at the inflow boundaries. Seiler (1993) estimated the stream function and the relative vorticity at four open boundaries in a quasi-geostrophic ocean model for a mid-latitude jet by assimilating the Geosat data with the adjoint method. Lardner (1993) presented a variational inverse method to retrieve the optimal open boundary conditions for a numerical tidal model. Ten Brummerlhuis *et al.* (1993) applied data assimilation techniques to identify the open boundary conditions in shallow sea models. Zou *et al.*, (1995) provided an efficient scheme for free boundary



conditions for an ocean model. Spitz (1995) assimilated tide gauge data into a two-dimensional model of the Chesapeake Bay to optimally estimate the bottom drag coefficient, wind stress and surface elevation at the open boundary. Even though there are some studies on determining the optimal open boundary conditions by data assimilation approaches in oceanography, no studies have been performed on determining the tracer open boundary conditions in transport models. In this Chapter, a variational data assimilation scheme is developed to determine the open boundary conditions for salinity transport problem in tidal environment.

In an intra-tidal salinity transport model, the traditional treatment of the inflow salinity open boundary condition is to specify a maximum salinity boundary value  $C_{bmax}$  and a recovery time  $t_R$  within which the salinity open boundary value recovers from a minimum value at slack water after ebb to its maximum value  $C_{bmax}$  (see Fig. 22). When observations at the open boundary are not available, estimations for  $C_{bmax}$  and  $t_R$  must be made based on some previous knowledge or observations at other locations. The fine tuning of such open boundary conditions is generally made manually by using a trial-and-error approach through the comparison of field observations and model counterparts and could be very time consuming. In many cases such a rough estimation would not assure satisfactory model outputs. The objective of this Chapter is to develop a variational data assimilation scheme to estimate optimally the maximum salinity open boundary value  $C_{bmax}$  and the recovery time  $t_R$ , so that the model best fits observations. Control of open conditions increases the dimension of the control variable by adding at every time step all the boundary grid-values of the variable. Thus the condition number of the Hessian

of the cost function with respect to control variables increases considerably.

## 4.2 Model Description

The governing equation used here for the salinity transport process is the same as Eq. (3) with the source/sink  $Q$  equal to zero:

$$\begin{aligned} \partial_t (mHC) + \partial_x (m_y H u C) + \partial_y (m_x H v C) + \partial_z (m w C) \\ = \partial_x (m H^{-1} D_v \partial_z C) \end{aligned} \quad (47)$$

For intra-tidal salinity transport problems, the inflow salinity open boundary condition can be specified as:

$$C_b = \begin{cases} C_E + \frac{(C_{bmax} - C_E)}{t_R} (t - t_E) & t_E \leq t \leq t_E + t_R \\ C_{bmax} & t_E + t_R \leq t \leq t_F \end{cases} \quad (48)$$

where  $t_E$  is the time at slackwater after ebb and  $C_E$  is the boundary salinity at  $t_E$ ,  $t_F$  is the time at slackwater after flood. During ebb (outflow), the boundary salinity value is determined by the advection of upstream salinity, *i.e.*, the time varying term is balanced by the horizontal advection terms:

$$\partial_t (mHC) + \partial_x (m_y H u C) + \partial_y (m_x H v C) = 0 \quad (49)$$

Choosing the coordinate system such that the x-direction is towards the east and the y-direction is towards the north and assuming the transverse velocity at the open boundary is equal to zero, then for eastern or western open boundaries, the outflow salinity at the open boundary salinity is determined by:

$$\partial_t (mHC) = -\partial_x (m_y H u C) \quad (50)$$

Similarly, for northern or southern open boundaries, the outflow salinity is determined by:

$$\partial_t (mHC) = -\partial_y (m_x H v C) \quad (51)$$

### 4.3 Adjoint Model And Gradient of The Cost Function

For the salinity open boundary condition problem, the cost function is defined in the spatial and temporal domains as shown in Eq. (12). The Lagrange function  $L$  function is defined by appending the model equation (Eq. (45)) to the cost function as a dynamic constraint:

$$L(C, \lambda, P) = J + \int_T \int_V \lambda \left\{ \begin{array}{l} \partial_t (mHC) + \partial_x (m_y H u C) + \partial_y (m_x H v C) \\ + \partial_z (m w C) - \partial_z (m H^{-1} D_v \partial_z C) \end{array} \right\} dV dT \quad (52)$$

where  $P$  represents the control variables to be estimated ( $C_{bmax}$  and  $t_R$ ). The adjoint model can be obtained by simply setting the derivative with respect to the model variable  $C$  equal to zero:

$$\begin{aligned} -\partial_t (mH\lambda) - \partial_x (m_y H u \lambda) - \partial_y (m_x H v \lambda) - \partial_z (m w \lambda) \\ - \partial_z (m H^{-1} D_v \partial_z \lambda) = W(C^{obs} - C) \end{aligned} \quad (53)$$

The Lagrange multiplier  $\lambda$  can be solved by integrating the adjoint model Eq. (51) backward in time. With the information for  $C$  and  $\lambda$  we can calculate the gradient of the cost function by setting  $\partial_p L=0$ :

$$\partial_P J = -\partial_P \int_T \int_V \lambda \left\{ \begin{array}{l} \partial_t (mHC) + \partial_x (m_y HuC) + \partial_y (m_x HVC) \\ + \partial_z (mWC) - \partial_z (mH^{-1} D_v \partial_z C) \end{array} \right\} dVdT \quad (54)$$

Since the inflow open boundary condition Eq. (48) enters the governing equation only from the advection terms, Eq. (54) can be simplified as:

$$\partial_P J = -\partial_P \int_T \int_V \lambda [ \partial_x (m_y HuC) + \partial_y (m_x HVC) ] dVdT ; \quad P = C_{bmax}, t_R \quad (55)$$

In numerical modeling, all the formulations are in discrete forms instead of continuous forms. In order to derive the formula for the gradients of the cost function with respect to  $C_{bmax}$  and  $t_R$ , it is necessary to re-write Eq. (55) in a discrete form. In the present study,  $C_{bmax}$  and  $t_R$  are allowed to vary at all grid cells across the open boundary but remain uniform vertically. We will use the eastern boundary as an example in the following discussion. Derivations of formulations for western, northern and southern open boundaries are similar. Assume there are  $NE$  grid cells across the eastern boundary and let  $LBE(i)$  ( $i=1, \dots, NE$ ) denote the horizontal cell index of the eastern boundary. In an up-wind scheme, the discrete form for the advection in x-direction at interior grid cells next to the eastern open boundary grid cells during the period of flood ( $u_{LBE(i)}^n < 0$ ) is:

$$\begin{aligned} [\partial_x (m_y HC)]_{LBE(i)-1, k}^n &= (m_y Hu)_{LBE(i), k}^n (C_b)_{LBE(i), k}^n \\ &- 0.5 \times \left\{ [(m_y Hu)_{LBE(i)-1, k}^n + |(m_y Hu)_{LBE(i)-1, k}^n|] C_{LBE(i)-2, k}^n \right. \\ &\left. + [(m_y Hu)_{LBE(i)-1, k}^n - |(m_y Hu)_{LBE(i)-1, k}^n|] C_{LBE(i)-1, k}^n \right\} ; \quad i=1, \dots, NE \end{aligned} \quad (56)$$

where  $C_b$  is defined by Eq. (48),  $k$  is the vertical grid index, and  $n$  is the  $n$ th time step.

Assuming the integration of the forward model (Eq. (47)) in time consists of  $M$  tidal

cycles, then substituting Eq. (56) into Eq. (55) and replacing  $C_{bmax}$  by Eq. (48) we can obtain the gradients of  $J$  with respect to  $C_{bmax}$  and  $t_R$  at open boundary cell  $LBE(i)$ :

$$\begin{aligned} \partial_{C_{bmax}(i)} J = & - \sum_{m=1}^M \sum_{k=1}^K \left[ \sum_{t=t_E(m)}^{t_E(m)+t_R(i)} (\lambda m_y H U)_{LBE(i),k}^n \left( \frac{t-t_E(m)}{t_R(i)} \right) \right. \\ & \left. - \sum_{t=t_E(m)+t_R(i)}^{t_E(m)} (\lambda m_y H U)_{LBE(i),k}^n \right] ; \quad i=1, \dots, NE \end{aligned} \quad (57)$$

and

$$\begin{aligned} \partial_{t_R(i)} J = & \sum_{m=1}^M \sum_{k=1}^K \sum_{t=t_E(m)}^{t_E(m)+t_R(i)} (\lambda m_y H U)_{LBE(i),k}^n \left( \frac{t-t_E(m)}{t_R(i)^2} \right) \\ & \times [C_{bmax}(i) - C_E(m)] ; \quad i=1, \dots, NE \end{aligned} \quad (58)$$

In numerical modelling,  $t_R$  actually is a discontinuous step-type variable instead of a continuous variable. The value of  $t_R$  can only change by an interval of one time step  $\Delta t$ . The recovery time for the inflow salinity open boundary conditions in the numerical model is specified by the number of time steps which is defined by  $N_R = t_R / \Delta t$ . So the integer  $N_R$  will be the control variable in the variational inverse procedure. Unfortunately, this causes difficulties in the minimization process because in the minimization algorithm all control variables are treated as real numbers. Further discussion on this issue will be followed in the next section.

## 4.4 Model Tests in An Idealized 3-D Estuary

### 4.4.1 Model Setup

The inverse model for the salinity open boundary problem is tested in an idealized

3-D semi-enclosed estuary. The horizontal geometry is very similar to that of the 2-D estuary in the tracer inverse problem (see Fig. 1). The total length of the estuary is 100 km. The estuary is 1 km wide at the head and 3 km wide at a distance of 80 km from the head and with the width remaining constant to the mouth. The water depth is specified such that the depth increases linearly from the head to 80 km from the head and then becomes constant. The cross-section profile of the water depth is assumed symmetric about the center of the channel and defined by the following exponential function:

$$h(y') = h_c \exp\left[ \left| \frac{2y'}{B_o} - 1 \right| \ln\left( \frac{h_s}{h_c} \right) \right]; \quad y' \in [0, B_o] \quad (59)$$

where  $y'$  is the relative coordinate originated at the river side and across the channel;  $B_o$  is the surface width of the channel;  $h_c$  is the water depth at the center of the channel ( $y'=B_o/2$ );  $h_s$  is the water depth at both sides of the channel ( $y'=0$  and  $B_o$ ). Values used for the test are:  $h_s=3$  m and  $h_c=5$  at the head of the estuary and  $h_s=10$  m and  $h_c=15$  m at the mouth. The  $x$ -coordinate origin is at the head of the estuary and directed seaward. The depth profiles at the head ( $x=0$  km) and at the mouth ( $x=100$  km) are:

$$h(y') = 5 \exp\left[ \left| \frac{2y'}{B_o} - 1 \right| \ln\left( \frac{3}{5} \right) \right]; \quad y' \in [0, B_o], \quad x=0 \text{ km} \quad (60)$$

and

$$h(y') = 15 \exp\left[ \left| \frac{2y'}{B_o} - 1 \right| \ln\left( \frac{2}{3} \right) \right]; \quad y' \in [0, B_o], \quad x=100 \text{ km} \quad (61)$$

The profiles of Eqs. (60-61) are shown in Fig. 23(a&b). The depth profiles at any

location between  $x=80$  km and  $x=100$  km (the mouth) are the same. The depth profiles at any location between  $x=0$  km and  $x=80$  km will be linearly interpolated by the profiles at  $x=0$  and  $x=80$  km (Eqs. (60-61)):

$$h(y') = \frac{x}{80} \left\{ 15 \exp \left[ \left| \frac{2y'}{B_o} - 1 \right| \ln \left( \frac{2}{3} \right) \right] - 5 \exp \left[ \left| \frac{2y'}{B_o} - 1 \right| \ln \left( \frac{3}{5} \right) \right] \right\} \quad (62)$$

$$+ 5 \exp \left[ \left| \frac{2y'}{B_o} - 1 \right| \ln \left( \frac{3}{5} \right) \right] ; \quad y' \in [0, B_o], \quad x \in [0, 80]$$

The geometry is shown in Fig. 24. There are 100 grid cells longitudinally, 5 cells laterally and 5 layers vertically. The horizontal grid is a curvilinear-orthogonal grid generated by the Grid Generating Preprocessor Code developed at VIMS. The physical horizontal grid map is shown in Fig. 25. A constant freshwater discharge (200 m<sup>3</sup>/s) is specified at the head and a single frequency semi-diurnal tide ( $M_2$ ) with an amplitude of 0.3 m is applied at the eastern open boundary (mouth). Because the maximum width of the estuary is only 3 km, the Coriolis force is neglected in the hydrodynamic model. The hydrodynamic model and transport model were run for 100 tidal cycles to assure that the model reaches equilibrium. The velocity field and spatial distribution of vertical diffusivity  $D_v$  for the last tidal cycle are saved as input for solving the inverse problem. The number of time steps for one tidal cycle ( $M_2$ ) is 180. Since the period of  $M_2$  tide is 12.4206 (hour) = 745.236 (min), the time interval of one step is  $\Delta t = 745.236/180 = 4.1402$  (min). In all the experiments discussed below, the forward transport model (Eq. (47)) is run for 10 tidal cycles to generate salinity observations with the open boundary inflow salinity value set to  $C_{bmax} = 30$  ppt and the recovery time set to  $t_R = 82.804$  min ( $N_R = 20$  time steps) at all 5 open boundary grid cells. As mentioned in the preceding section, in the

numerical model, the number of time steps  $N_R$  ( $t_R = N_R \Delta t$ ) specified for the recovery of the inflow salinity is used instead of the variable  $t_R$ . Therefore  $N_R$  will be the control variable in the minimization algorithm. The "observed" salinity distributions along the channel of the estuary and at cross section  $x=50$  km at 4 different phases of the last tidal cycle are presented in Figs. 26 and 27. Observation data are sampled at five horizontal locations ( $x=50, 60, 70, 80$  and  $90$  km) along the central axis of the estuary channel at the time when slackwater happens at the open boundary. Again, because the observations are generated by the same model, the weighting matrix  $W$  in this study is set to be unity at the sampling grid cells and zero at any other cells:

$$W = \begin{cases} 1 & \text{at data cells} \\ 0 & \text{at other cells} \end{cases} \quad (63)$$

The total number of parameters to be estimated is 10, *i.e.*, 5 salinity open boundary values ( $C_{bmax}$ ) and 5 recovery times ( $t_R$ ) across the open boundary.

#### 4.4.2 Scaling And Preconditioning

One of the main issues in variational data assimilation problems is the convergence rate during minimization processes. The rate is related to the Hessian matrix, which is defined as the second derivatives of the cost function with respect to the control variables. The shape of the cost surface is a function of the eigenvalues and eigenvectors of the Hessian matrix and the speed of convergence can be determined by the Hessian condition number which is defined as the ratio of its maximum and minimum eigenvalues (Thacker 1987; Tziperman and Thacker, 1989; Yang *et al.*, 1995). A



condition number equal to or close to unity means the cost function is spherical-shaped and the Hessian matrix is well-conditioned. When the Hessian matrix is well-conditioned, theoretically only one descent iteration is required to reach the minimum and all control variables are equally well-determined. In order for the minimization algorithm to work efficiently and converge rapidly, the Hessian matrix must be well-conditioned. Conversely, a very large condition number corresponds to the case of highly elliptical constant-cost contours and the problem is then ill-conditioned, which would result in an extremely slow convergence rate in the minimization process. To speed-up convergence in an ill-conditioned problem, preconditioning methods are often used. A simple preconditioning method is to transform control variables to a new set of unknowns so that the transformed Hessian matrix is better conditioned (Navon and de Villiers, 1983; Tziperman and Thacker, 1989; Courtier and Talagrand, 1990; Li *et al.*, 1993, 1994; Navon *et al.*, 1992; Zou and Holloway, 1995). However, for complicated problems, difficulties may be encountered in choosing proper scaling factors and in some cases even a simple scale transformation is not sufficient to improve the Hessian condition. Therefore, more sophisticated scaling methods will be needed to find preconditioning transformations (Gill *et al.*, 1981; Thacker, 1987). Recent work on preconditioners is reviewed by Courtier *et al.* (1994) and Yang *et al.* (1996).

In the present problem, it was found that if the control variables and the gradients are not properly scaled, the minimization process hardly converges. As Navon *et al.* (1992) pointed out, in the minimization algorithm, the control variables should be scaled to similar magnitudes on the order of unity because within the optimization algorithm

convergence tolerances and other criteria are based on an implicit definition of small and large. We choose to scale  $C_{bmax}$  and  $N_R$  by 1/30 and 1/20, respectively. The gradients of the cost function with respect to  $C_{bmax}$  and  $t_R$  at the central cell ( $G_3$ ) are about 5 times greater than those at the side cell ( $G_1$  and  $G_5$ ). This can be explained by the forms of Eqs. (55-56). The gradients at each cell are proportional to the total volume flux at that cell  $(m_y H u)_{LBE(i)}^n$  and also depend on the magnitude of the Lagrange multiplier  $\lambda$ . Because the volume flux at the center of the channel is the strongest due to the nature of the geometry, this also results in the largest  $\lambda$  magnitudes when the driven force ( $W(C^{obs}-C)$  in Eq. (53)) is located at the center of the channel. Also, the gradient with respect to  $C_{bmax}$  is about 2 orders of magnitude greater than that with respect to  $t_R$  at all open boundary cells. In order to transform the gradients close to the same magnitude, we scale the gradient with respect to  $C_{bmax}$  by the scaling vector (0.01, 0.004, 0.002, 0.004, 0.01) and scale the gradient with respect to  $t_R$  by the scaling vector (1, 0.4, 0.2, 0.4, 1) across the open boundary cells ( $G_1, G_2, G_3, G_4$  and  $G_5$ ). In all the experiments presented below, the scaling factors for control variables and for gradients remain the same.

#### 4.4.3 Test with Initial Guess I

Twin experiments in the idealized 3-D estuary were carried out to test the inverse model. In the first experiment, we decrease  $C_{bmax}$  to 25 ppt and increase  $t_R$  to 124.206 min ( $N_R=30$ ) at all 5 boundary grid cells and use these values as initial guesses. The initial salinity misfits at the end of the run at all the sampling locations are shown in Table 2 where  $k=1$  and  $k=5$  represent the bottom layer and surface layer, respectively.

The normalized cost function and gradient norm are plotted in Fig. 28. The final salinity misfits at sampling locations are given in Table 3. As we can see, even though the cost function is not reduced to zero, but the misfits are reduced to the order of  $10^{-4}$  ppt, which is acceptable. Since the Coriolis force is neglected, the flow field and the salinity distribution are symmetric about the central axis of the estuary. For this reason, we only plotted the recovering status of the salinity boundary values and recovery time at grid cell  $G_1$ ,  $G_2$ ,  $G_3$  in Figs. 31(a&b). From Fig. 29a we can see that  $C_{bmax}$  converges to the true solution at all open boundary grid cells. However, Fig. 29b shows some spatial fluctuations in the recovery time  $t_R$  even though all the retrieved solutions tend to converge to the true solution. The main reason for such spatial fluctuations may be due to the way that minimization algorithm handles  $N_R(t_R)$ . Every time a new set of  $C_{bmax}$  and  $N_R$  are estimated by the minimization algorithm,  $N_R$  is a real number instead of an integer. Thus a rounding statement has to be made to convert  $N_R$  output from the minimization algorithm to an integer. Such a treatment actually somewhat distorts the minimization process and may cause oscillations.

The spatial oscillations in  $t_R(N_R)$  can be eliminated by penalty techniques as was demonstrated in Chapter 3. Similar to Eq. (37), consider the following penalized cost function:

$$J_p = J + \frac{1}{2} \beta_1 (\partial_\gamma C_{bmax})^2 + \frac{1}{2} \beta_2 (\partial_\gamma t_R)^2 \quad (64)$$

where  $\gamma$  represents the direction along the open boundary;  $\beta_1$  and  $\beta_2$  are penalty coefficients for  $C_{bmax}$  and  $t_R$ , respectively. The gradients of the penalized cost function

with respect to  $C_{bmax}$  and  $t_R$ . can be calculated by appending an additional term:

$$\beta_1(\partial_\gamma C_{bmax}) \quad (65)$$

and

$$\beta_2(\partial_\gamma t_R) \quad (66)$$

to the gradients of the nonpenalized cost function (Eqs. (57-58)). With penalty coefficients of  $\beta_1=50$  and  $\beta_2=10$ , the minimization process converges much faster than that without penalty (see Fig. 30). The cost function is reduced by 15 orders of magnitude which is close to machine zero. Both parameters converge to true values accurate to 6 digits within 10 iterations (Fig. 31). For use of penalty in cost functions see Zou *et al.* (1992) and Zou *et al.* (1993). The salinity final misfits at all sampling locations are equal to or less than order  $10^{-7}$  (Table 4).

#### 4.4.4 Test with Initial Guess II

In this experiment we start with a different initial guess by increasing  $C_{bmax}$  to 35 ppt and decreasing  $t_R$  to 41.402 min ( $N_R=10$ ). The initial salinity misfits at the end of the run at all the sampling locations are shown in Table 5. Without penalty, the normalized cost function and gradient norm are plotted in Fig. 32 and the final salinity misfits are presented in Table 5. Variations of  $C_{bmax}$  and  $t_R$  are shown in Fig. 33(a&b). Clearly both parameters tend to converge to the true values but again spatial oscillations are observed with  $t_R$  and  $C_{bmax}$  over estimated at the center ( $G_3$ ) and under-estimated at the side ( $G_1$ ). With the penalty added to the cost function, using  $\beta_1=50$  and  $\beta_2=1$ , the minimization

process converges much faster than that without the penalty (see Fig. 34) and all control variables converge to true values accurate to 6 digits within 15 iterations (Fig. 35). The final salinity misfits at all sampling locations are equal to or less than order  $10^{-6}$  (Table 7).

#### 4.5 Conclusions And Future Studies

A variational inverse scheme for the inflow salinity open boundary problem is developed in this Chapter. The maximum inflow salinity value at the open boundary and the recovery time for the inflow salinity boundary condition are used as control variables in the minimization process. The inverse model is tested in an idealized 3-D semi-enclosed estuary. A series of twin experiments were carried out to test the capability of the proposed inverse model for retrieving the optimal salinity open boundary conditions. Experimental results show that reasonable solutions can be retrieved when the control variables and the gradients of the cost function are properly scaled. However, spatial oscillations are observed in the solutions of the recovery time  $t_R$ . This is likely due to the discontinuous characteristic of  $t_R$ , which distorts the minimization process. Further experiments showed that such spatial oscillations can be eliminated by a penalty method. As we pointed out in section 3.7, in real situations, the penalty method has to be used very carefully due to the fact that we don't know how smooth the true solution should be. In the twin experiments, only the  $M_2$  tide is considered. However, since the activation of the inflow salinity open boundary condition is controlled by the local flow directions, such a salinity open boundary condition can be used for multiple tidal

constituents. The period of the validation of the salinity open boundary condition mainly depends on the time scale of the variations of freshwater discharge to the river.

Even though the twin experiments we presented in this Chapter demonstrate that the variational inverse method is a good tool to retrieve the optimal tracer open boundary conditions, there are still many issues related to this problem to be investigated and solved. In particular, the following issues should be addressed in future studies:

1) Vertical varying inflow open boundary conditions. This is very important because stratification is common and significant in estuarine processes, due to the saltier sea water intruding landward near the bottom. In the present study, we assume the maximum inflow salinity value at the surface layer of the open boundary is the same as that at the bottom layer. Such an assumption actually implies that the water column at the open boundary is always well-mixed during the late stage of flood (inflow). Therefore, treating the salinity inflow open conditions at the surface layer and the bottom layer differently would be more realistic.

2) Because the recovery time  $t_R$  is treated as a discontinuous step-type variable in the numerical model, oscillations occur in the minimization process. A smooth and continuous treatment for  $t_R$  should be considered in the future studies.

3) Sensitivity study on data at different locations and different tidal phases. In the present study, the observation data are located at the central axis of the estuary at slack waters (after both ebb and flood). Experiments are necessary to examine how different data locations and tidal phases will affect the retrieved solutions.

4) Sensitivity study on number of data in space and time. More experiments should

be conducted to determine the minimum number of observations in time and space required to retrieve the true solutions.

5) Sensitivity study on noisy data. In reality, the assumption of no noise in observations will not be valid. Real field observations always contains noise due to many complicated mechanisms in estuarine environments as well as instrument characteristics. Therefore it is necessary to test the capability of the inverse model to recover the optimal model state based on noisy observations.

Table 2. Initial salinity misfit (initial guess I)

| Index | I=50       | I=60       | I=70       | I=80       | I=90       |
|-------|------------|------------|------------|------------|------------|
| k=1   | -.2815E-01 | -.1970E+00 | -.7622E+00 | -.1900E+01 | -.3471E+01 |
| k=2   | -.3545E-01 | -.2367E+00 | -.8808E+00 | -.1948E+01 | -.3478E+01 |
| k=3   | -.2229E-01 | -.1541E+00 | -.6432E+00 | -.1582E+01 | -.3002E+01 |
| k=4   | -.6887E-02 | -.6242E-01 | -.2944E+00 | -.8648E+00 | -.2022E+01 |
| k=5   | -.2075E-02 | -.2083E-01 | -.1204E+00 | -.4300E+00 | -.1053E+01 |

Table 3. Final salinity misfit without penalty (initial guess I)

| Index | I=50       | I=60      | I=70      | I=80      | I=90      |
|-------|------------|-----------|-----------|-----------|-----------|
| k=1   | .8767E-06  | .2308E-04 | .1589E-03 | .4583E-03 | .3271E-03 |
| k=2   | .1553E-05  | .3148E-04 | .1971E-03 | .5001E-03 | .3573E-03 |
| k=3   | .7379E-06  | .1761E-04 | .1326E-03 | .4132E-03 | .9474E-04 |
| k=4   | .8906E-07  | .5345E-05 | .5025E-04 | .2096E-03 | .1427E-03 |
| k=5   | -.2107E-07 | .1020E-05 | .1547E-04 | .9058E-04 | .1645E-03 |

Table 4. Final salinity misfit with penalty (initial guess I)

| Index | I=50      | I=60       | I=70       | I=80       | I=90       |
|-------|-----------|------------|------------|------------|------------|
| k=1   | .7690E-08 | -.2657E-07 | -.3651E-06 | -.1198E-05 | .7672E-07  |
| k=2   | .7339E-08 | -.4640E-07 | -.4656E-06 | -.1292E-05 | -.1688E-07 |
| k=3   | .5957E-08 | -.1831E-07 | -.2996E-06 | -.1068E-05 | -.8613E-06 |
| k=4   | .2737E-08 | .6377E-09  | -.9809E-07 | -.5309E-06 | -.1876E-05 |
| k=5   | .1191E-08 | .4025E-08  | -.1986E-07 | -.2045E-06 | -.8075E-06 |



Table 5. Initial salinity misfit (initial guess II)

| Index | I=50      | I=60      | I=70      | I=80      | I=90      |
|-------|-----------|-----------|-----------|-----------|-----------|
| k=1   | .3062E-01 | .2124E+00 | .8115E+00 | .1993E+01 | .3588E+01 |
| k=2   | .3852E-01 | .2547E+00 | .9354E+00 | .2041E+01 | .3595E+01 |
| k=3   | .2425E-01 | .1662E+00 | .6852E+00 | .1663E+01 | .3117E+01 |
| k=4   | .7502E-02 | .6754E-01 | .3153E+00 | .9144E+00 | .2117E+01 |
| k=5   | .2264E-02 | .2262E-01 | .1297E+00 | .4580E+00 | .1109E+01 |

Table 6. Final salinity misfit without penalty (initial guess II)

| Index | I=50      | I=60      | I=70      | I=80       | I=90       |
|-------|-----------|-----------|-----------|------------|------------|
| k=1   | .1252E-03 | .4300E-03 | .2352E-03 | -.1069E-02 | .1022E-01  |
| k=2   | .1445E-03 | .4377E-03 | .3613E-04 | -.1404E-02 | .9781E-02  |
| k=3   | .9843E-04 | .3502E-03 | .2466E-03 | -.1224E-02 | .2899E-02  |
| k=4   | .3550E-04 | .1864E-03 | .3258E-03 | -.3796E-03 | -.5523E-02 |
| k=5   | .1281E-04 | .8343E-04 | .2441E-03 | .1433E-03  | -.1679E-02 |

Table 7. Final salinity misfit with penalty (initial guess II)

| Index | I=50       | I=60      | I=70      | I=80      | I=90      |
|-------|------------|-----------|-----------|-----------|-----------|
| k=1   | .2232E-09  | .2827E-07 | .1943E-06 | .5729E-06 | .2920E-06 |
| k=2   | .1066E-08  | .3869E-07 | .2384E-06 | .6080E-06 | .3283E-06 |
| k=3   | .2196E-09  | .2128E-07 | .1612E-06 | .4999E-06 | .5277E-06 |
| k=4   | -.2357E-09 | .5959E-08 | .6118E-07 | .2566E-06 | .7759E-06 |
| k=5   | -.1959E-09 | .7173E-09 | .1842E-07 | .1089E-06 | .3548E-06 |

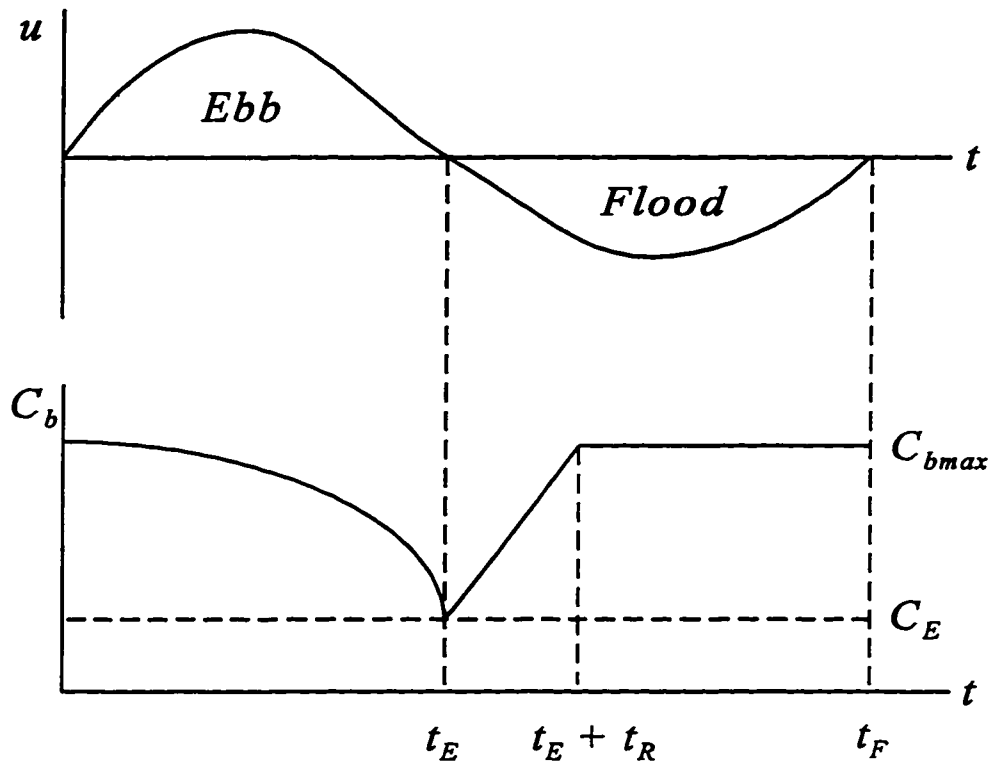


Fig. 22 Specification of salinity open boundary condition

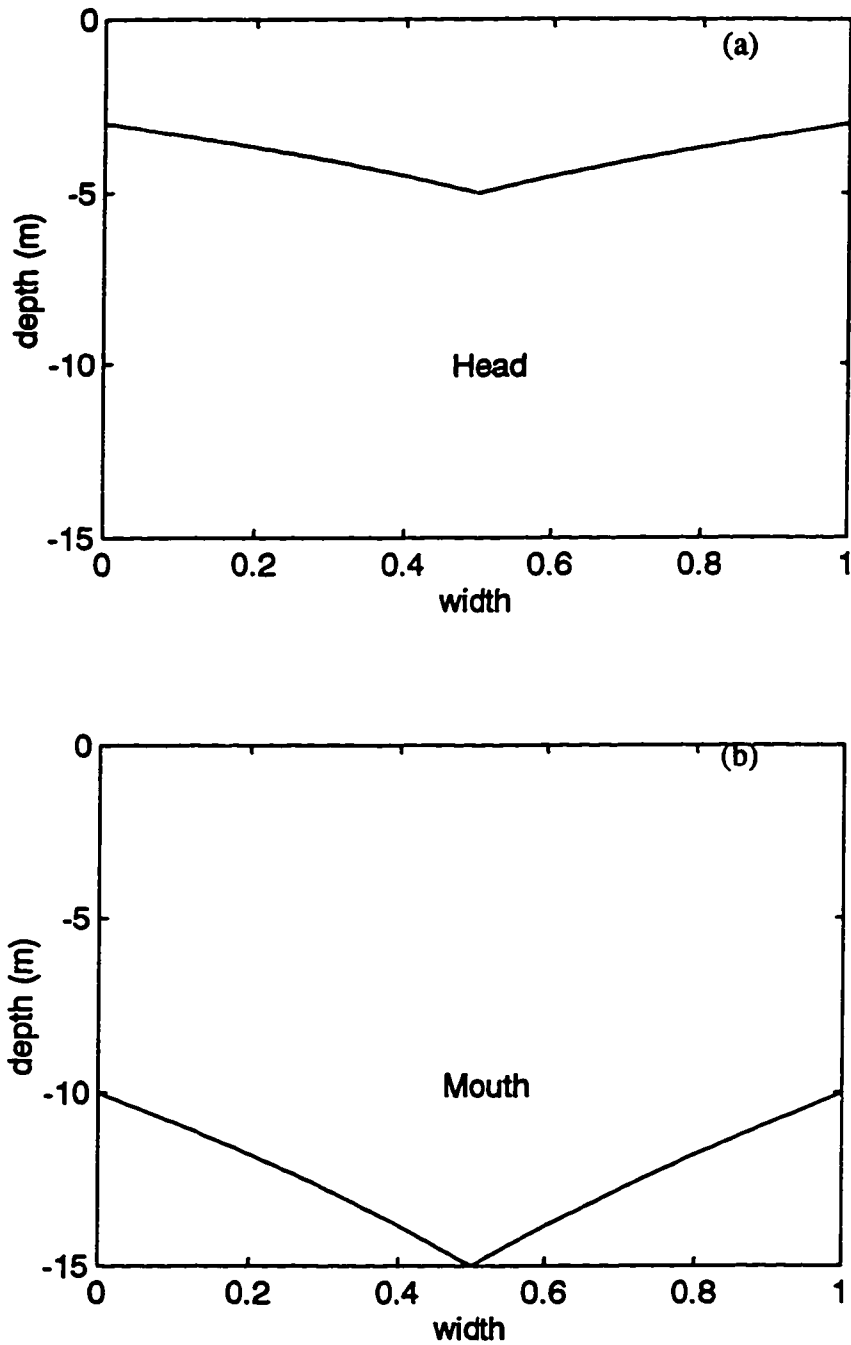


Fig. 23 Depth profiles at the head (a) and at the mouth (b).

The width is in relative scale.

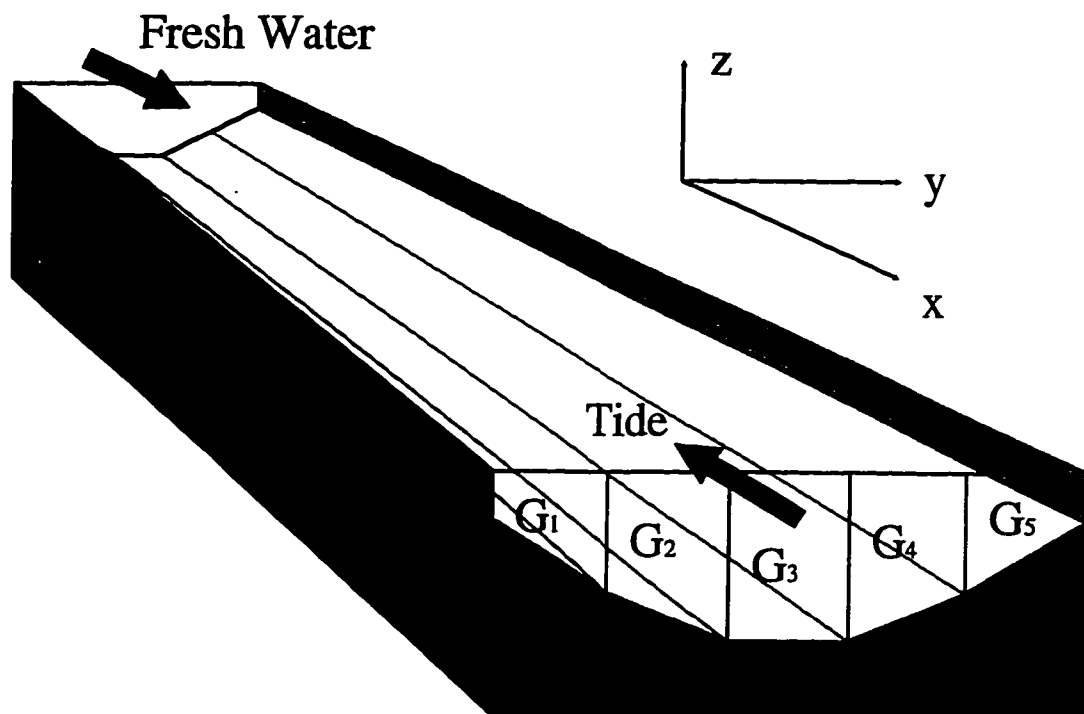
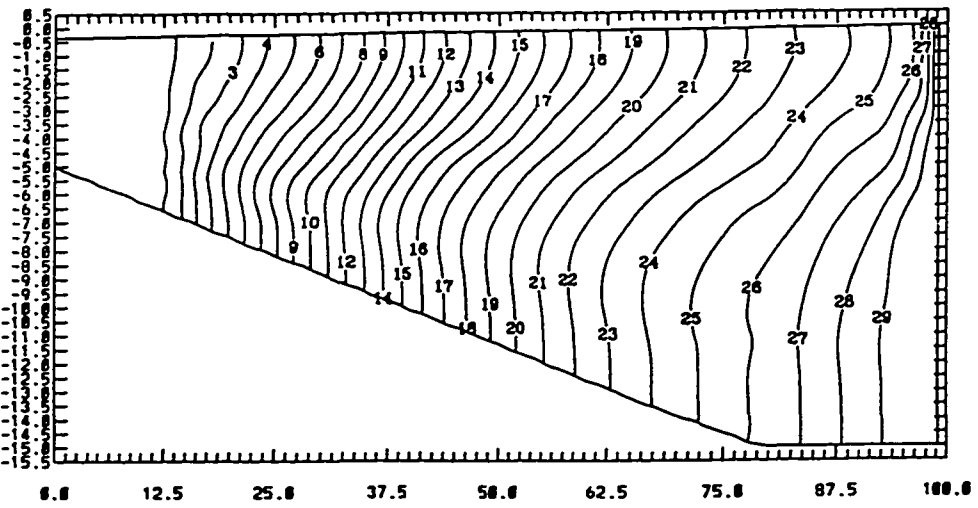
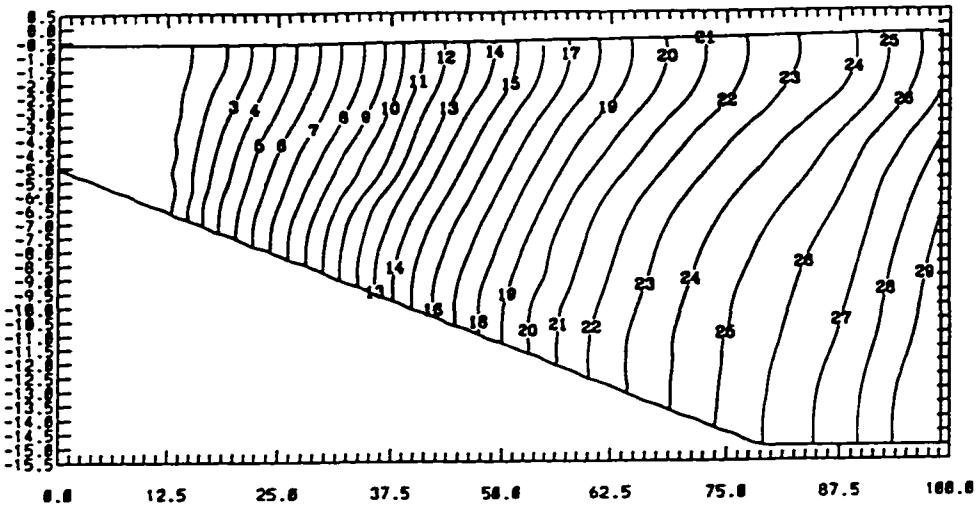


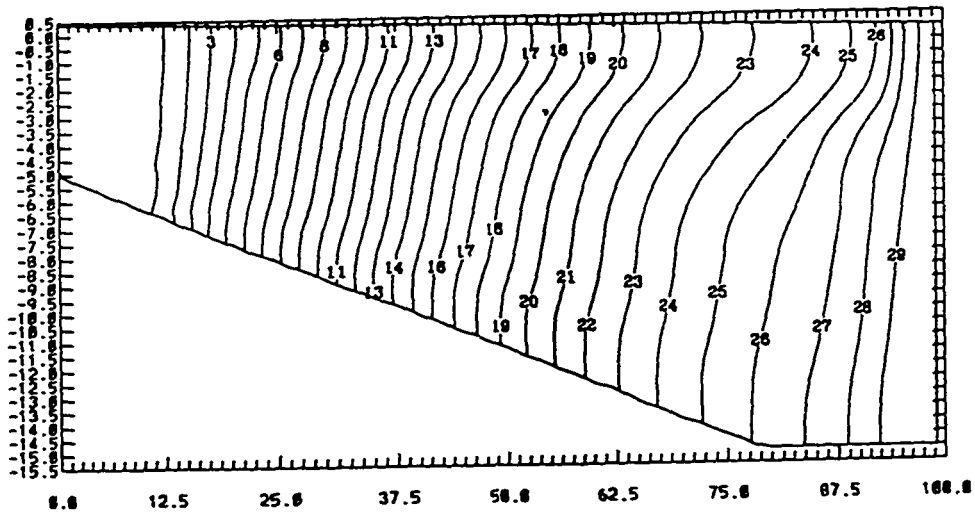
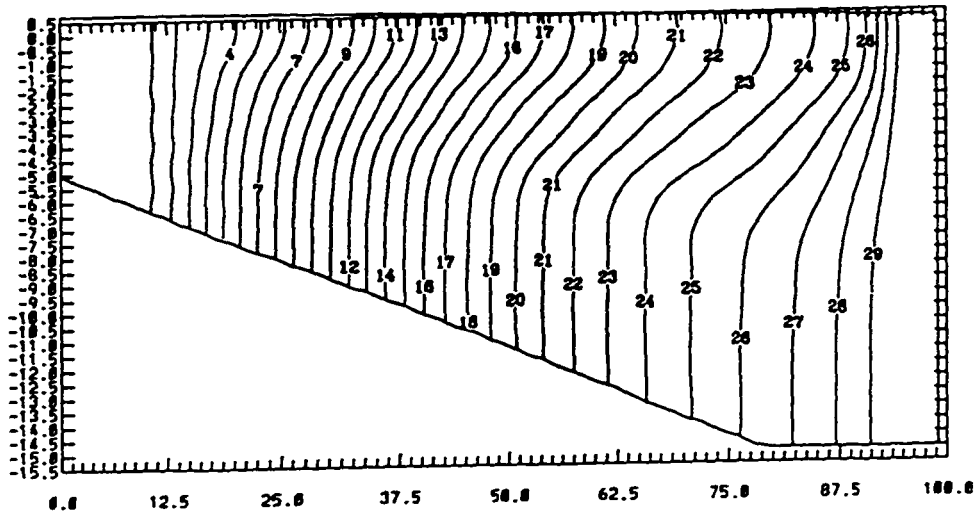
Fig. 24 Schematic of a 3-D idealized estuary



**Fig. 25 Horizontal physical grid of the 3-D idealized estuary**

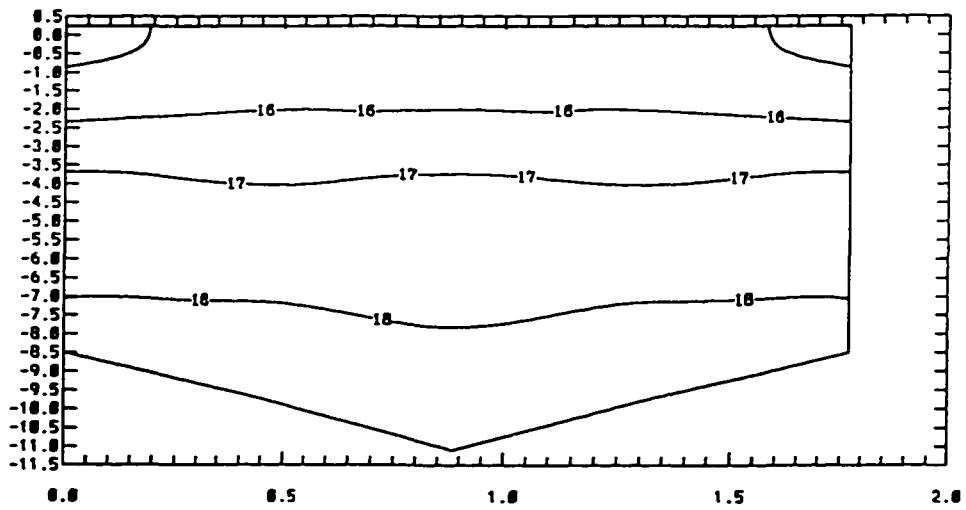
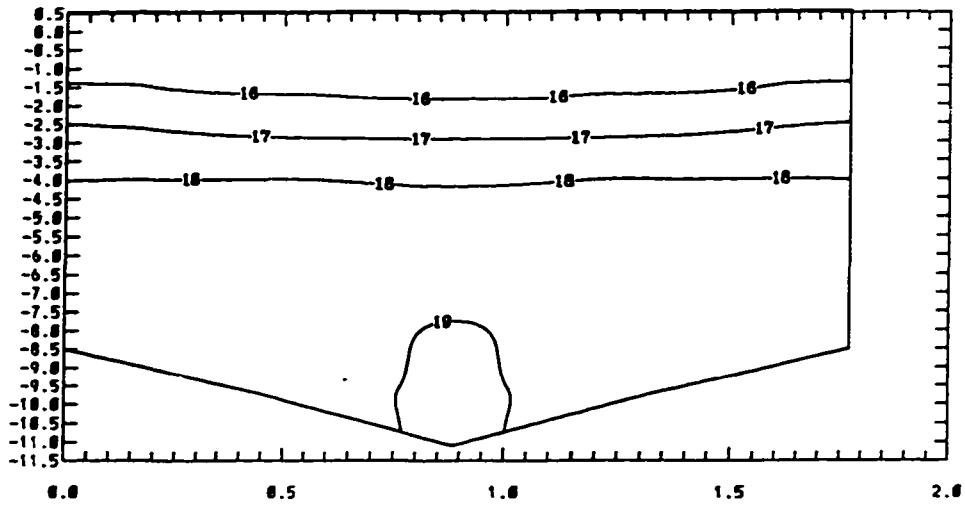
**Fig. 26 “Observed” salinity distribution (ppt) at four tidal phases ( $T/4$ ,  $T/2$ ,  $3T/4$  and  $T$ ) along the axis of the estuary channel**

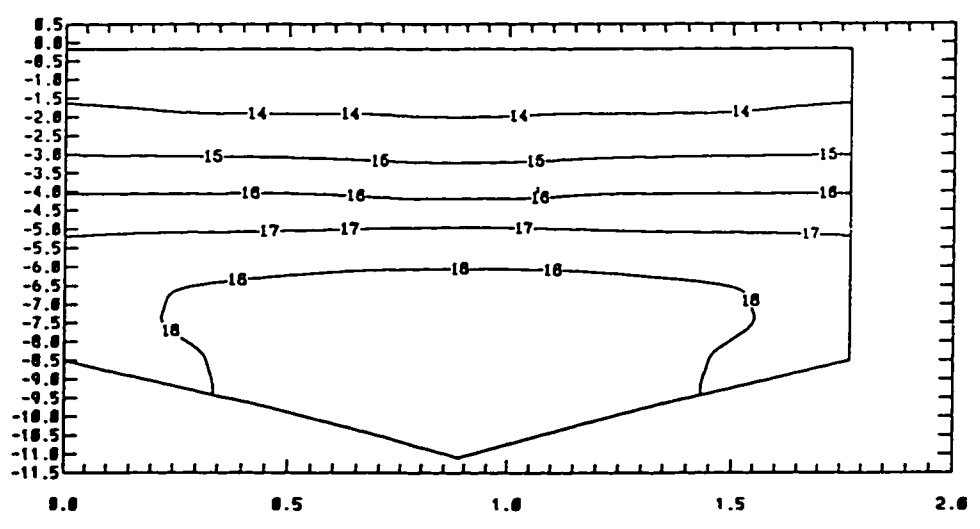
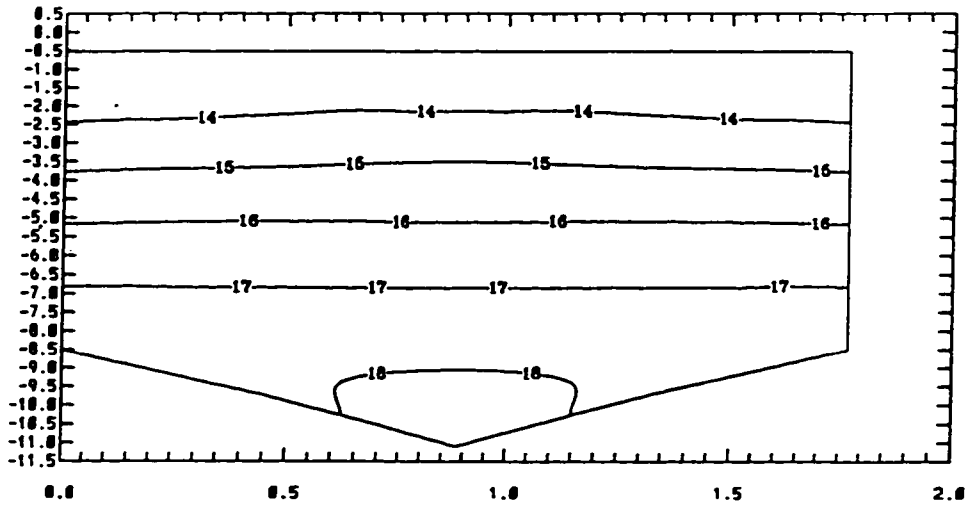






**Fig. 27 “Observed” salinity distribution (ppt) at four tidal phases ( $T/4$ ,  $T/2$ ,  $3T/4$  and  $T$ ) at the cross section I=50**





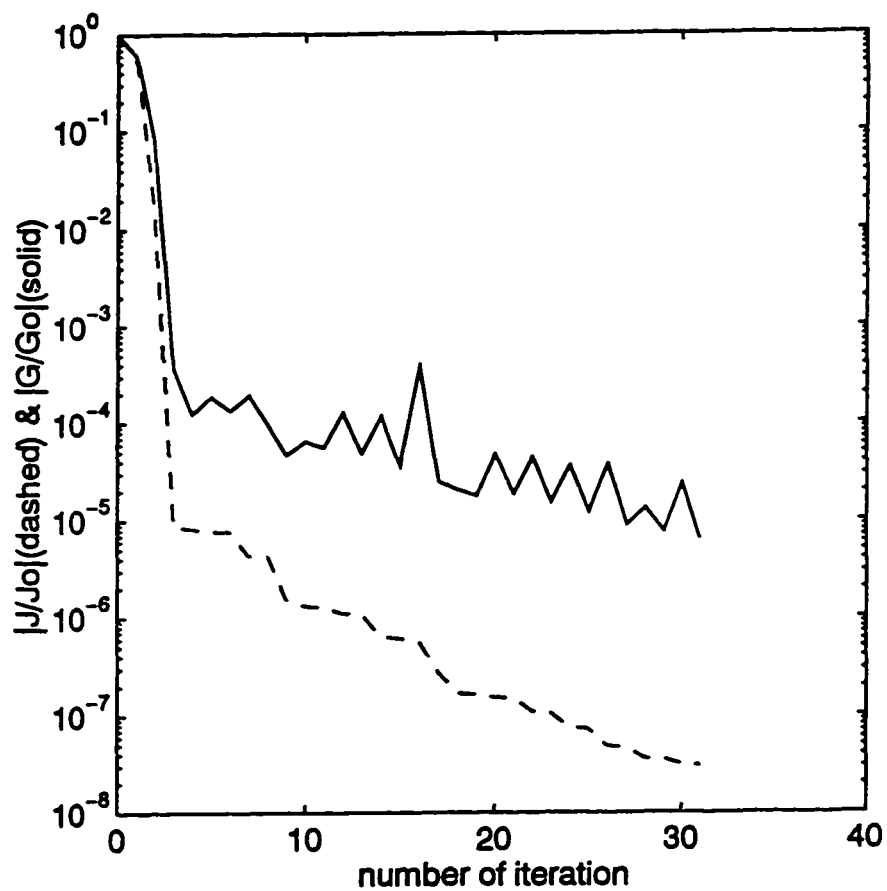


Fig. 28 Variations of  $|J_n/J_0|$  and  $|\nabla J_n/\nabla J_0|$  without penalty (initial guess I)

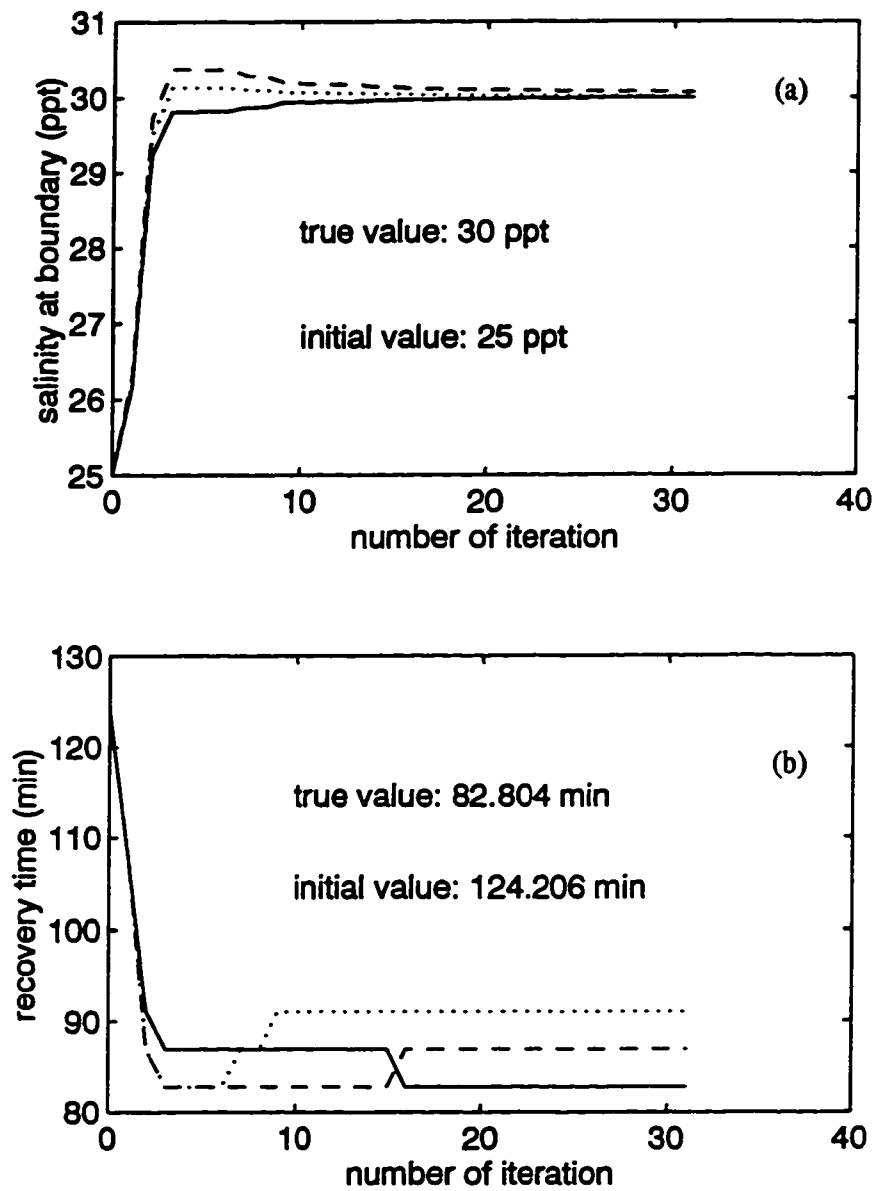


Fig. 29 Variations of the maximum salinity boundary value  $C_{bmax}$  (a) and the recovery time  $t_R$  (b) without penalty (initial guess I) at grid cell  $G_1$  (dashed),  $G_2$  (dotted) and  $G_3$  (solid)

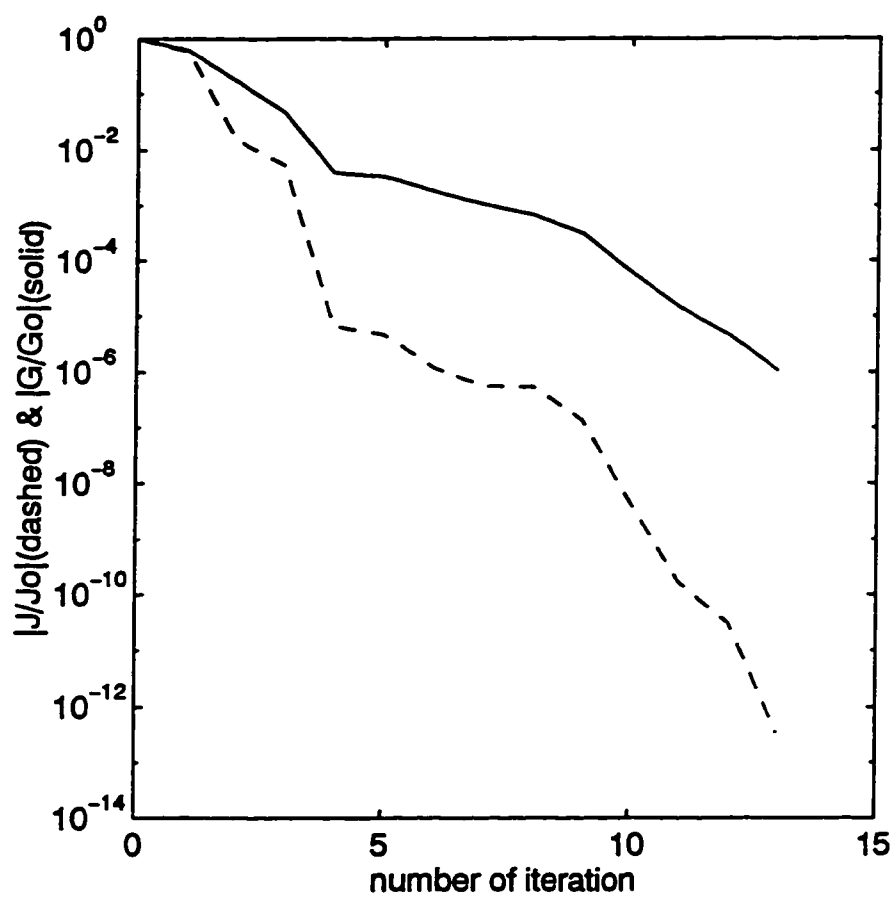


Fig. 30 Variations of  $\|J_n/J_0\|$  and  $\|\nabla J_n/\nabla J_0\|$  with penalty (initial guess I)

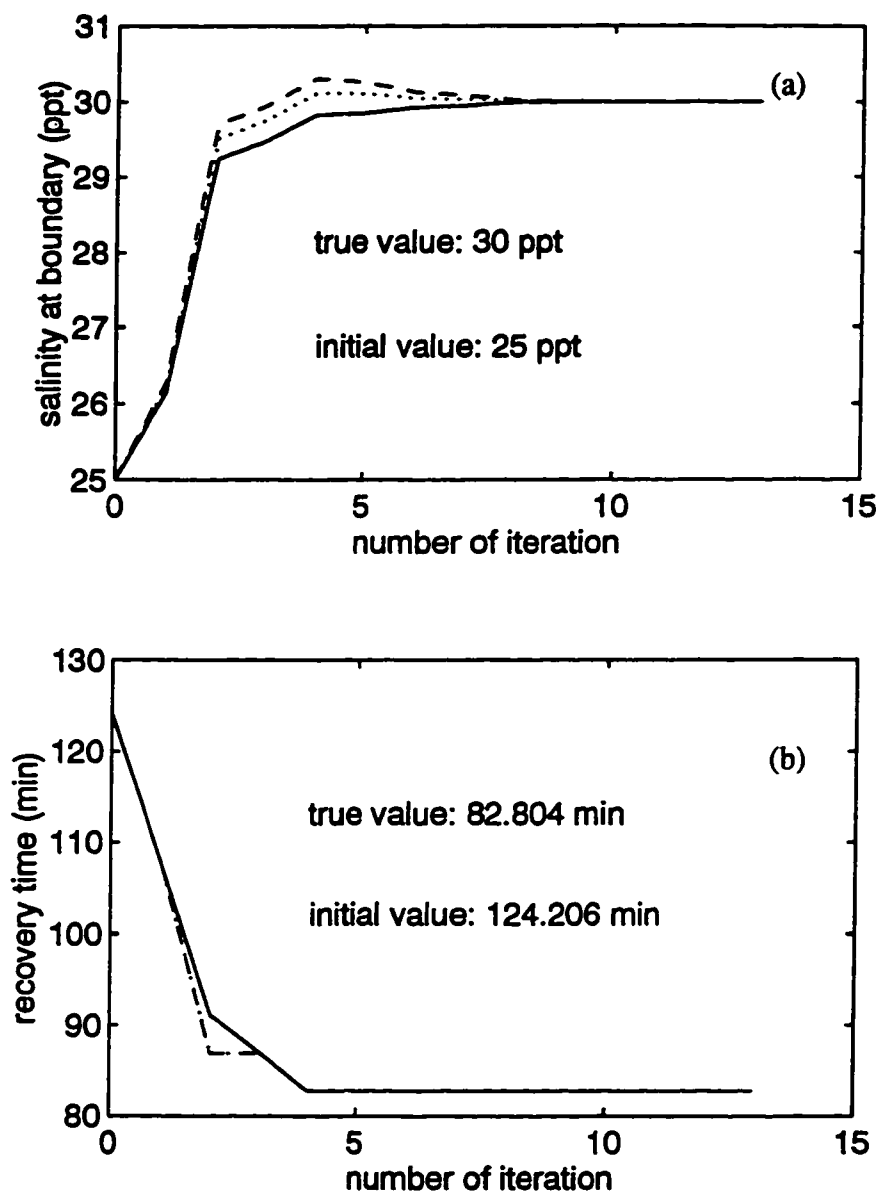


Fig. 31 Variations of the maximum salinity boundary value  $C_{bmax}$  (a) and the recovery time  $t_R$  (b) with penalty (initial guess I) at grid cell  $G_1$  (dashed),  $G_2$  (dotted) and  $G_3$  (solid)

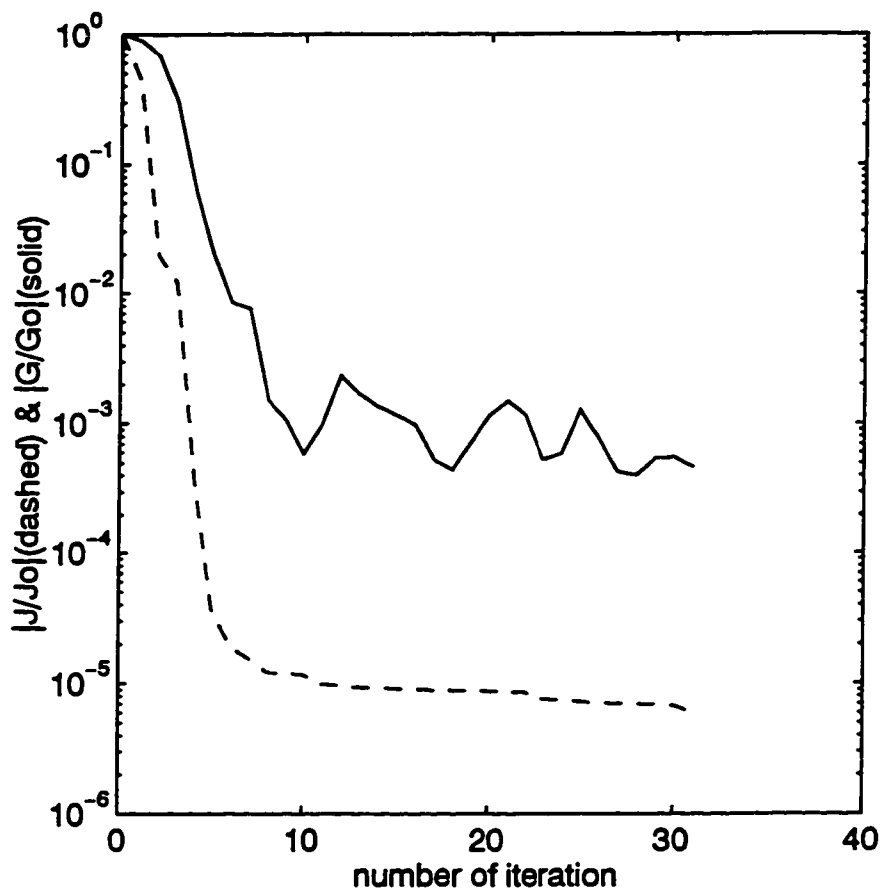


Fig. 32 Variations of  $|J/J_0|$  and  $\|\nabla J/\nabla J_0\|$  without penalty (initial guess II)



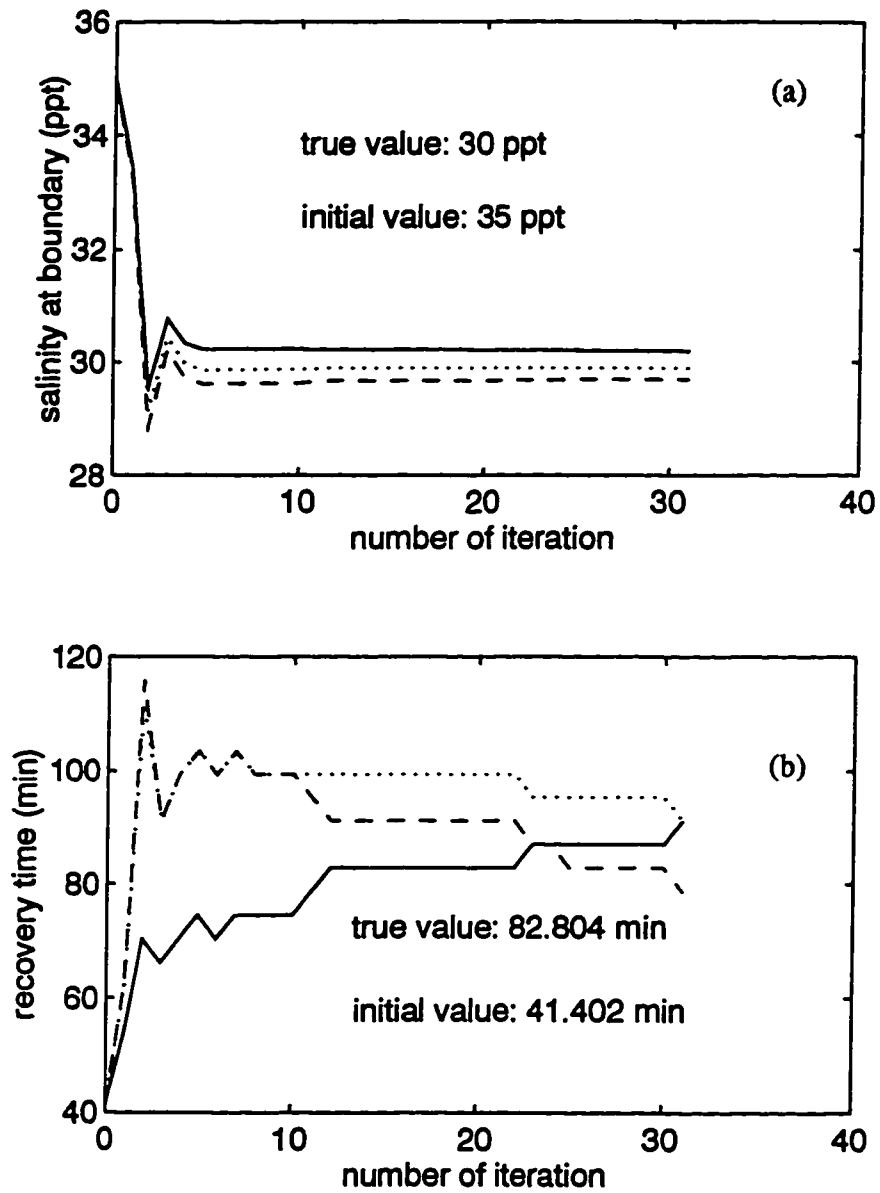


Fig. 33 Variations of the maximum salinity boundary value  $C_{bmax}$  (a) and the recovery time  $t_r$  (b) without penalty (initial guess II) at grid cell  $G_1$  (dashed),  $G_2$  (dotted) and  $G_3$  (solid)

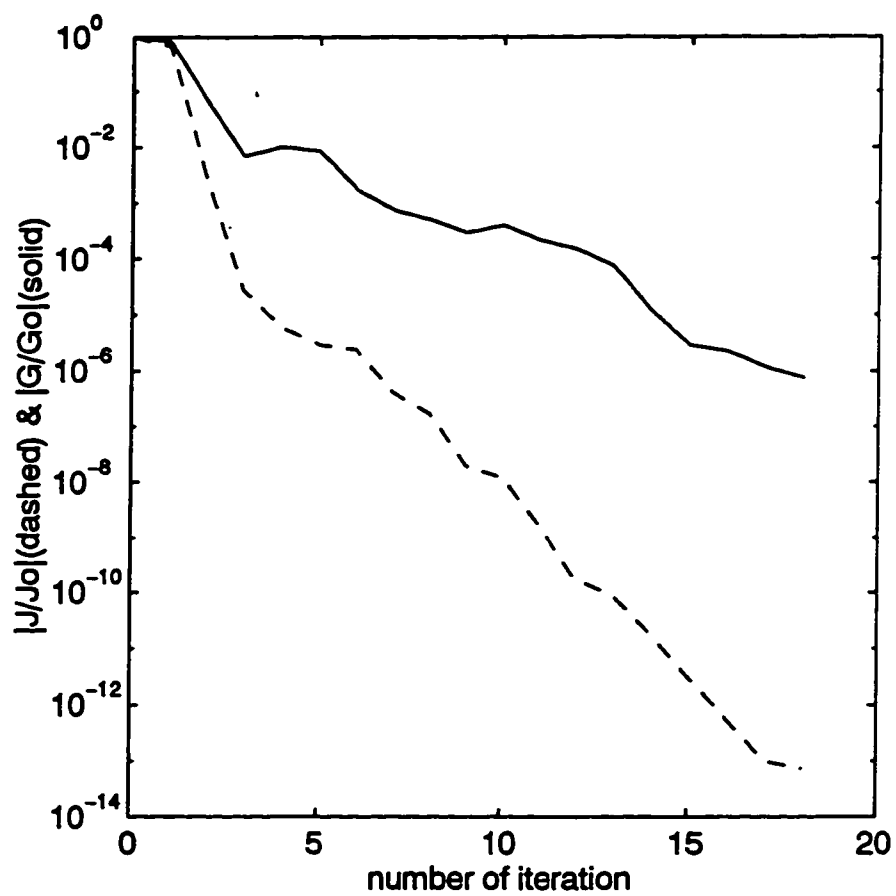


Fig. 34 Variations of  $|J_n/J_0|$  and  $|\nabla J_n/\nabla J_0|$  with penalty (initial guess II)

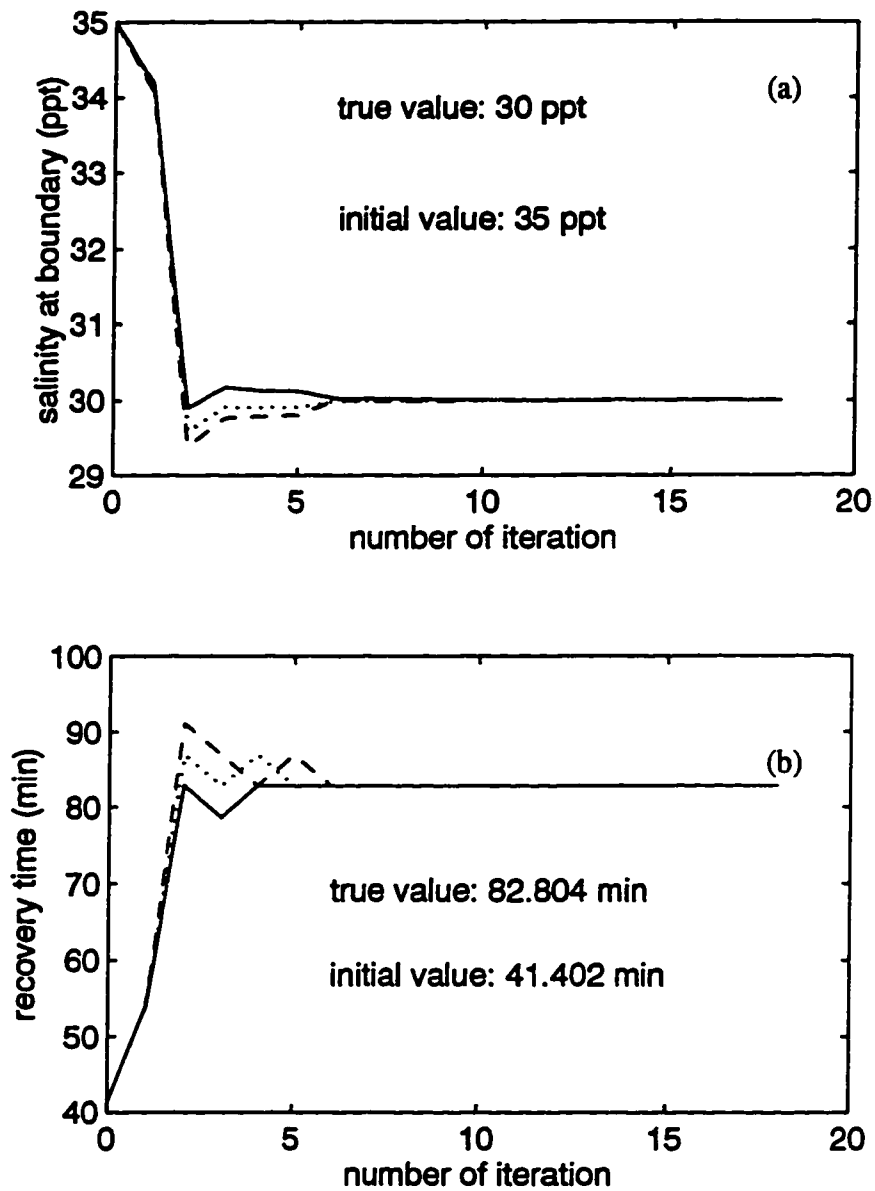


Fig. 35. Variations of the maximum salinity boundary value  $C_{bmax}$  (a) and the recovery time  $t_R$  (b) with penalty (initial guess II) at grid cell  $G_1$  (dashed),  $G_2$  (dotted) and  $G_3$  (solid)

## **5. PARAMETER ESTIMATION IN A COHESIVE SEDIMENT TRANSPORT MODEL**

### **5.1 Introduction**

Suspended sediment transport is one of the most important processes in estuarine and coastal waters. Suspended sediment is discharged into estuarine and coastal waters by river runoff or resuspended to the water column from the bed. Particles greater than about 60  $\mu\text{m}$  in diameter are considered to be coarse grained sediment, and less than 60  $\mu\text{m}$  are referred as fine grained sediment. Particles with grain size less than 2  $\mu\text{m}$  are mainly composed of clay minerals. Sediment becomes cohesive when it contains more than 10 percent of clay by weight because clay minerals are platelike and have ionic charges on their surface which cause the particles to interact electronically and stick together. Flocculation happens when the cohesive sediment discharged from the river meets the saline water and the effective weight of the particles increases. Flocculation is normally related to suspended sediment concentration and shear stresses in the water column. Fine grained sediment moves into the water column as a suspended load. The transport process of cohesive sediment are affected by many dynamic processes such as advection, diffusion, gravitational settling, deposition, erosion, flocculation and consolidation. The distribution pattern of suspended sediment is mainly controlled by the mean circulation pattern in estuaries.

For many years, scientists have been trying to understand the mechanisms of suspended sediment transport and forecast future sedimentation in estuarine environments

through field measurements, laboratory experiments, analytical studies and numerical models. For the purpose of sedimentation prediction, numerical modeling is by far the most useful tool since it can provide spatial and temporal distributions of suspended sediment concentration in the whole model domain. An early mathematical model of suspended sediment transport was developed by Odd and Owen (1972). They used a one-dimensional and two-layer model to simulate the cohesive sediment movement in the Thames Estuary. Following Odd and Owen's (1972) work, Ariathurai and Krone (1976) presented a horizontal two-dimensional finite element model for cohesive sediment transport and tested the model in a hypothetical harbor. Kuo *et al.* (1978) studied the sediment movement in the turbidity maximum of the Rappahannock River by a vertical two-dimensional model. Hayter and Mehta (1986) developed a two-dimensional, depth-averaged sediment transport model and verified the model against laboratory experiments performed in a recirculating flume. Satisfactory agreement between model prediction and laboratory measurement was obtained. The model was also applied to study the sedimentation in a harbor in Florida. Other early model studies of cohesive sediment transport were conducted by Owen (1977), Festa and Hansen (1978), Onish (1981) and Hayter (1983). Three-dimensional numerical modeling of sediment transport has developed rapidly in recent years. For example, a comprehensive sediment dispersion model which is coupled with a boundary layer model, an erosion model, a deposition model and a flocculation model was described by Sheng (1986). Nicholson and O'Connor (1986) developed a three-dimensional mathematical model simulating the transport of cohesive sediment and applied the model to a harbor siltation problem. The

effects of deposition, erosion, flocculation and consolidation are incorporated in their model. Cancino and Neves (1994) used a 3-D cohesive sediment transport model to simulate the suspended sediment distribution in a mesotidal estuary. Their model included the effects of flocculation, deposition and erosion processes. A series of model experiments were conducted to study the model sensitivity to important model parameters. For a recent review of the state of the art in sediment transport modeling, see van Rijn (1989).

Difficulties in measuring model parameters for deposition and erosion processes from both laboratory experiments and field observations still prevent numerical modeling of sediment transport from achieving a high level of predictive ability. In cohesive sediment transport modeling, there are four critical parameters strongly affecting numerical model results: 1) sediment settling velocity  $w_s$ ; 2) resuspension rate  $M_o$ ; 3) critical shear stress for deposition  $\tau_{cd}$  and 4) critical shear stress  $\tau_{cr}$  for erosion. Numerous studies have been dedicated to determining these parameters. Early studies of transport and shoaling processes under estuarine conditions was conducted by Krone (1962) through flume studies. He found that suspended sediment can be deposited only at bottom shear stresses less than a critical value of  $0.8 \text{ dyne/cm}^2$  and the deposition rate is very sensitive to the flocculation rate which is enhanced by the suspended sediment concentration. Owen (1970) studied the variation of  $w_s$  using natural mud in saline water. His results indicated that as salinity and suspension concentration increase, the settling velocity  $w_s$  also increases due to the increased cohesion and interparticle collision. Hayter (1983) investigated the effect of salinity on deposition and erosion using laboratory

experiments. Results showed that the influence of salinity on  $w_s$  is significant in the range of 0-2 ppt and as salinity increases  $w_s$  approaches a constant. The critical shear stress for erosion could be described as a linear function of salinity when salinity is in the range of 0-2 ppt and a constant when salinity is greater than 2 ppt.

According to literature,  $w_s$  and  $M_o$  can vary over the ranges of  $10^{-5}$  to  $10^{-1}$  (cm/s) and  $10^{-7}$  to  $10^{-3}$  (g/cm<sup>2</sup>/s) respectively, while the critical stresses  $\tau_{cd}$  and  $\tau_{cr}$  are in the ranges of 0.06 to 2 and 0.1 to 5 (dyne/cm<sup>2</sup>) respectively (Krone, 1962; Greenberg and Amos, 1983; DeVries, 1985; Gibbs, 1985; Sternberg *et al.*, 1988; Mehta *et al.*, 1989; Sheng *et al.*, 1992; Sanford and Halka, 1993). Some comparisons of these four parameters used in previous studies are listed in Table 8. We can see that these parameters vary over very wide ranges in different studies. Therefore, it is highly desirable to find a better way to retrieve these poorly known parameters based on field observations so that the optimal model state is found and so the best-fit of model results to the observation is produced. To date we have not seen any application of variational inverse methods in sediment transport problems. In this Chapter, a data assimilation scheme for estimation of the settling velocity and erosion or resuspension rate is described and tested in an idealized estuary and the James River, a tributary at the lower Chesapeake Bay.

## 5.2 Sediment Transport Models

The most typical governing equation for sediment transport is the advection and diffusion equation with a settling velocity of  $w_s$  :

$$\begin{aligned} \partial_t(mHC) + \partial_x(m_y HUC) + \partial_y(m_x HVC) + \partial_z(mwC) \\ = \partial_z(mH^{-1}D_v \partial_z C) + \partial_z(mw_s C) \end{aligned} \quad (67)$$

Many different models for sediment transport have been developed and they can be classified into three categories: 1) cohesive sediment models; 2) non-cohesive sediment models and 3) intermediate sediment models (Sanford and Halka, 1993). The differences between these models appear to be the approach to formulating the bottom boundary condition and different formulations for the deposition and erosion terms. In cohesive sediment models, a mutually exclusive deposition and erosion assumption is made and the flux bottom boundary condition for the cohesive model can be written as:

$$-w_s C - D_v \frac{\partial C}{\partial z} = E - D ; \quad z = -h \quad (68)$$

where  $D$  and  $E$  are the deposition rate and the erosion rate. The deposition rate is commonly described by the formula presented by Krone (1962):

$$D = \begin{cases} w_s C_1 \left(1 - \frac{\tau_b}{\tau_{cd}}\right) & \tau_b < \tau_{cd} \\ 0 & \tau_b \geq \tau_{cd} \end{cases} \quad (69)$$

where  $C_1$  is the sediment concentration near the bottom,  $\tau_b$  is the bottom shear stress and  $\tau_{cd}$  is the critical shear stress for deposition. As described in Section 5.1, the settling velocity is a function of salinity and suspended sediment concentration (Owen, 1970; Hayter, 1983; Dyer, 1986). In low sediment concentration,  $w_s$  can be considered as a constant but it changes significantly in high concentration. The transition zone is around 0.3 g/l (Krone, 1962). At any particular salinity, the settling velocity can be represented



as an exponential function of sediment concentration:

$$w_s = w_o \left( \frac{C}{C_o} \right)^{\gamma_o} \quad (70)$$

where  $C_o$  is the normalized sediment concentration, and  $\gamma_o$  is an empirical constant in the range of 1~3 (Dyer, 1986, van Leussen and Cornelisse, 1993). The reference settling velocity,  $w_o$  corresponds to  $C=C_o$ . In the present study, the effects of salinity and sediment concentration on the settling velocity are not considered, so  $\gamma$  is set to be zero and thus  $w_s=w_o$ . The erosion rate can be described as (Partheniades, 1962; Ariathurai and Arulanandan, 1978; Mehta, 1981; Sheng and Lick, 1979, Lee, 1995):

$$E = \begin{cases} M_o \left( \frac{\tau_b}{\tau_{cr}} - 1 \right)^\eta & \tau_b \geq \tau_{cr} \\ 0 & \tau_b < \tau_{cr} \end{cases} \quad (71)$$

in which the critical shear stress  $\tau_{cr}$  for erosion is assumed to be depth independent;  $\eta$  is an empirical constant;  $M_o$  is the erosion constant which is equivalent to the erosion rate when  $\tau_b=2\tau_{cr}$ . In many studies,  $\eta$  is assumed to be zero. In general,  $\tau_{cr}$  depends on salinity. Based on laboratory experiments, Hayter (1983) presented the following formula to describe the relationship between  $\tau_{cr}$  and salinity  $S$ :

$$\tau_{cr} = \begin{cases} \tau_{cr}^0 (0.5S+1) & 0 \leq S \leq 2 \\ 2 \tau_{cr}^0 & S \geq 2 \end{cases} \quad (72)$$

where  $\tau_{cr}^0$  is the critical shear stress when salinity equals zero ( $S=0$ ). From the above formula we know that  $\tau_{cr}$  is a constant for most salinity ranges but linearly increases when salinity is between 0~2 ppt. For the case where  $\tau_{cr}$  increases with depth of erosion,

the erosion rate can be described by (Sanford and Halka, 1993):

$$E = \begin{cases} \varepsilon_o \exp\{\alpha_1 [\tau_b - \tau_{cr}(z)]^{0.5}\} & \tau_b \geq \tau_{cr} \\ \varepsilon_o & \tau_b < \tau_{cr} \end{cases} \quad (73)$$

where  $\varepsilon_o$  and  $\alpha_1$  are empirical constants and  $z$  is the depth below the bottom surface. The most significant difference between the depth independent erosion model (Eq. (71)) and depth dependent erosion model (Eq. (73)) is that erosion always occurs in the depth dependent model while there is no erosion at all in the depth independent model when the bottom stress  $\tau_b$  is less than the critical stress  $\tau_{cr}$ .

In non-cohesive sediment models, erosion and deposition can occur simultaneously (Dyer, 1986; Glenn and Grant, 1987) and there is no critical shear stress for deposition, which is equivalent to an infinite critical shear stress. Sediments are transported as bedload in a layer with thickness  $a$ . The concentration bottom boundary condition at the top of this bedload layer is applied in non-cohesive transport models (Sanford and Halka, 1993; Glenn and Grant, 1987):

$$C_a = \begin{cases} \frac{C_o \gamma_o \left( \frac{\tau_b}{\tau_{cr}} - 1 \right)}{1 + \gamma_o \left( \frac{\tau_b}{\tau_{cr}} - 1 \right)} & \tau_b \geq \tau_{cr} \\ 0 & \tau_b < \tau_{cr} \end{cases} \quad (74)$$

where  $C_o$  is the sediment concentration in the bed and  $\gamma_o$  is an empirical constant on the order of  $10^{-3}$ - $10^{-5}$  (Sternberg *et al.*, 1988).

Some studies have been conducted for modelling sediment transport using the so-called intermediate approach. (Lavelle *et al.*, 1984, Bedford *et al.*, 1987, Sanford and

Halka, 1993). In the intermediate model, the flux bottom boundary condition (Eq. (68)) is applied but the non-cohesive transport assumption of simultaneous erosion and deposition is also made. That is, the critical shear stress for deposition is equal to infinity in Eq. (69) while the erosion rate (Eq. (71)) remains of the same form as that in cohesive sediment models.

In addition to bottom boundary condition, a no flux surface boundary condition is applied to all models:

$$-w_s C - D_v \frac{\partial C}{\partial z} = 0 ; \quad z = \zeta \quad (75)$$

In the present study, the cohesive sediment transport model is considered and the critical shear stress for erosion is assumed to be depth independent, i.e. Eqs. (67-69) and Eq. (71) will be used as bottom boundary conditions. A single class of sediment particles with a single set of deposition and erosion parameters is assumed. In principle, the VIMS EFDC model can be applied to multiple sediment classes with multiple deposition and erosion behaviors.

### 5.3 Adjoint Model And Gradient of The Cost Function

The derivation of the adjoint model and the gradients of the cost function for parameter estimation in sediment transport problems is very similar to that for the salinity open boundary condition problem. The cost function is still defined in the spatial and time domains as shown in Eq. (12). The Lagrange function  $L$  function is constructed by appending the sediment transport model equation (Eq. (67)) to the cost function:

$$L(C, \lambda, P) = J + \int_T \int_V \lambda \left\{ \begin{array}{l} \partial_t(mHC) + \partial_x(m_yHuC) + \partial_y(m_xHvC) \\ + \partial_z(mwC) - \partial_z(mH^{-1}D_v\partial_zC) - \partial_z(mw_sC) \end{array} \right\} dVdT \quad (76)$$

where  $P$  represents the control variables to be estimated ( $w_s$  and  $M_o$ ). Similarly, the adjoint model is represented by:

$$\begin{aligned} & -\partial_t(mH\lambda) - \partial_x(m_yHu\lambda) - \partial_y(m_xHv\lambda) - \partial_z(mw\lambda) \\ & -\partial_z(mH^{-1}D_v\partial_z\lambda) + \partial_z(mw_s\lambda) = W(C^{obs} - C) \end{aligned} \quad (77)$$

The gradients of the cost function can be obtained by setting  $\partial_p L=0$  ( $P=w_s, M_o$ ). Notice that when performing the spatial integral in Eq. (76), the bottom boundary condition Eq. (68) enters the integral. Neglecting all the terms not related to  $w_s$  and  $M_o$  allows one to obtain the general formula for the gradients of the cost function:

$$\partial_P J = \partial_P \int_T \int_V \lambda \partial_z(mw_s C) dVdT + \partial_P \int_T \int_\Omega \lambda (E-D) d\Omega dT \quad (78)$$

where  $\Omega$  represents the whole bottom boundary region. In the current study, both  $w_s$  and  $M_o$  are assumed constant in the whole spatial and time domain. Thus the gradient of the cost function with respect to  $w_s$  can be obtained by substituting Eq. (69) into Eq. (78):

$$\partial_{w_s} J = \int_T \int_V \lambda \partial_z(mC) dVdT - \int_T \int_\Omega \lambda C_1 \left(1 - \frac{\tau_b}{\tau_{cd}}\right) d\Omega dT ; \quad \tau_b < \tau_{cd} \quad (79)$$

and the gradient of the cost function with respect to  $M_o$  can be obtained by substituting Eq. (71) into Eq. (78):

$$\partial_{M_o} J = \int_T \int_\Omega \lambda \left(\frac{\tau_b}{\tau_{cr}} - 1\right) d\Omega dT ; \quad \tau_b > \tau_{cr} \quad (80)$$

Eq. (79) can be further written in a discrete form:

$$\begin{aligned} \partial_{w_s} J = & \sum_{n=1}^{NT} \sum_{k=1}^{K-1} \sum_{l=1}^{LN} 0.5 \times (\lambda_{l,k+1}^n + \lambda_{l,k}^n) [(mC)_{l,k+1}^n - (mC)_{l,k}^n] \\ & - \sum_{(\tau_b)_l^n < \tau_{cd}} \left[ \lambda C \left( 1 - \frac{\tau_b}{\tau_{cd}} \right) \right]_{l,1}^n \end{aligned} \quad (81)$$

where  $NT$  is the total number of time steps and  $LN$  is the total number of water cells.

Similarly, Eq. (80) can be written as:

$$\partial_{M_o} J = \sum_{(\tau_b)_l^n > \tau_{cr}} \left[ \lambda \left( \frac{\tau_b}{\tau_{cr}} - 1 \right) \right]_{l,1}^n \quad (82)$$

Since there is no sediment source at the water surface, under a stable conditions the vertical gradient of sediment concentration is generally not greater than zero:  $\partial_z(mC) \leq 0$ . Thus, from Eq. (79) (or Eq. (81)) we can see the gradient of the cost function with respect to  $w_s$  has an opposite sign of Lagrange multiplier  $\lambda$ . Also, Eq. (80) (or Eq. (82)) indicates that the gradient of the cost function with respect to  $M_o$  has the same sign as  $\lambda$ . That means that if  $\lambda$  has the same sign in the whole domain then  $\partial J / \partial w_s$  would always have an opposite sign of  $\partial J / \partial M_o$ . This actually shows how  $w_s$  and  $M_o$  affect suspended sediment transport from different point of view, i.e., increasing resuspension rate  $M_o$  or decreasing settling velocity  $w_s$  will result in more suspended sediment in the water column, or vice versa.

One of the important issues in adjoint parameter estimation is the identifiability which addresses the question of whether it is possible to obtain unique solutions of the inverse problems (Navon, 1996). In reality, inverse problems are often ill-posed and are characterized by the nonuniqueness and the instability of the identified parameters of the problems. The ill-posedness of a problem causes difficulties to identify the spatially and

temporally dependent parameters in the inverse problem. It is shown that the regularization provides an efficient approach to solve the ill-posed inverse problems. Regularization is an approach to solve a well-posed regularized problem which has an approximated, but more regular, solution than that of the original problem. Recent work on the identifiability of an inverse problem can be seen in Navon (1996).

## 5.4 Model Tests in An Idealized 3-D Estuary

### 5.4.1 Forward Problem

The inverse model for the parameter estimation in the cohesive sediment transport problem is first tested in an idealized 3-D semi-enclosed estuary. The geometry is the same as that in the salinity open boundary problem (Fig. 24). The physical forcing and salinity boundary conditions are also the same. At the open boundary, zero sediment concentration is specified, *i.e.*, no sediment is transported into the estuary from the estuarine mouth. The suspended sediment source is specified at the head of the estuary with a constant discharge concentration 50 (mg/l) through the whole water column. The initial conditions for the suspended sediment is assumed to be 50 (mg/l) in the whole domain and the initial bed sediment per unit area is specified as 1000 (g/m<sup>2</sup>). The critical shear stresses for deposition and resuspension are set to be  $\tau_{cd}=0.25$  (dyne/cm<sup>2</sup>) and  $\tau_{cr}=0.5$  (dyne/cm<sup>2</sup>) respectively. The "observed" suspended sediment distribution is generated with a settling velocity  $w_s=5\times 10^{-5}$  (m/s) and a resuspension constant,  $M_o=0.4$  (g/m<sup>2</sup>/s). The hydrodynamic model and transport model for salinity and suspended sediment were run for 50  $M_2$  tidal cycles. The velocity field, vertical diffusivity and bed

shear stress in the last tidal cycle were saved to run the forward problem for sediment transport. The suspended sediment concentration at the end of the run is also saved and used as the initial condition for the forward problem. The forward simulation is made for 10 tidal cycles and the "observed" suspended sediment distributions along the channel of the estuary at 4 different phases of the last tidal cycle at the end of the run are presented in Fig. 36.

The turbidity maximum, one of the most distinguishing feature of estuaries is a zone within which the concentration of suspended sediment is higher than concentrations both upstream and downstream. The turbidity maximum is located around the limit of salt intrusion point and maintained by the mean longitudinal circulation in the estuary. Upstream of the turbidity maximum, sediment is transported to the turbidity maximum zone by the seaward mean flow and downstream sediment either settles to the bottom layer or is transported back to the turbidity maximum zone by the landward mean flow in the bottom layer due to the density-driven two-layer circulation. Because the salt intrusion and the pattern of the mean circulation are functions of the freshwater discharge, the location of the turbidity maximum is altered with changing river discharge. From Fig. 36 we can see that a suspended sediment turbidity maximum is formed upstream in the estuary at the location of the salinity intrusion limit (see Fig. 26). In the turbidity maximum zone, the suspended sediment concentration is on the order of 300 (mg/l), while downstream, the sediment concentration is lower than 10 (mg/l). The sediment distributions across a section of the turbidity maximum are presented in Fig. 37. From this figure we can see the sediment concentration at the shallow sides is higher than that

in the center of the deep channel. This is caused by the mean transverse circulation. Fig. 38a&b show the distribution patterns of the longitudinal and transverse Lagrangian mean velocity across the section of turbidity maximum zone, facing landward. A positive value implies that the current direction is seaward in Fig. 38a and to the right in Fig. 38b, while a negative value implies that the current direction is landward in Fig. 38a and to the left in Fig. 38b. Fig. 38a shows that the net landward flow is confined at the center of the channel and a net seaward flow occupies the surface and both shallow side regions. Fig. 38b indicates that a pair of "ring" type transverse circulation cells are formed in the cross section which causes divergence at the bottom layer and convergence at the surface layer. Such a transverse circulation pattern may be caused by the baroclinic forcing and bathymetry effect, which can be seen clearly in the mean salinity distribution in Fig. 39. Similar transverse circulation patterns were observed by Valle-Levinson and Lwiza (1995) in the lower Chesapeake Bay, by analysis of ADCP data and by numerical model study. A general description of mechanisms for the transverse circulation patterns can be found in Dyer (1979). The net divergence flow at the bottom layer thus transports the suspended sediment from the central axis to both shallow sides of the estuary.

#### **5.4.2 Inverse Problem**

The inverse model for the suspended sediment transport problem is tested by twin experiments. Observation data are sampled at 5 horizontal locations ( $I=10, 20, 30, 40, 50$ ), covering the region of turbidity maximum along the central axis of the estuary. There are 12 samples in each tidal cycle. The first test experiment is started with initial



guesses of  $w_s=5\times 10^{-4}$  (m/s) and  $M_o=0.04$  (g/m<sup>2</sup>/s). The suspended sediment distribution along the central axis of the estuary after 10  $M_2$  tidal cycles with the aforementioned initial guess values is plotted in Fig. 40. Because of increasing of settling velocity  $w_s$ , the suspended sediment discharged from the head of the estuary immediately settles down in the very upstream region of the estuary. Also because of decreasing the erosion constant  $M_o$ , the sediment being resuspended up to the water column from the bed is reduced. Thus the combined effect of increasing settling velocity  $w_s$  and decreasing erosion constant  $M_o$  is the decrease of the suspended sediment concentration in the water column.

Since the magnitudes of  $w_s$  and  $M_o$  are much less than unity, we scale  $w_s$  and  $M_o$  by factors of  $2\times 10^4$  and 30 respectively. The gradients of the cost function with respect to  $w_s$  and  $M_o$  are also scaled to the order of magnitude of unity by factors of  $2\times 10^4$  and 25 respectively. The minimization process is shown in Fig. 41. We can see that it only takes 11 iterations for both parameters to converge to the true solution. The good performance of the minimization may be due to recovering only two parameters and the use of sufficient data to construct the cost function such that the problem can be well-determined. The cost function and the gradient norm are reduced to the order of  $10^{-14}$  and  $10^{-8}$  respectively. The distributions of the settling velocity and erosion constant versus the number of iterations are plotted in Fig. 42a&b.

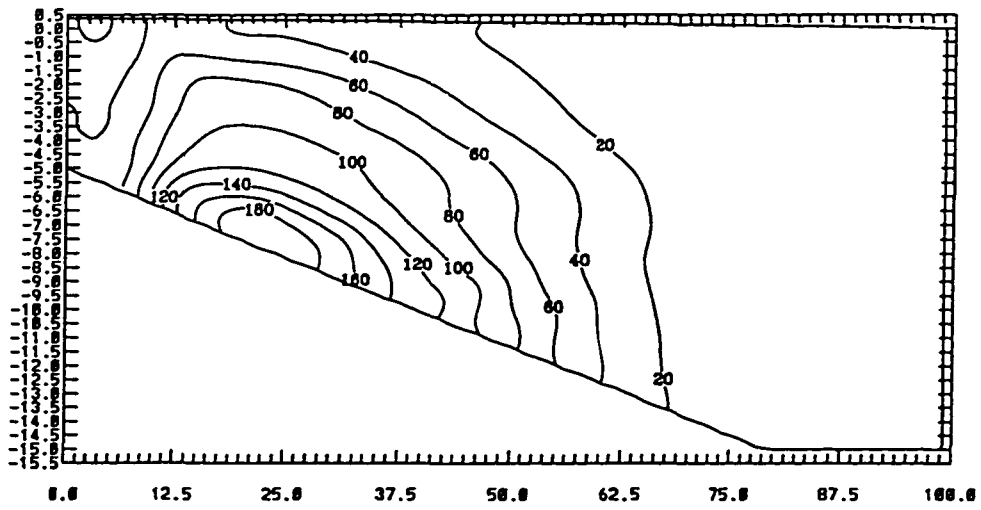
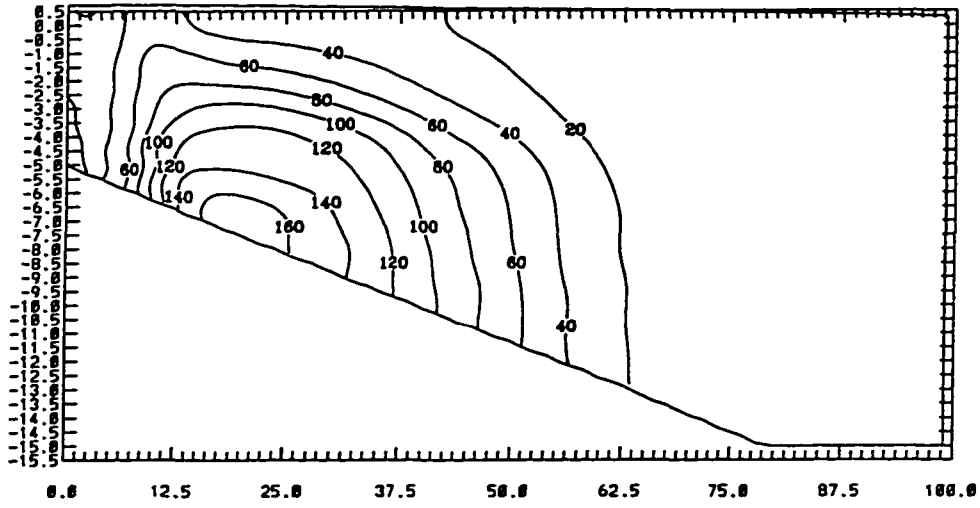
The inverse model is also tested with a different set of initial guesses: decreasing the settling velocity to  $w_s=5\times 10^{-6}$  (m/s) and increasing the erosion constant to  $M_o=4.0$  (g/m<sup>2</sup>/s). The suspended sediment distribution at four different tidal phases along the

estuary with such a set of initial guesses is plotted in Fig. 43. Now, because the settling velocity is decreased and the erosion constant is increased, much more sediment is suspended in the water column, even downstream portion of the estuary, compared to the "observed" suspended sediment distribution (Fig. 36). Actually, as the settling velocity approaches zero, the suspended sediment will become neutrally buoyant and the distribution will be more similar to that of salinity. The normalized cost function and the gradient norm versus the number of iterations are shown in Fig. 44. Again, we can see that the minimization process converges very fast and the cost function and the gradient norm are reduced to the order of  $10^{-19}$  and  $10^{-8}$  respectively. The convergence of the settling velocity and the erosion constant in terms of the number of iterations are plotted in Fig. 45a&b, respectively. Fig. 42a&b and Fig. 45a&b also show that in the two identical twin experiments described above, the settling velocity and the erosion constant converge to satisfactory estimates of the true solutions within 5 iterations, with the cost function reduced by the order of  $\sim 10^{-4}$ .

Table 8. Parameters for cohesive sediment transport used in literature

| References                     | $w_s$<br>(cm/s) | $M_o$<br>(g/cm <sup>2</sup> /s) | $\tau_{cd}$<br>(dyne/cm <sup>2</sup> ) | $\tau_{cr}$<br>(dyne/cm <sup>2</sup> ) |
|--------------------------------|-----------------|---------------------------------|--|--|
| Sternberg <i>et al.</i> (1988) | 0.28            |                                 | 0.49                                   |  |
| Gibbs (1985)                   | 0.01-0.1        |                                 |  |  |
| DeVries (1992)                 |                 | $6.25 \times 10^{-7}$           |  | 1.44                                   |
| Lee (1995)                     |                 | $10^{-5}$ - $10^{-4}$           |  | ~1.0                                   |
| Greenberg & Amos (1983)        | 0.11            | $1.9 \times 10^{-3}$            | 0.84                                   | 2.56                                   |
| Krone (1962)                   |                 |                                 | 0.8                                    |  |
| Sanford & Halka (1993)         | 0.08-0.14       | $1.2 \times 10^{-6}$            | 0.25-0.4                               | 0.4                                    |
| Sheng (1990)                   | 0.012           | $5.31 \times 10^{-8}$           |  | 6.4                                    |

**Fig. 36 “Observed” suspended sediment distribution (mg/l) at four tidal phases  
(T/4, T/2, 3T/4 and T) along the axis of the estuary channel**



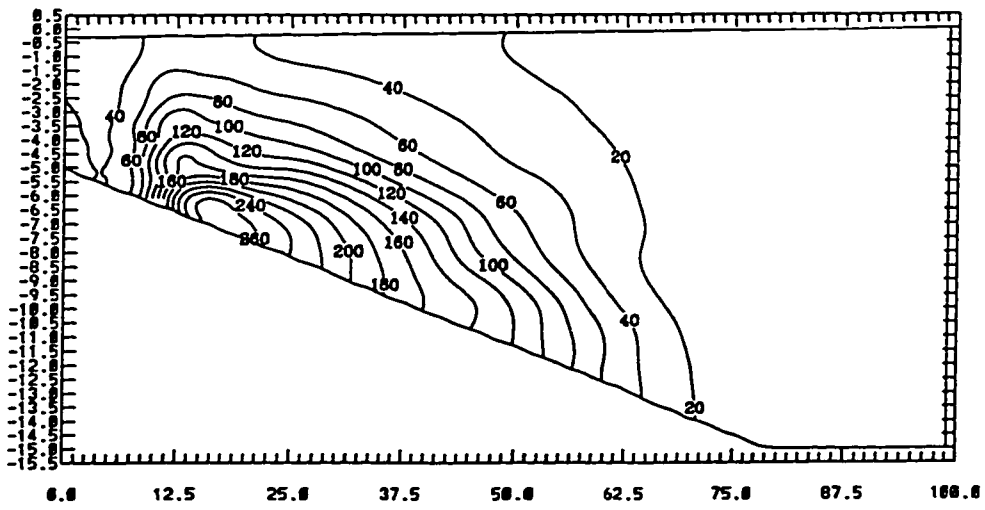
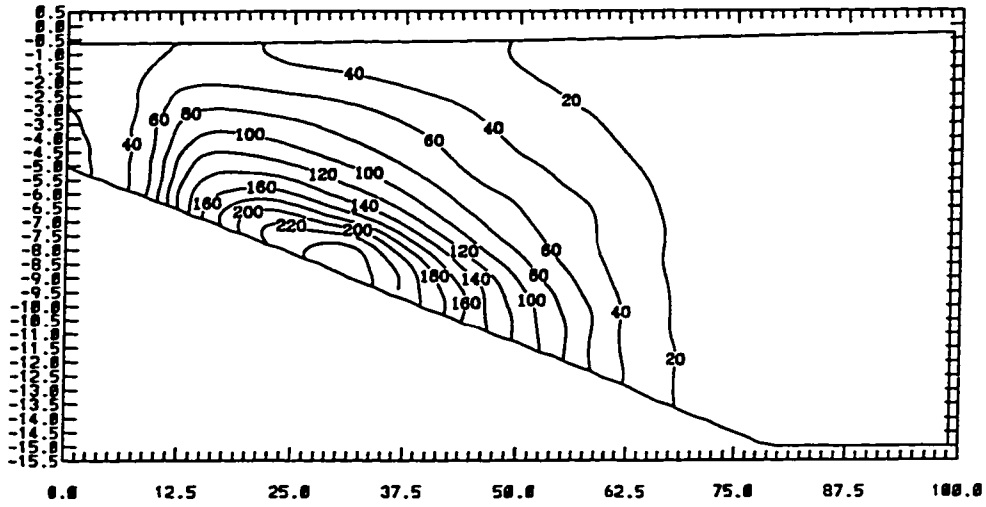
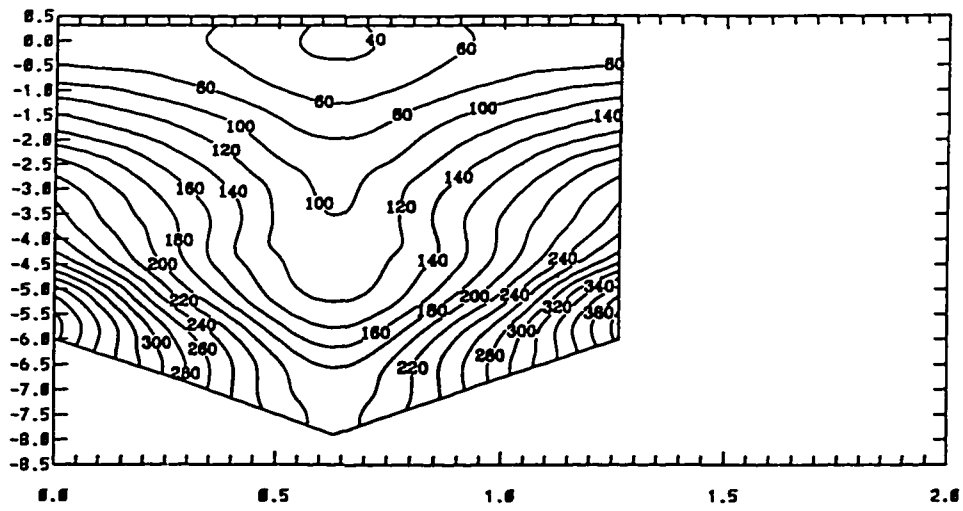
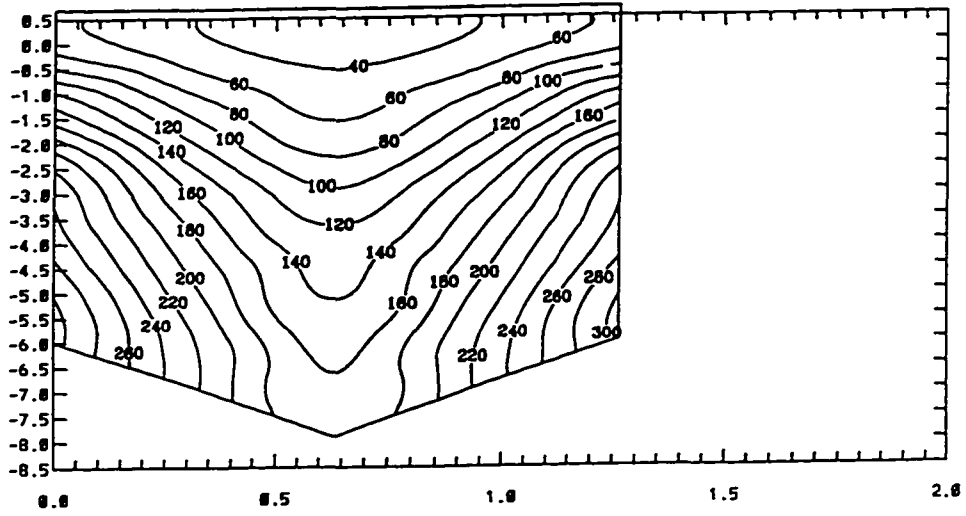
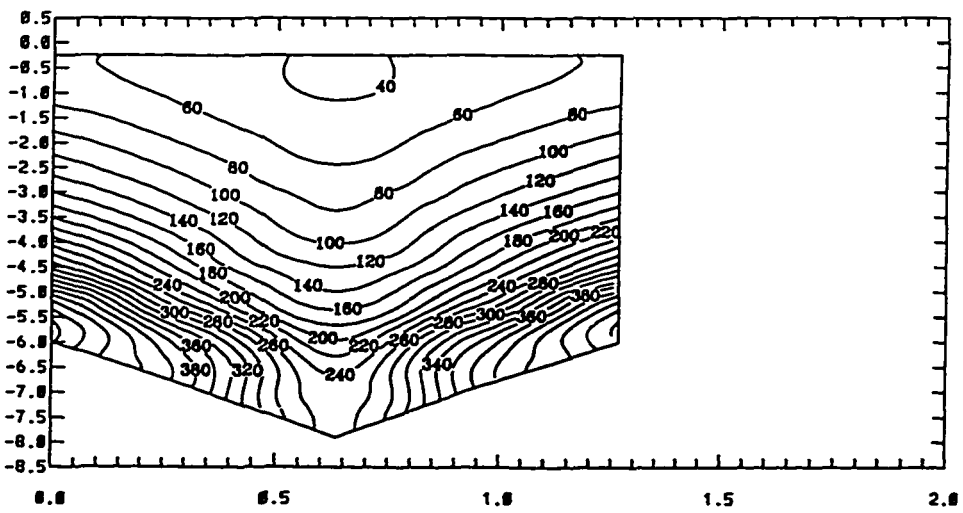
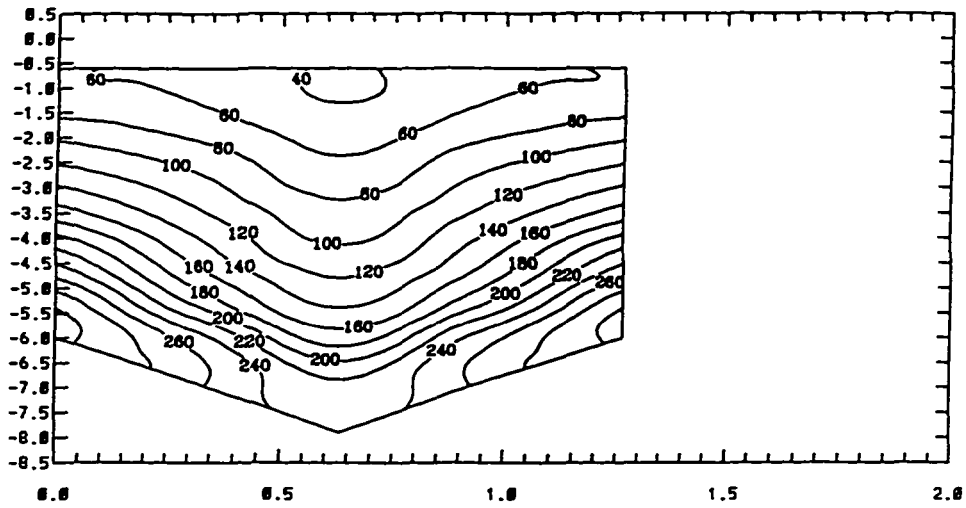


Fig. 37 "Observed" suspended sediment distribution (mg/l) at four tidal phases  
(T/4, T/2, 3T/4 and T) at the cross section I=25







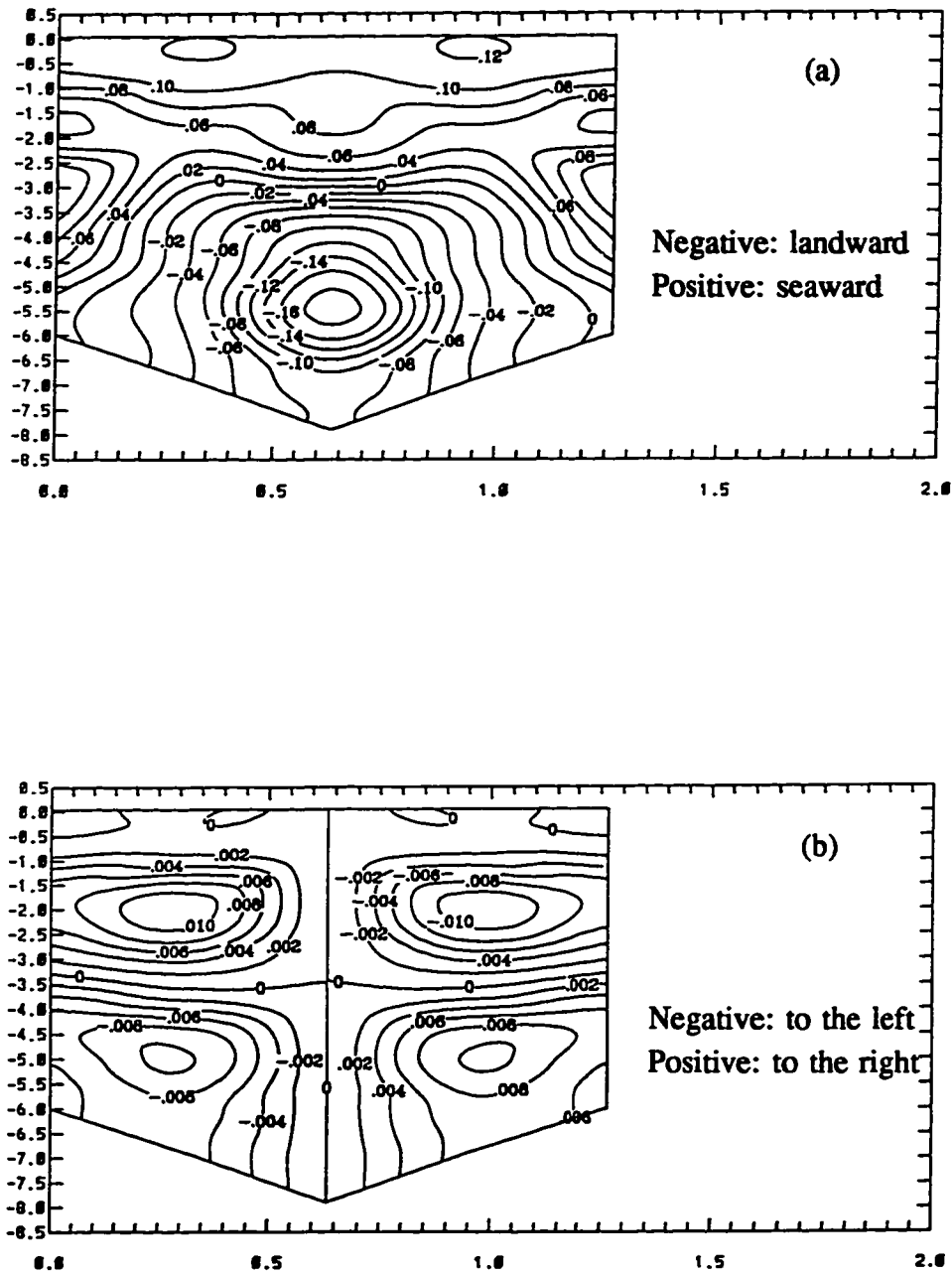


Fig. 38 Lagrangian mean velocity (m/s) at the cross section I=25:

longitudinal component (a) and transverse component (b)

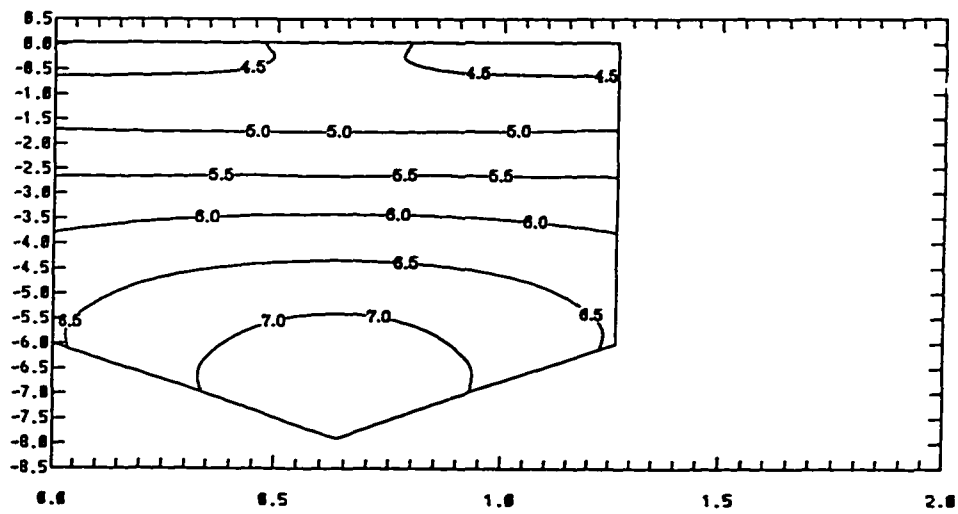
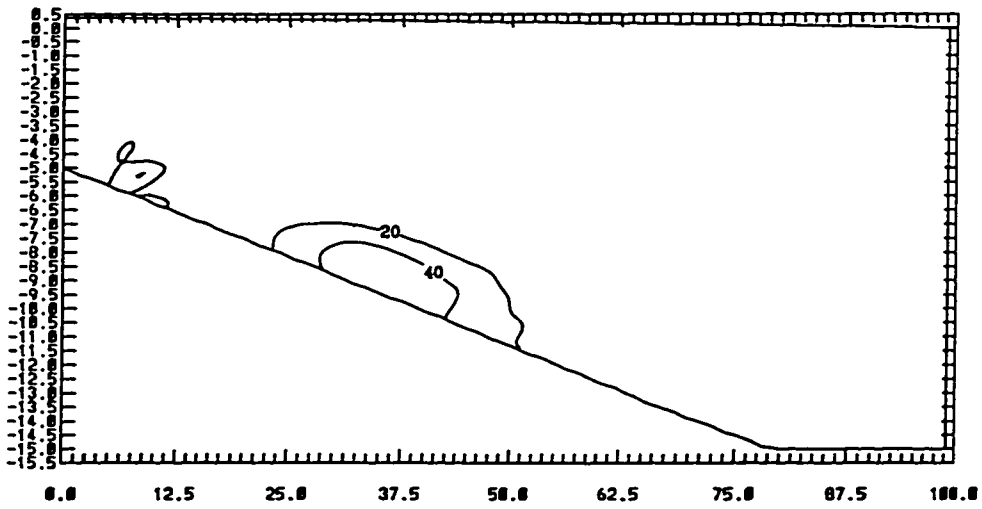
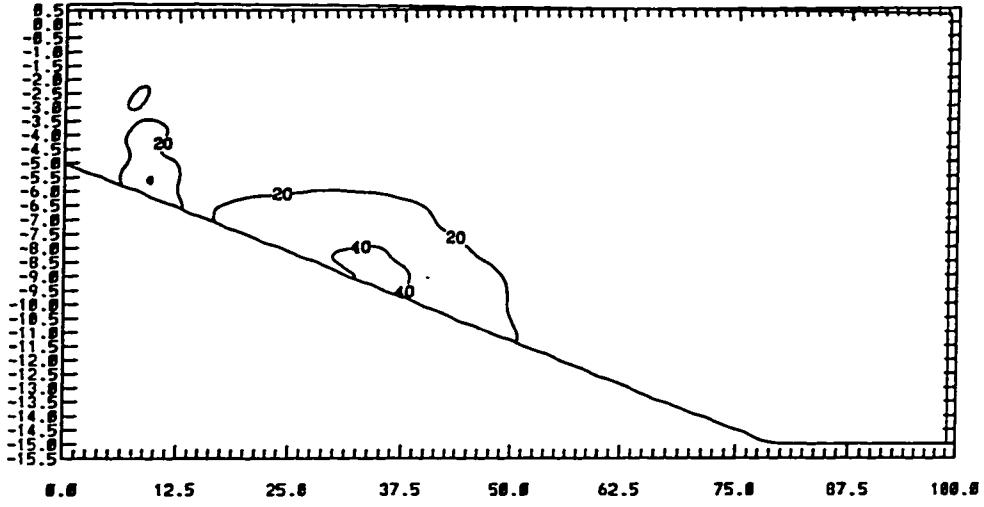
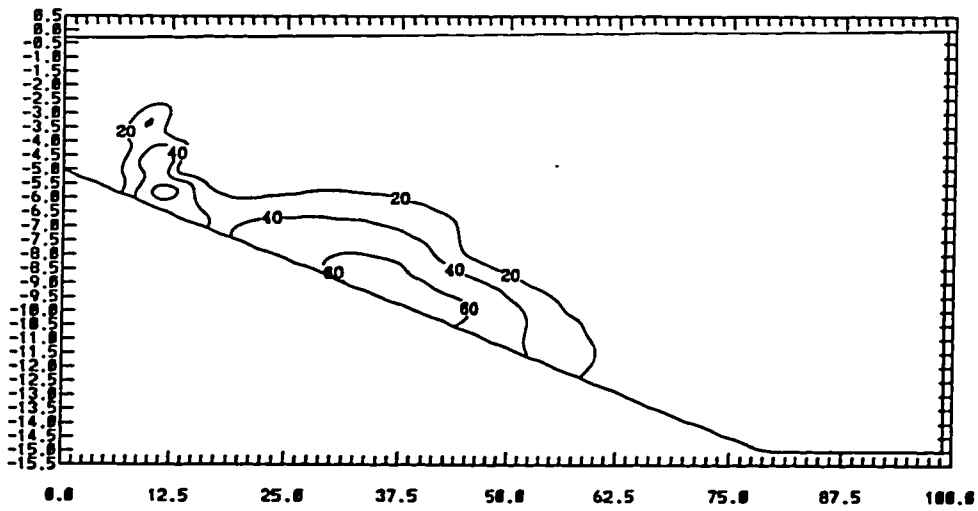
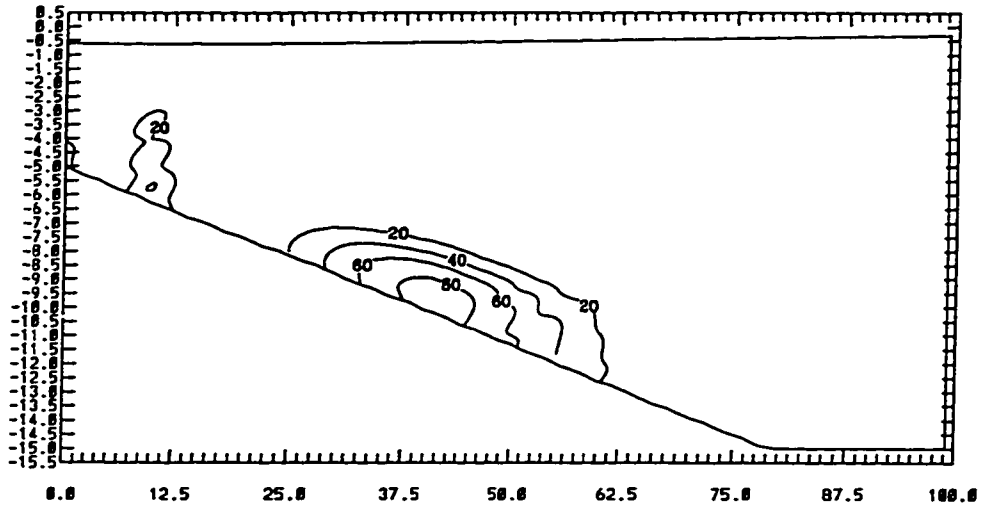


Fig. 39 Mean salinity distribution (ppt) at the cross section I=25

**Fig. 40 Initial suspended sediment distribution (mg/l) at four tidal phases (T/4, T/2, 3T/4 and T) along the axis of the estuary channel (initial guess I)**





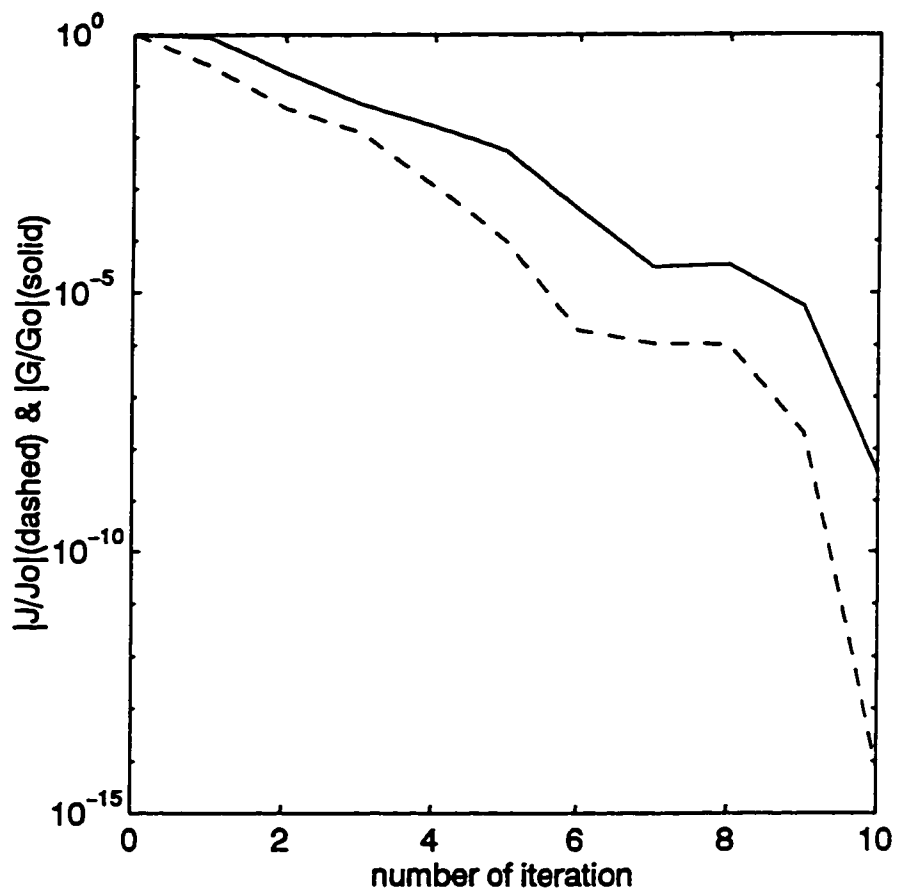


Fig. 41 Variations of  $|J/J_0|$  and  $|G/G_0|$  (initial guess I)

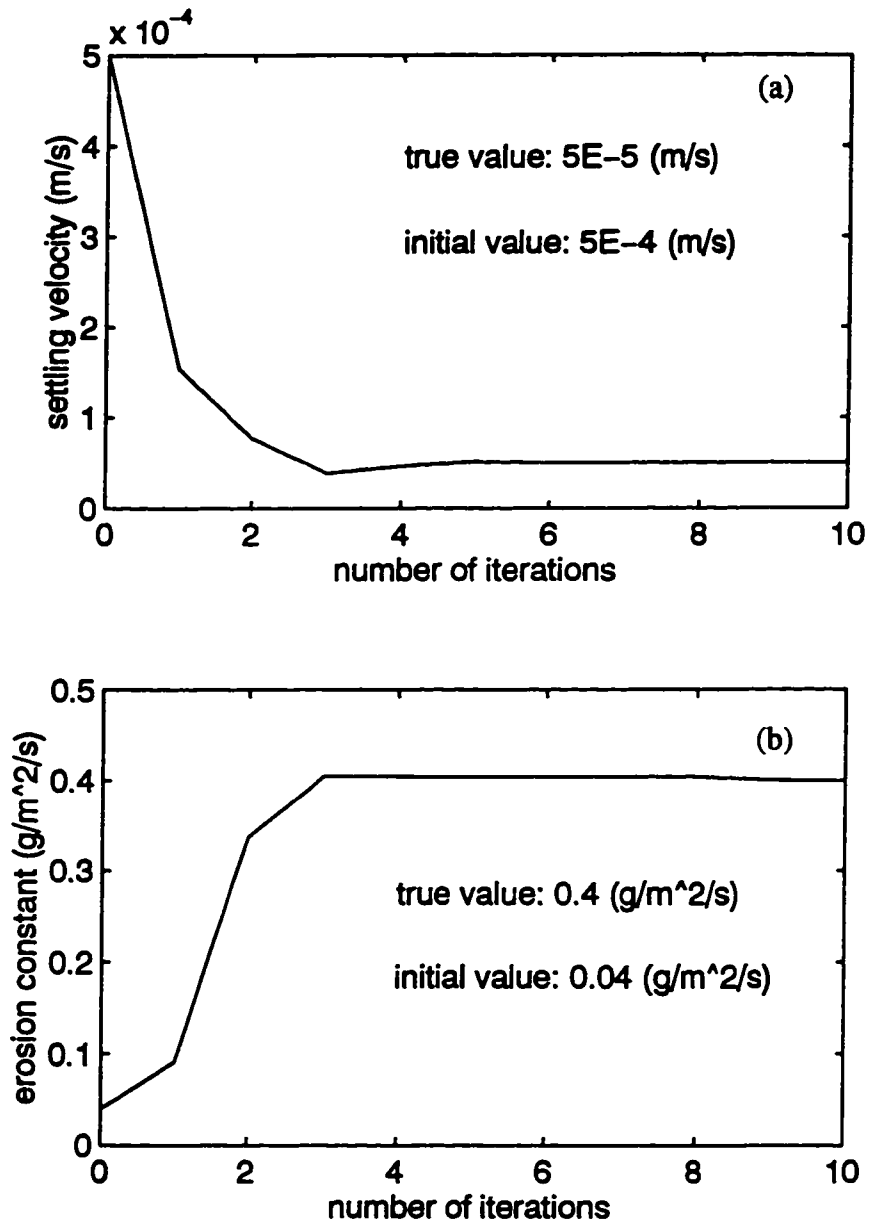
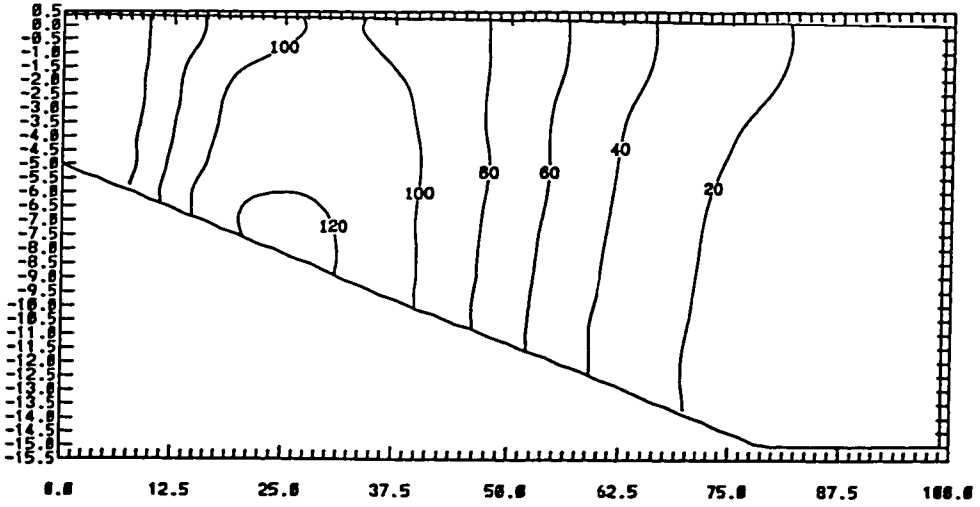
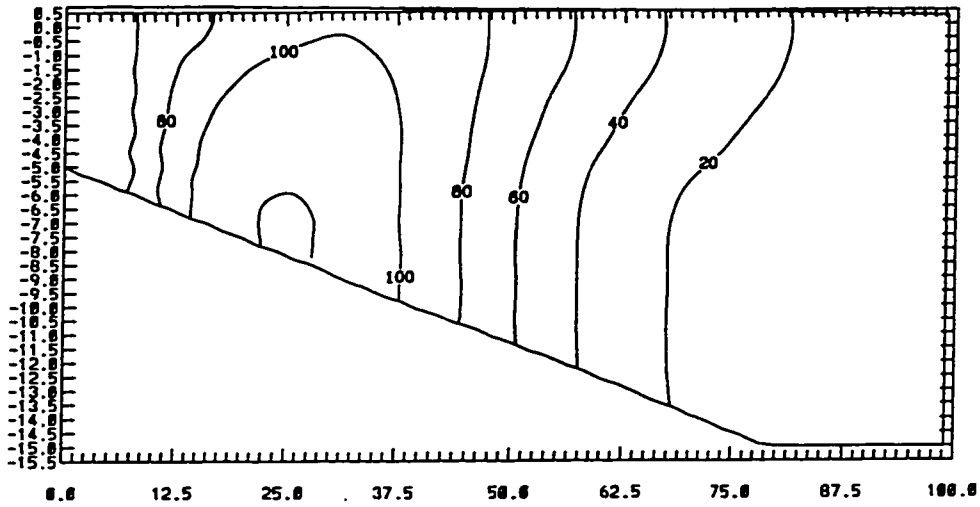
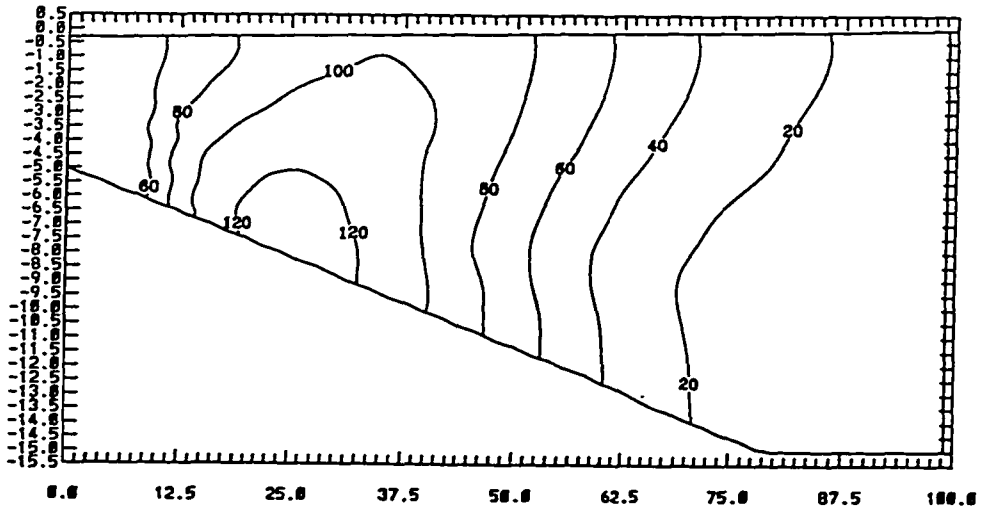
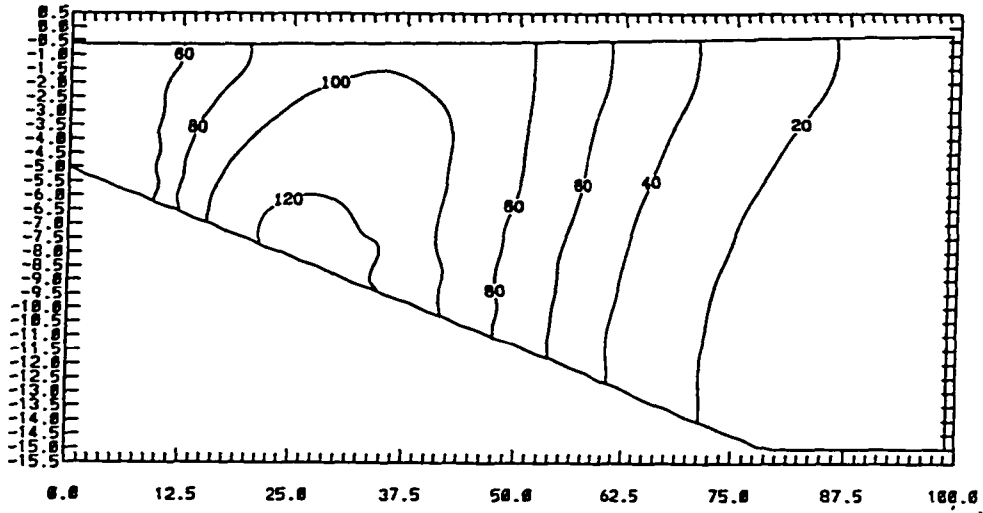


Fig. 42 Variations of settling velocity  $w_s$  (a) and erosion constant  $M_o$  (b) (initial guess I)



**Fig. 43 Initial suspended sediment distribution (mg/l) at four tidal phases (T/4, T/2, 3T/4 and T) along the axis of the estuary channel (initial guess II)**





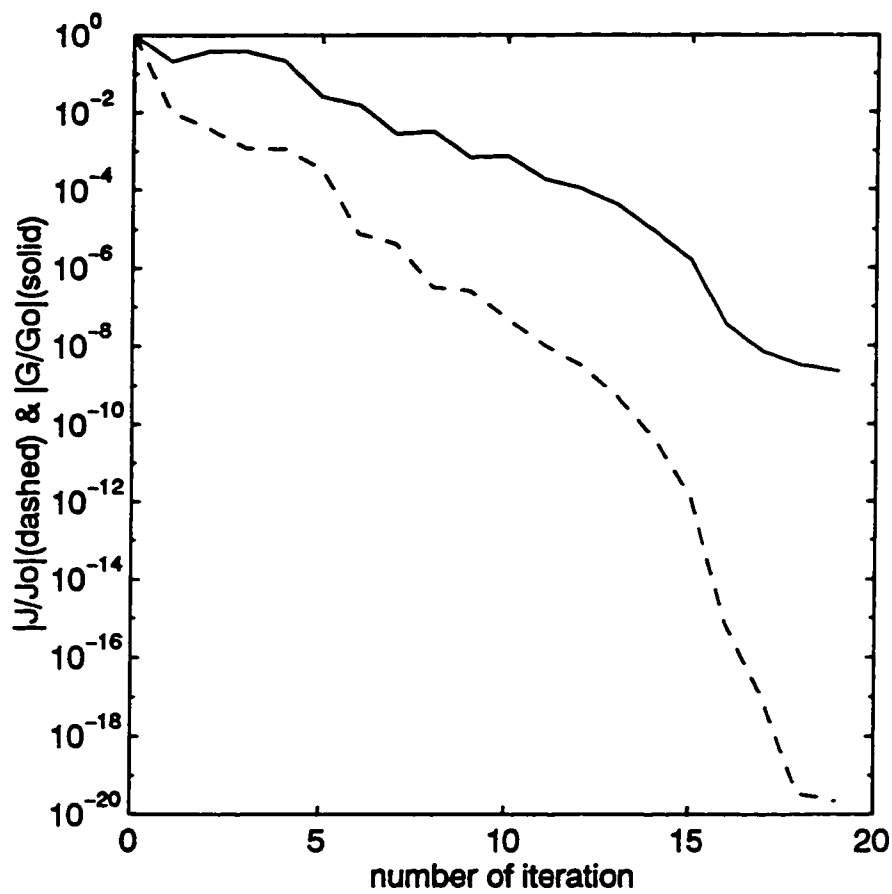


Fig. 44 Variations of  $|J_n/J_0|$  and  $|\nabla J_n/\nabla J_0|$  (initial guess II)

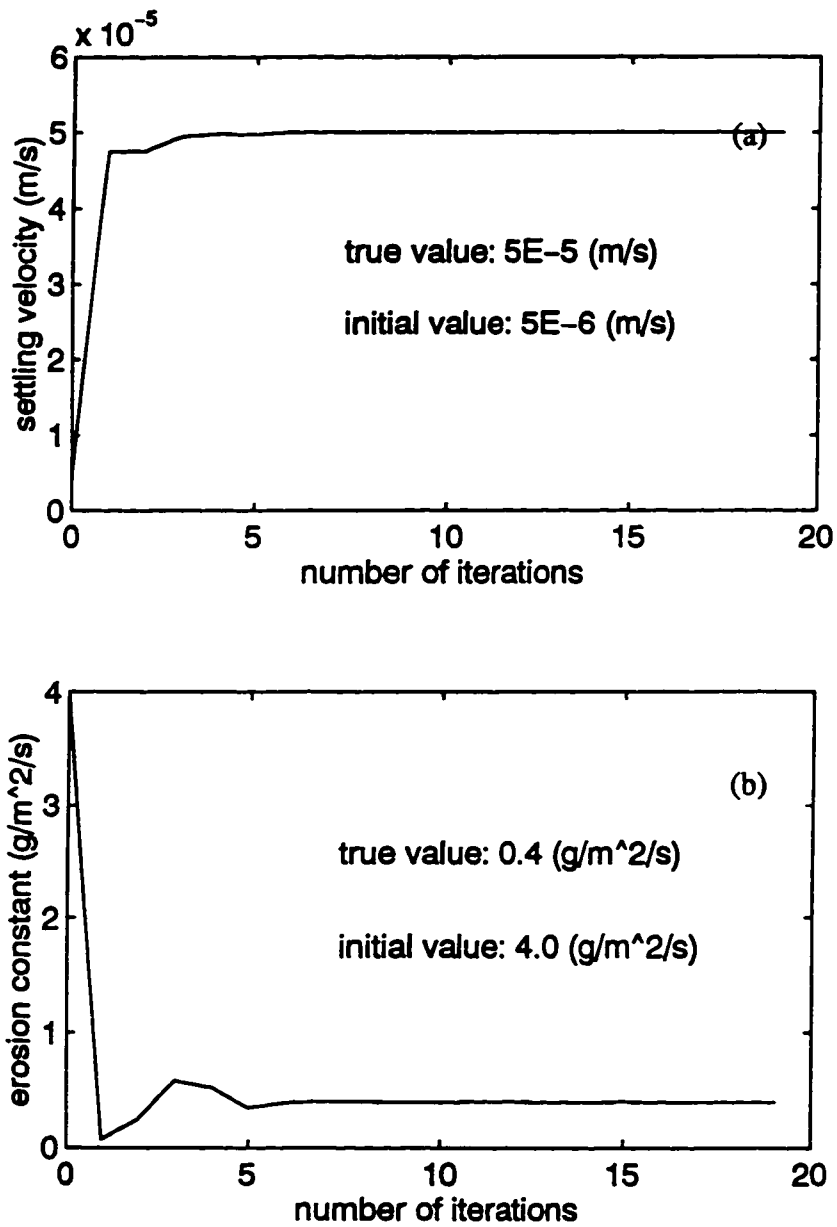


Fig. 45 Variations of settling velocity  $w_s$  (a) and erosion constant  $M_o$  (b) (initial guess II)

## 5.5 Model Application in The James River

### 5.5.1 Physical Background of The James River

The inverse model of cohesive sediment transport is also tested in the James River, one of the many drowned river valley tributaries in the Chesapeake Bay (Fig. 46). The James River estuary is a classic coastal plain estuary. The length of the estuary is about 161 km from the mouth to the fall line at Richmond. The average width is 5.1 km and the water depth is relatively shallow with average of 5.8 m. The estuary floor is shaped into a narrow central channel bordered by submerged shoals. The deepest depth is 29 m and located at the northwest of Mulberry Point (MP). Nichols, *et al.* (1991) classified the morphology of the James River into three distinct compartments: 1) bay-mouth, 2) estuary funnel and 3) meander zone. The bay-mouth zone covers a region from the estuary mouth extending 26 km seaward to the ocean, featuring a straight channel bothered by wide shallow banks (< 10 m). In the estuary funnel zone extending from Hampton Roads (HR) landward to Jordan Point (JP), meanders are broad and the axial channels are sinuous. The vertical profile of the estuary flow shows irregularities of depth (Nichols, 1972). Upstream of Jordan Point is the meander zone which is characterized by the pronounced meanders flanked by marshes and tidal flats. The physical and hydrodynamic characteristics of the James River estuary are listed in Table 9 (from Nichols, *et al.*, 1991). The estuary receives about  $2.4 \times 10^6$  tons of sediment load annually, most of it during the wet season from January to April.

The James River estuary is a typical partially mixed coastal plain estuary. The density-driven two-layer circulation is a distinct feature in the system. Pritchard (1952,

1954) examined the mean circulation pattern and salt flux in the James River based on field data in early 1950's. Calculation showed that the seaward flow in the upper layer can be as large as 9-40 times of the river inflow and thus causes a significant compensating landward flow in the bottom layer. The salt intrusion point may shift about 60 km along the estuary in response to the seasonal changes of river inflow, from upstream near Brandon Point to downstream on Burwell Bay (Fig. 46).

### **5.5.2 Numerical Model Setup**

A fully 3-D model for simulation of hydrodynamics and salinity transport in the James River estuary is setup and calibrated. Rectangular Cartesian grids are used in the whole domain, with grid size equal to 370 m in both the x- and y-directions. There are 202 grid cells in the x-direction and 150 grid cells in the y-direction and 5 levels in the vertical. The number of total horizontal water cells is 4610, only about 15% of total horizontal grid cells. A computational grid map is shown in Fig. 47. The model open boundary is extended further seaward from the James River mouth to reduce the effect of the uncertainty at the open boundary on the interior model domain of interest. There are 14 grid cells across the open boundary. In the extension portion of the model domain, solid boundaries are assumed in both the northern and southern lateral boundaries so that no normal flux boundary condition is applied. Water depth is assumed to be constant in the 5 x-direction grid cells adjacent to the open boundary. The tidal amplitudes and phases at all grid cells across the open boundary are assumed to be the same and a single  $M_2$  tidal constituent with amplitude of 0.375 m is specified at the open boundary. In the

present study, wind forcing is not considered. The number of time steps used in the model for one tidal cycle simulation is 288 and thus each time step interval is about 2.6 min. The salinity open boundary condition is specified with the maximum inflow salinity equal to 30 ppt and the recovery time to be 30 time steps (Fig. 22), which is about 77.6 min. A freshwater discharge of 100 cms at the head of the estuary is specified. The model was calibrated with respect to surface elevation, velocity and salinity using field data sets existing at VIMS.

### **5.5.3 Modeling Hydrodynamics and Suspended Sediment Transport**

Before simulating the distribution of suspended sediment in the James River, the hydrodynamic model should be calibrated first. Instantaneous salinity distributions at four different tidal phases at the surface layer and the bottom layer are plotted in Fig. 48 and Fig. 49, respectively. The contour plot starts from 0.5 ppt with a interval of 5 ppt in order to present the salinity intrusion limit (0.5 ppt) in the estuary. The surface salinity is significantly higher on the right-hand side (facing landward) than that on the left-hand side, which is caused by the Coriolis effect. The only large scale horizontal distribution of observed salinity in the James River was made in the early 1950's by Pritchard (1952). Fig. 50 (from Pritchard, 1952) shows the observed horizontal salinity distributions at high tide and low tide in September 3, 1950 in the James River. We can see that the salinity on the right-hand side is also higher than that on the left-hand side. Also from Fig. 48 we can see that the surface salinity at the downstream end of Burwell Bay (BB) varies from 10 ppt to almost 15 ppt within a tidal cycle, which is consistent with the



observations in Fig. 50. The bottom salinity (Fig. 49) shows a slightly different distribution pattern. Salinity on the right-hand side is not significantly higher than that on the left-hand side in the mid-portion of the estuary. The salinity is more constrained to the deep channel in the bottom layer. A vertical profile along the main channel of the James River estuary at the phase before flood at the mouth is plotted in Fig. 51. A vertical profile of observed salinity distribution along the main channel at slack water run before flood is plotted in Fig. 52 (Hepworth and Kuo, 1989). Compared to the field observation (Fig. 52), the model produces a similar salinity distribution pattern.

The cohesive sediment transport model for the James River case is the same as the one used in the idealized 3-D estuary (see section 5.4). The suspended sediment discharge concentration at the head is given as 25 mg/l (personal communication with Nichols). The initial suspended sediment concentration is assumed to be 50 (mg/l) in the whole domain and the initial bed sediment per unit area is specified as 2000 (g/m<sup>2</sup>). The settling velocity, erosion constant, critical shear stresses for deposition and erosion are first roughly tuned such that suspended sediment distribution is in a reasonable agreement with observations reported by Nichols (1972). The final adjusted settling velocity and erosion constant are  $w_s=5\times 10^{-5}$  (m/s) and  $M_o=0.03$  (g/m<sup>2</sup>/s) respectively, while the critical shear stresses for deposition and erosion are set to be  $\tau_{cd}=0.4$  (dyne/cm<sup>2</sup>) and  $\tau_{cr}=0.7$  (dyne/cm<sup>2</sup>). After 100 tidal cycles, a turbidity maximum is well developed near the Jamestown Island. The instantaneous horizontal distribution of surface suspended sediment concentration at four phases of a M<sub>2</sub> tidal cycle is shown in Fig. 53 in both contour and color scales. The contours start at 50 mg/l with an interval of 50 mg/l. We

can see clearly that the location of the turbidity maximum is coincided with the salt intrusion limit (0.5 ppt isohaline in Fig. 48). The turbidity maximum migrates with tidal motion up and down the channel in a distance of approximated 8 km. The maximum sediment concentration at the surface is about 180 mg/l. The instantaneous suspended sediment concentration in the bottom layer is given in Fig. 54. Comparing this to the concentration distribution at the surface, we can see that the concentration is much higher than that at the surface. Also, in addition to the turbidity maximum at Jamestown Island, there is another high concentration zone in the southern region of Burwell Bay, which is not observed at the surface. This phenomena can be explained partially by the mean circulation pattern. The Eulerian mean velocity distributions at the surface and bottom are shown in Fig. 55 and Fig. 56. From Fig. 55 we can see that a strong and large clockwise tidal residual eddy (with maximum velocity about 10cm/s) is formed in lower Burwell Bay while a weak anti-clockwise eddy is formed in upper Burwell Bay. In the bottom layer, the eddies do not exist due to the complicated topographic feature in Burwell Bay. This indicates that suspended sediment is trapped in Burwell Bay and settles to the bottom layer. The comparison of depth changes on U.S. Coast and Geodetic Survey boat sheets in 70 years from 1873 to 1943 also shows that the greatest sedimentation rate occurs in Burwell Bay (Fig. 57, from Nichols, 1972). Based on field observations in 1960's, Nichols (1972) found that the mean turbidity maximum is located around Hog Point (Fig. 46), a little downstream of Jamestown Island. Concentration magnitudes at the turbidity maximum from the model are about 100 mg/l at the surface and 300 mg/l at the bottom, which are reasonable compared to historic field

measurements (Nichols, 1972). The field observations (Nichols, 1972) also showed that upstream of Jamestown Island, the suspended sediment concentrations is around 30 mg/l, while in the lower portion of the estuary, sediment concentration are generally below 20 mg/l, which are also shown in the model results.

#### 5.5.4 Inverse Experimental Results

To test the inverse model for the suspended sediment transport problem, twin experiments were conducted. The forward model was run for 10 tidal cycles to generate "observation" data with the settling velocity  $w_s=5\times 10^{-5}$  (m/s) and the erosion constant  $M_o=0.03$  (g/m<sup>2</sup>/s). The "observation" data are sampled at 5 locations around the turbidity maximum at the end of each tidal cycle. The initial guesses for  $w_s$  and  $M_o$  are  $5\times 10^{-4}$  (m/s) and 0.003 (g/m<sup>2</sup>/s), *i.e.*, increasing  $w_s$  by an order and decreasing  $M_o$  by an order. The minimization procedure converged very fast and the true solutions are retrieved to the accuracy of 4 digits in 7 iterations. The variations of the normalized cost function and the gradient norm versus the number of iterations are plotted Fig. 58. We can see that the cost function is reduced by an order of  $10^9$  and the gradient by an order of  $10^6$ . The recovery processes for the settling velocity and erosion constant are plotted in Fig. 59. Different initial guesses for  $w_s$  and  $M_o$  were also tested. The convergence of the normalized cost function and gradient norm are shown in Fig. 60 when initial guesses of  $w_s$  and  $M_o$  are set to be  $5\times 10^{-6}$  (m/s) and  $M_o=0.3$  (g/m<sup>2</sup>/s), respectively. Fig. 61 shows that the minimization procedure converges to the true solution in 15 iterations.

## 5.6 Conclusions and Future Studies

In this chapter, a variational data assimilation scheme for estimation of sediment settling velocity  $w_s$  and erosion constant  $M_o$  in a cohesive sediment transport model is developed. Some very preliminary tests of the inverse model were performed in an idealized 3-D estuary and the James River, a tributary in the lower Chesapeake Bay. Experimental results show that the inverse model can successfully recover both parameters within 30 iterations when observations are available in the turbidity maximum region of the spatial and temporal domains. The successful model tests demonstrate that variational data assimilation techniques can be a useful tool to identify poorly determined model parameters in cohesive sediment transport model, such as settling velocity and resuspension rate.

There are still many related issues which need to be addressed through future experiments since only very simple twin experiments were conducted in the present study. First, the critical shear stresses for deposition ( $\tau_{cd}$ ) and erosion ( $\tau_{cr}$ ) are not considered in the present inverse model. It may be necessary to include  $\tau_{cd}$  and  $\tau_{rd}$  in the inverse model since changes in either  $\tau_{cd}$  or  $\tau_{rd}$  will actually change the time span as well as the magnitude of deposition or erosion. For uniformly distributed  $\tau_{cd}$  and  $\tau_{rd}$  in the whole modeling domain, the gradients of the cost function with respect to  $\tau_{cd}$  and  $\tau_{cr}$  can be derived from Eq. (76). Noticing that the first term in the right-hand side of Eq. (76) is not related to  $\tau_{cd}$  and  $\tau_{cr}$ , we then have:

$$\partial_{\tau_{cd}} J = - \int_T \int_{\Omega} \lambda w_s C_1 \left( \frac{\tau_b}{\tau_{cd}^2} \right) d\Omega dT ; \quad \tau_b < \tau_{cd} \quad (83)$$

and

$$\partial_{\tau_{cr}} J = - \int_T \int_{\Omega} \lambda M_o \left( \frac{\tau_b}{\tau_{cr}^2} \right) d\Omega dT ; \quad \tau_b > \tau_{cr} \quad (84)$$

Since  $w_s$ ,  $M_o$ ,  $C_1$ ,  $\tau_b$ ,  $\tau_{cd}$  and  $\tau_{cr}$  are all positive quantities, the signs of the gradients

Similar to the salinity open boundary problem, sensitivity runs are necessary to see how the variational inverse model works when dealing with different types of data sets. It should be pointed out that in the twin experiments presented in this Chapter, all the data are located near the turbidity maximum region. However, in the real study, the observations may not be in that region. It would be interesting to test the inverse model using the data sampled downstream or upstream of the turbidity maximum. Another important issue is the temporal distribution of the data. In the current study, data are sampled at an interval of every tidal cycle. So for a 10 tidal cycle simulation, we have 10 data sets in time. From a practical point of view, it is not easy to obtain long time series of data for suspended sediment concentration. Therefore, more experiments should be conducted to test the inverse model for the cases of less data in time or shorter simulation periods (e.g., only one tidal cycle instead of 10 tidal cycles). Sensitivity runs should also be carried out to study how the total number of observation data in space and time will affect the retrieved solutions and to determine the minimum number of data required to retrieve satisfactory solutions. Compared to the field measurement of salinity, the measurement of suspended sediment concentration would be much less accurate. It

is particularly important to add noisy signals in the model generated data and to test the inverse model.

In the present study, both settling velocity  $w_s$  and erosion constant  $M_o$  are assumed constant throughout the modeling domain. However, they are not constant in reality. The effects of salinity and sediment concentration (flocculation) on the settling velocity  $w_s$  should be on the agenda of future studies for the forward problem. The erosion constant  $M_o$  also depends on the surface sediment texture distribution on the bottom, even though there is not a general and widely used formula to describe the erosion rate as a function of bottom sediment texture. It will be of significance to consider the erosion constant  $M_o$  as regionally dependent, based on the information of bottom sediment texture. For example, the sand and mud ratio along the James River channel is characterized by very high ratios (70%) at the mouth and upstream of Jordan Point. In the central part of the estuary, the sand and mud ratio is less than 20% (Nichols, *et. al.*, 1991). In this case  $M_o$  can be assumed to vary upstream, the central and the mouth regions of the estuary.

Another shortcoming of the present study on the modeling of sediment transport process is that only a single class of sediment is considered. To describe fully the sediment transport more realistically, multi-classes of sediments should be included in the numerical model. Thus, for the inverse problem, a set of settling velocities  $w_s$  and erosion constants  $M_o$  will be treated as control variables corresponding to each class of sediment.

Table 9. Physical and hydrodynamic characteristics of the James River estuary  
(from Nichols, *et al.*, 1991)

|  |                                     |
|--|-------------------------------------|
| Fluvial and estuarine drainage area          | 26,360 km <sup>2</sup>              |
| Surface area                                 | 611 km <sup>2</sup>                 |
| Precipitation                                | 1079 mm/yr                          |
| Length                                       | 161 km                              |
| Width (average)                              | 5.1 km                              |
| Depth (average)                              | 5.8 m                               |
| Depth/width ratio                            | 0.0011                              |
| Volumetric capacity (MLW)                    | 2.5 km <sup>3</sup>                 |
| Freshwater inflow (average)                  | 213 m <sup>3</sup> /s               |
| Low flow                                     | 28 m <sup>3</sup> /s                |
| High flow                                    | 322 m <sup>3</sup> /s               |
| Flood  | > 1500 m <sup>3</sup> /s            |
| Tidal prism                                  | 0.28×10 <sup>9</sup> m <sup>3</sup> |
| Tide range (average)                         | 70 cm                               |
| Flow ratio (average) <sup>1</sup>            | 0.10                                |
| Low flow                                     | 0.03                                |
| Mean hydraulic residence time <sup>2</sup>   | 219 days                            |
| High flow                                    | 5 days                              |
| Mean fresh water fraction residence time     | 138 days                            |
| Suspended sediment load in turbidity maximum | 100-270 mg/l                        |

<sup>1</sup> Proportion of freshwater entering during a tidal cycle to the tidal prism.

<sup>2</sup> Volumetric capacity divided by average river inflow.

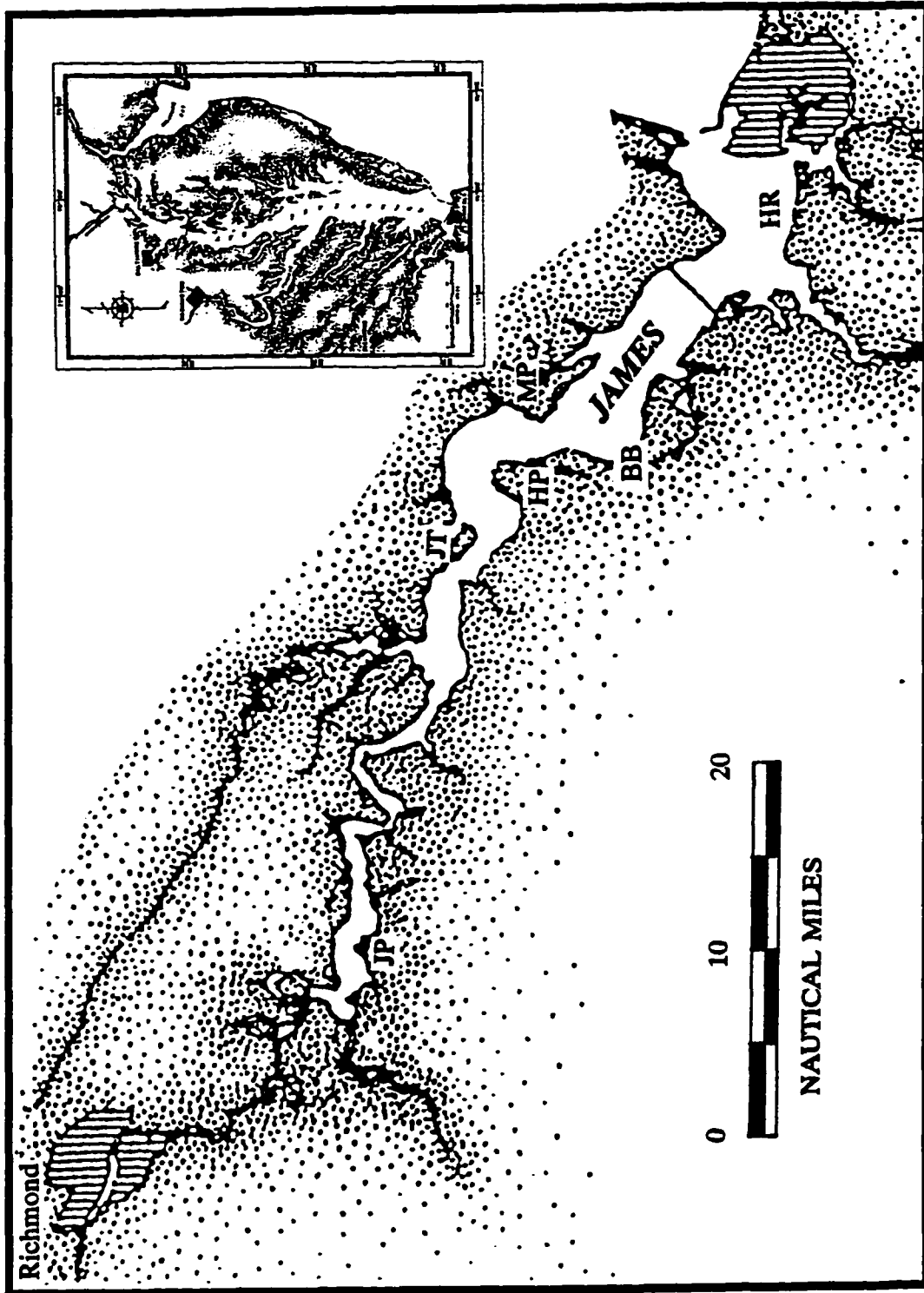


Fig. 46 Location of the James River estuary in the Chesapeake Bay region



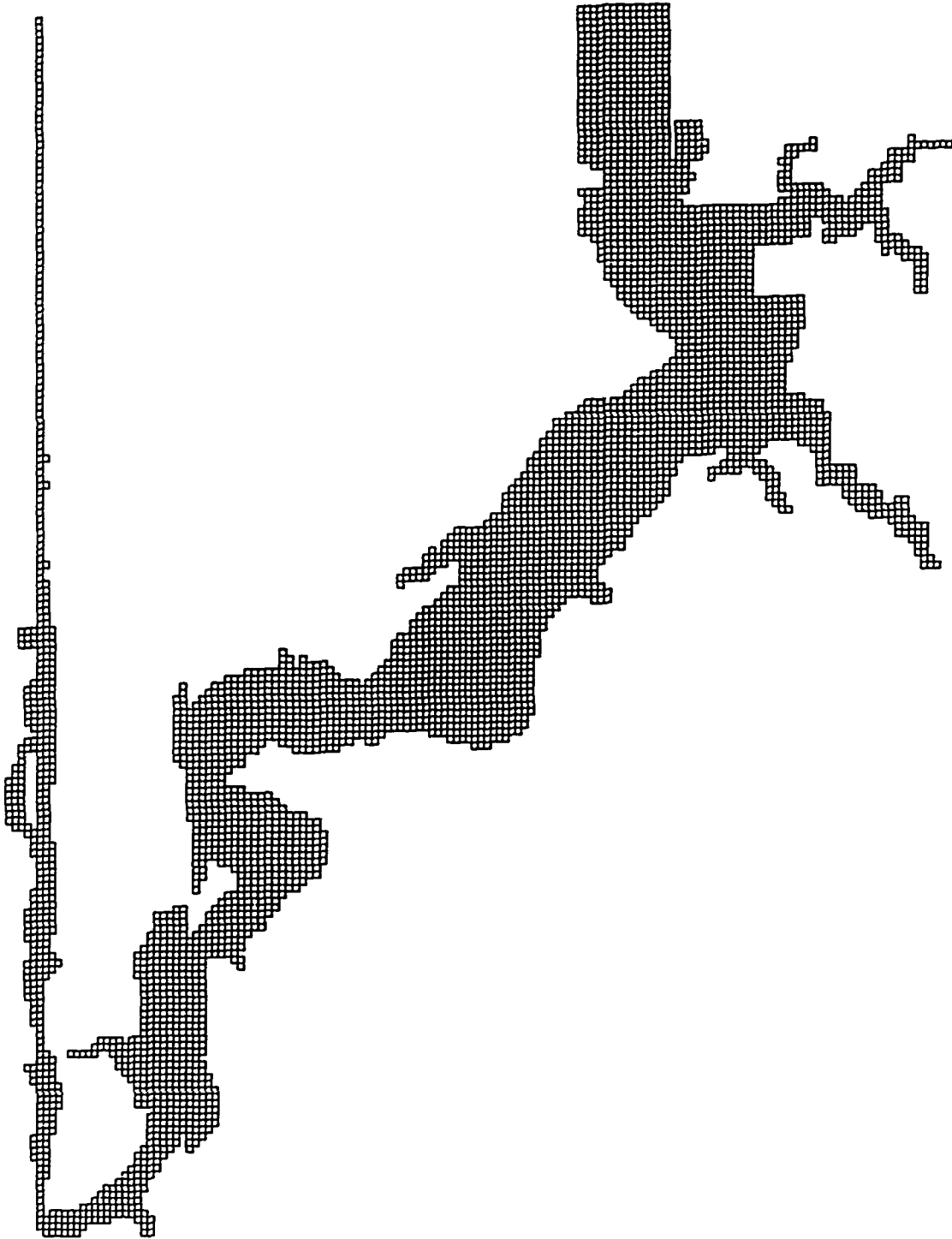
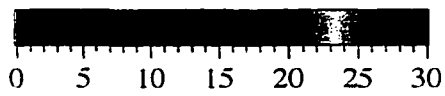
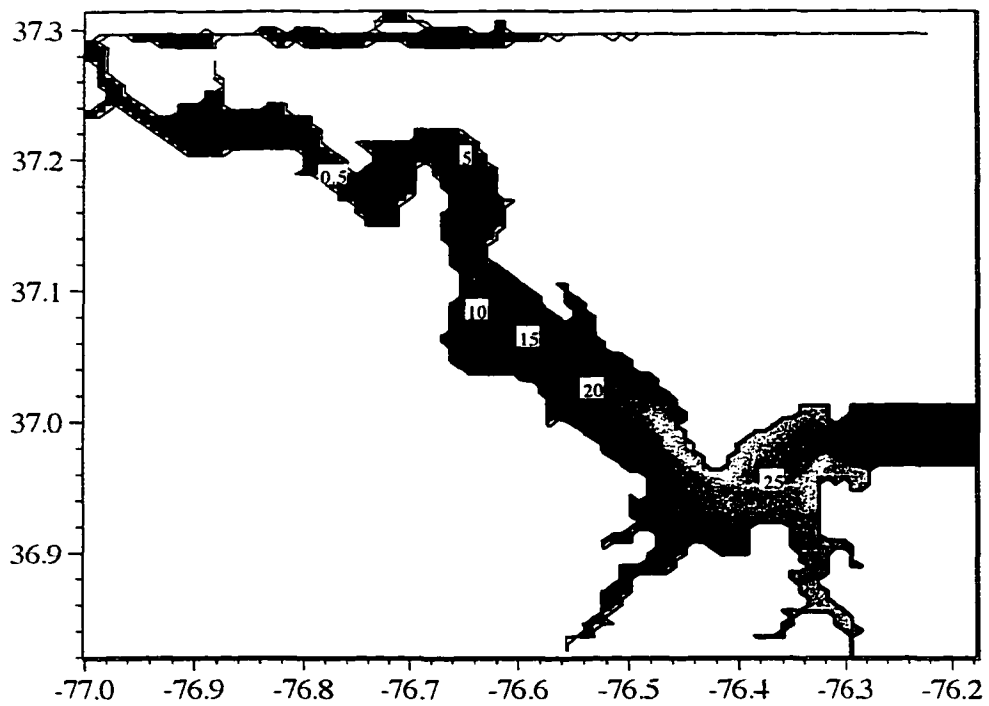
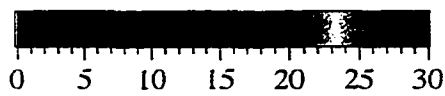
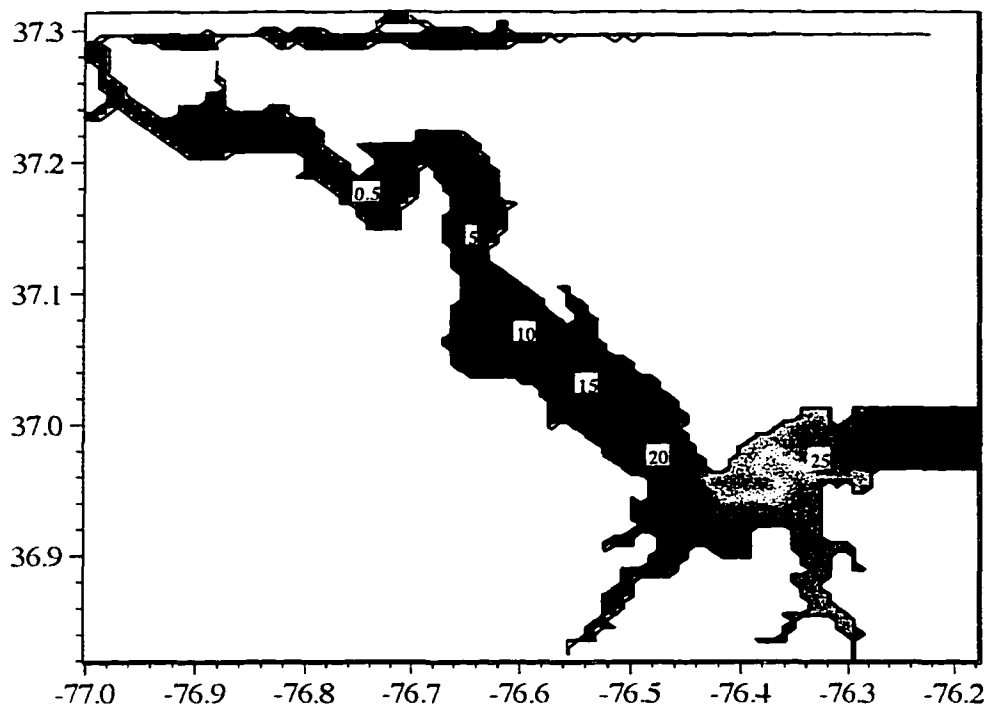
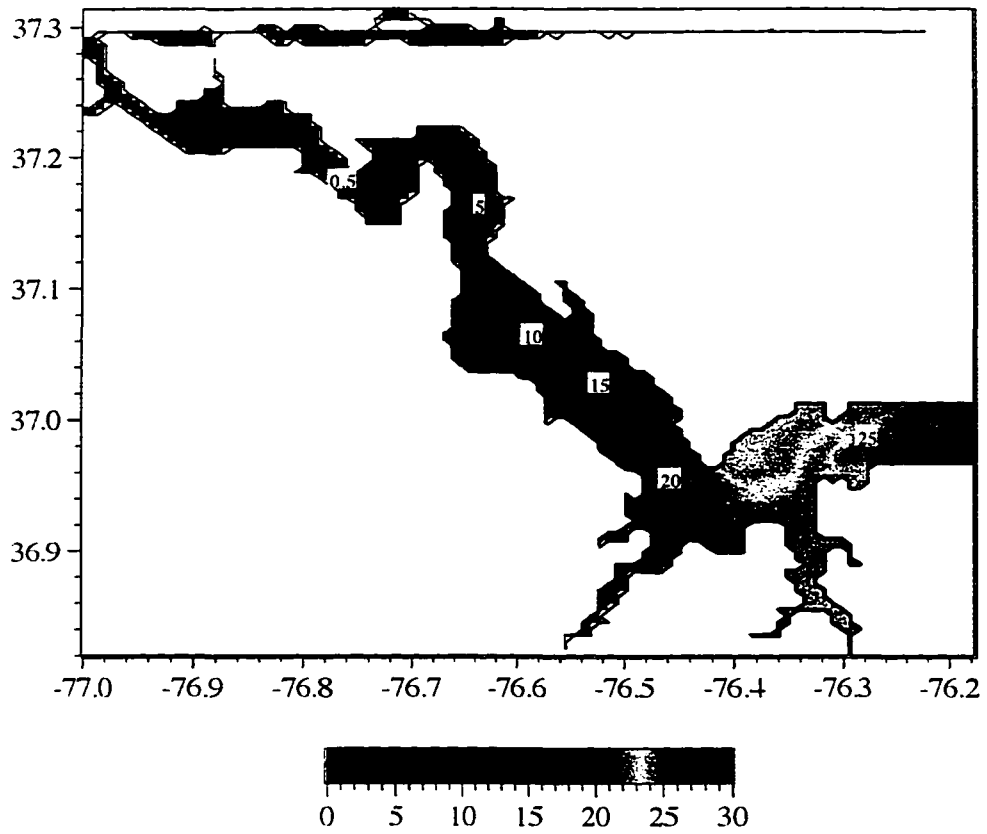
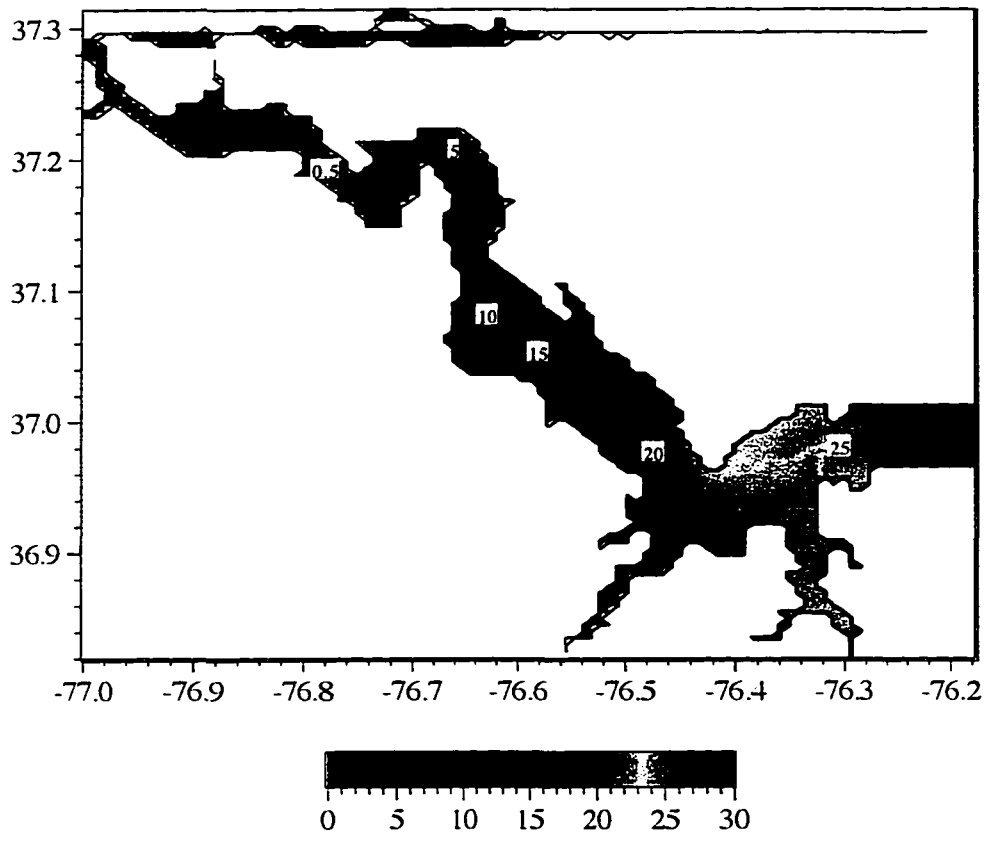


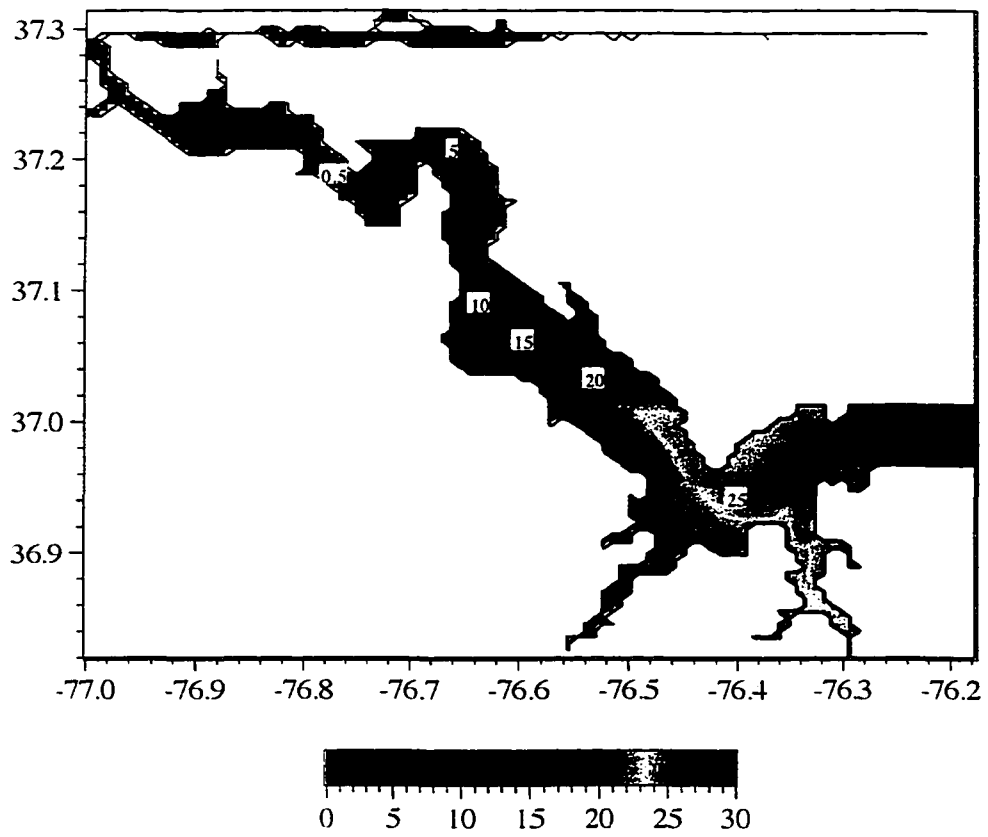
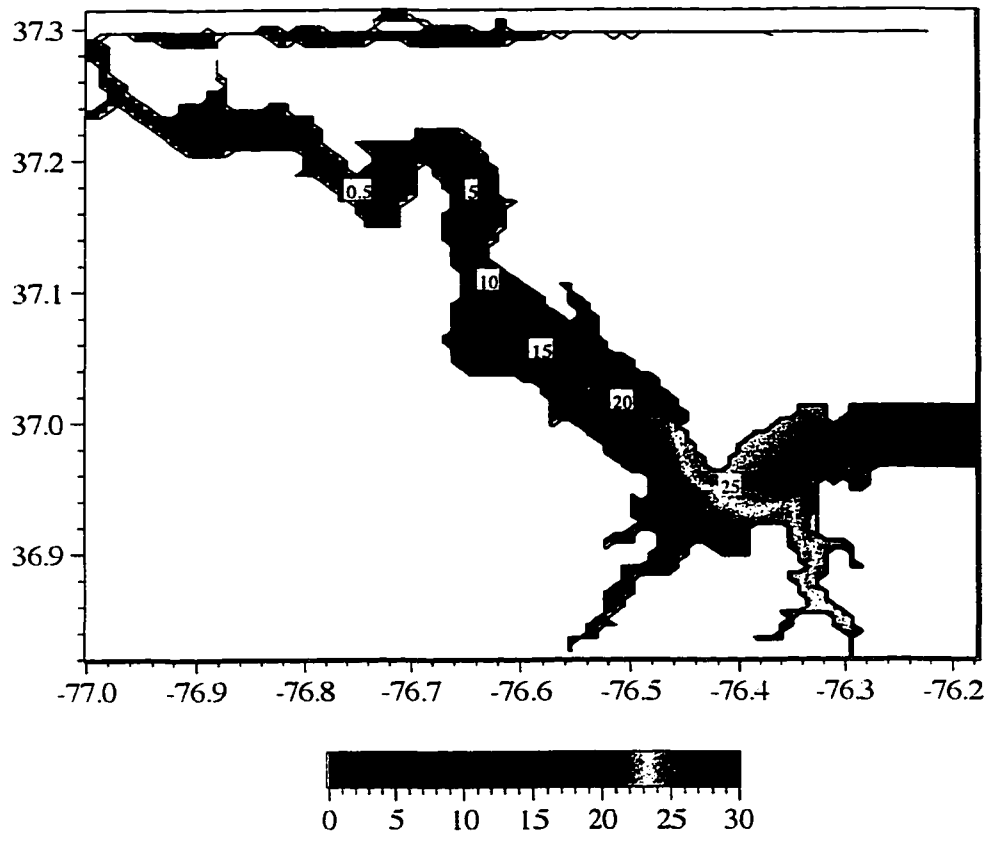
Fig. 47 Grid map of the James River model

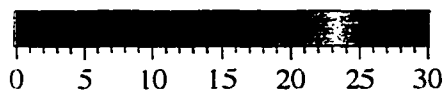
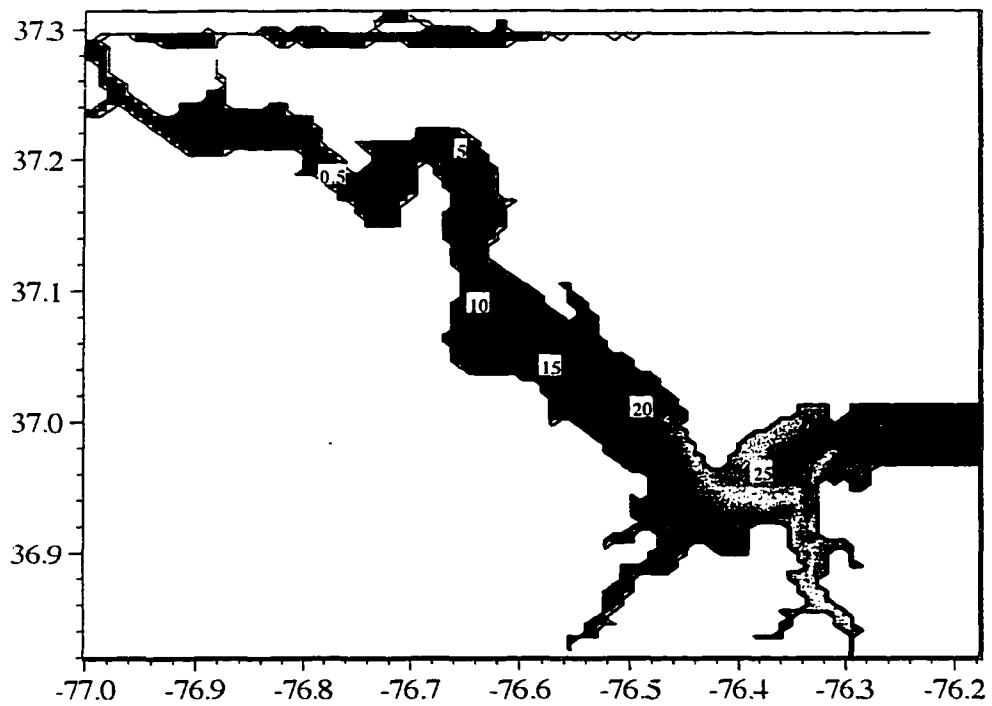
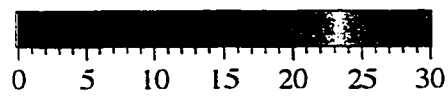
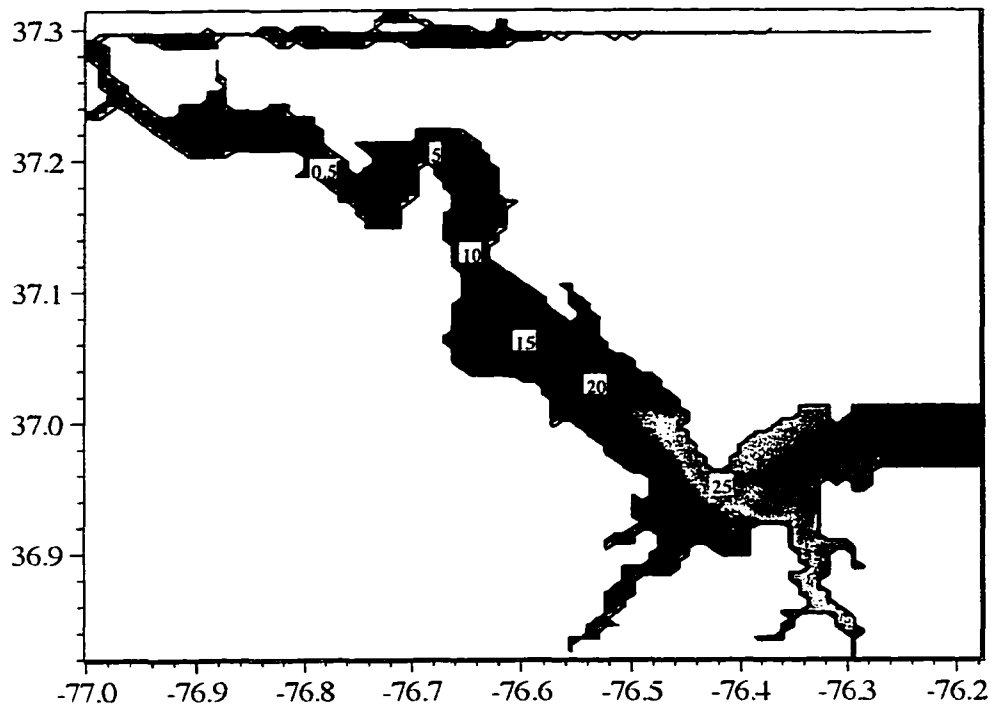
**Fig. 48 Surface salinity distribution (ppt) in the James River  
at four tidal phases ( $T/4$ ,  $T/2$ ,  $3T/4$ ,  $T$ ).**





**Fig. 49. Bottom salinity distribution (ppt) in the James River  
at four tidal phases ( $T/4$ ,  $T/2$ ,  $3T/4$ ,  $T$ ).**





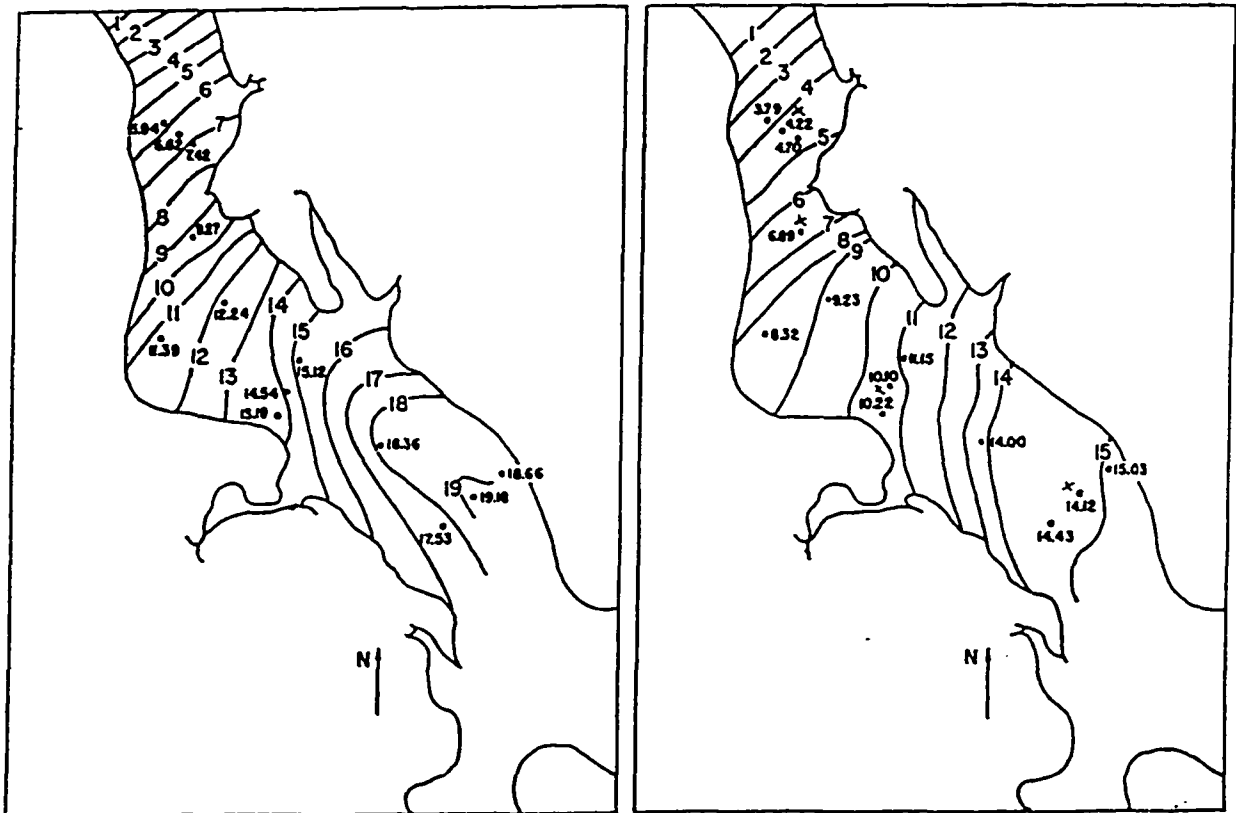


Fig. 50 Surface salinity distribution (ppt) in the Burwell Bay region of James River at high water (left panel) and low water (right panel) on 2 September 1950.

(from D. W. Pritchard, 1952)



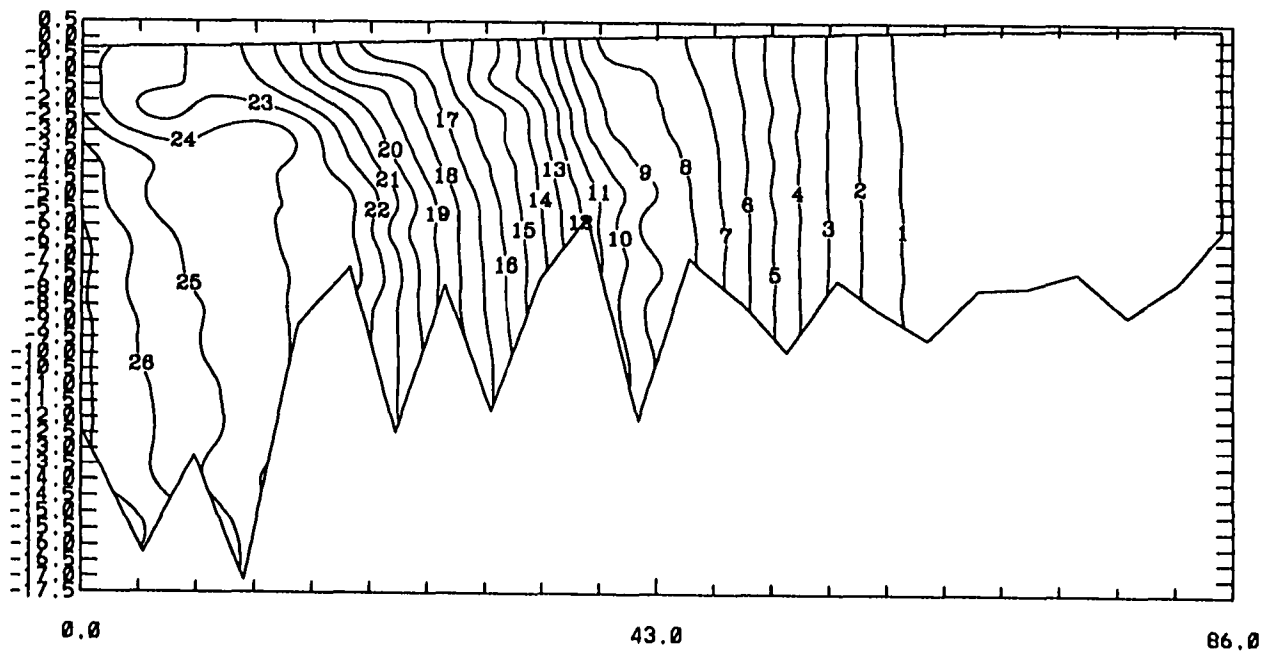


Fig. 51. Calculated vertical profile of salinity (ppt) at phase before flood  
at the mouth in the James River.

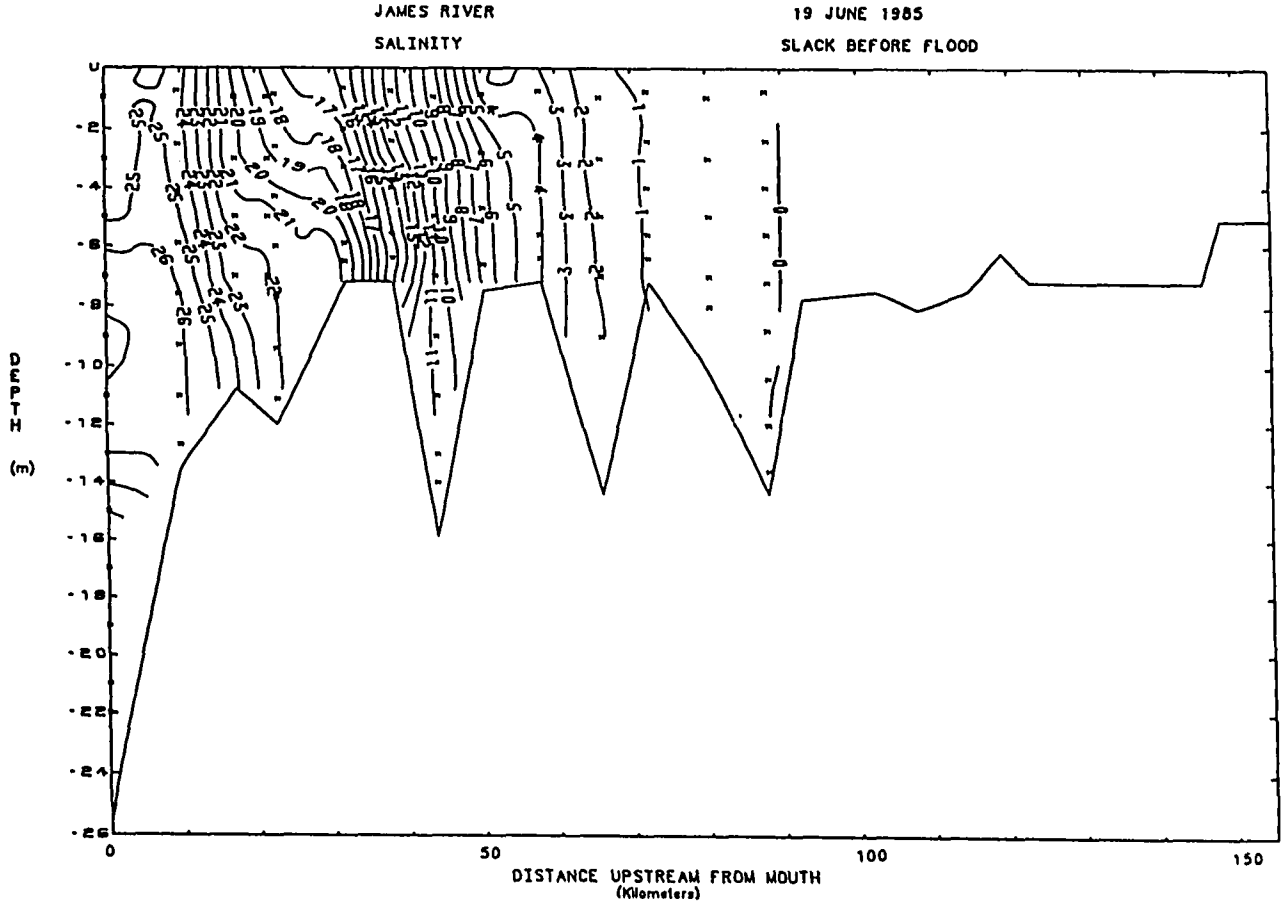
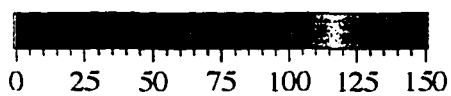
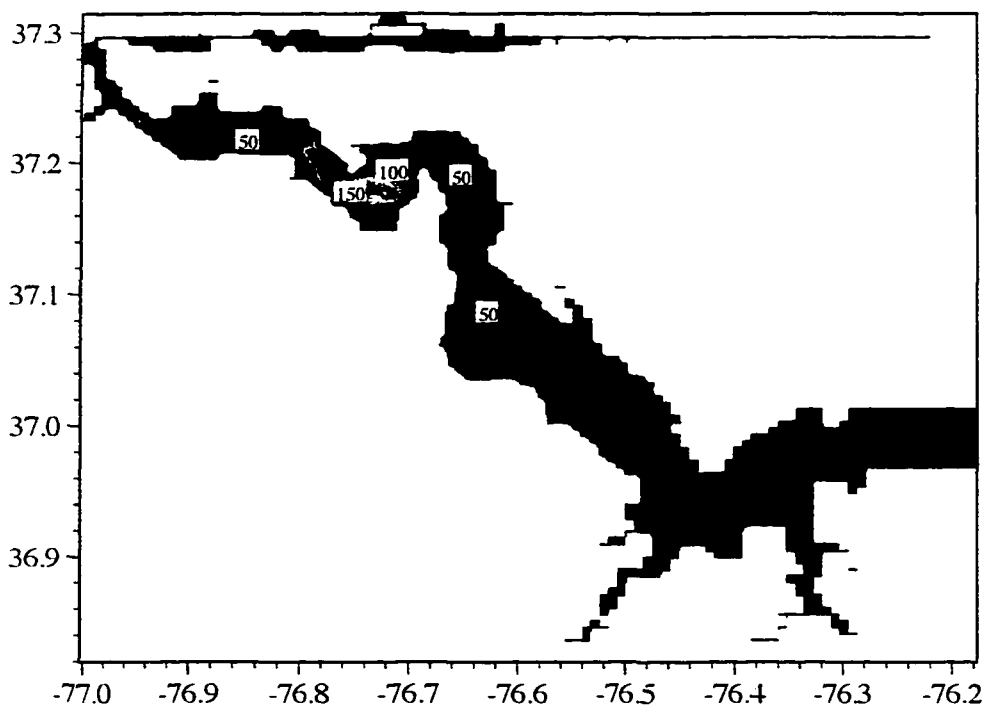
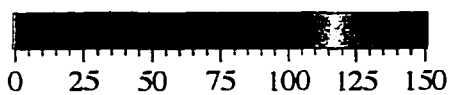
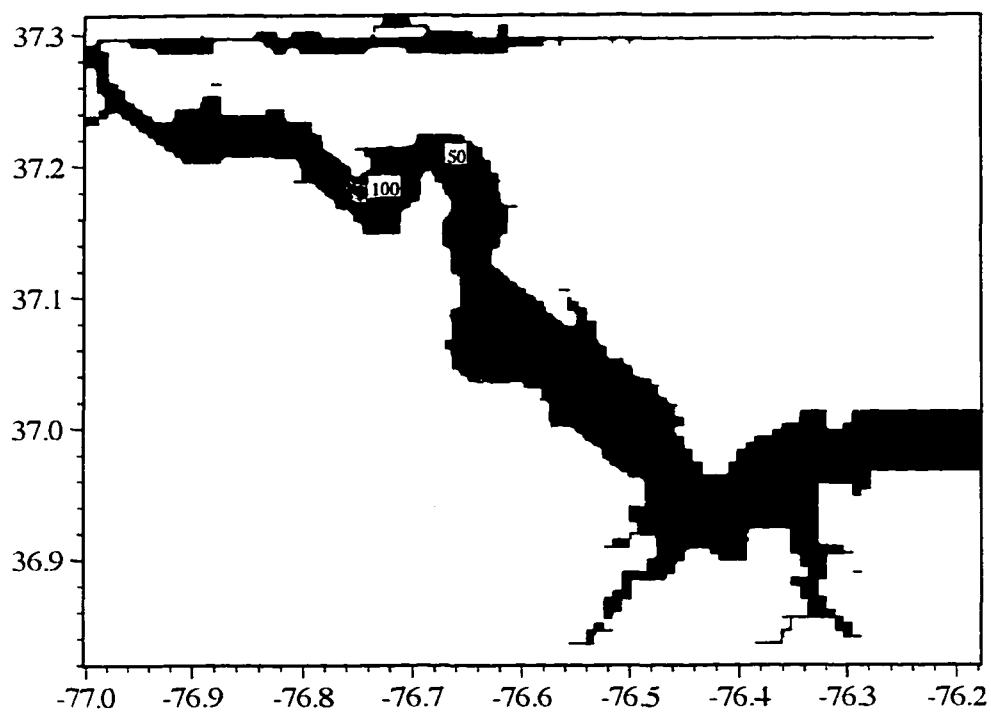
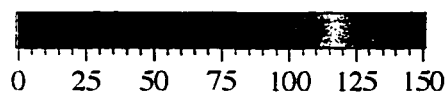
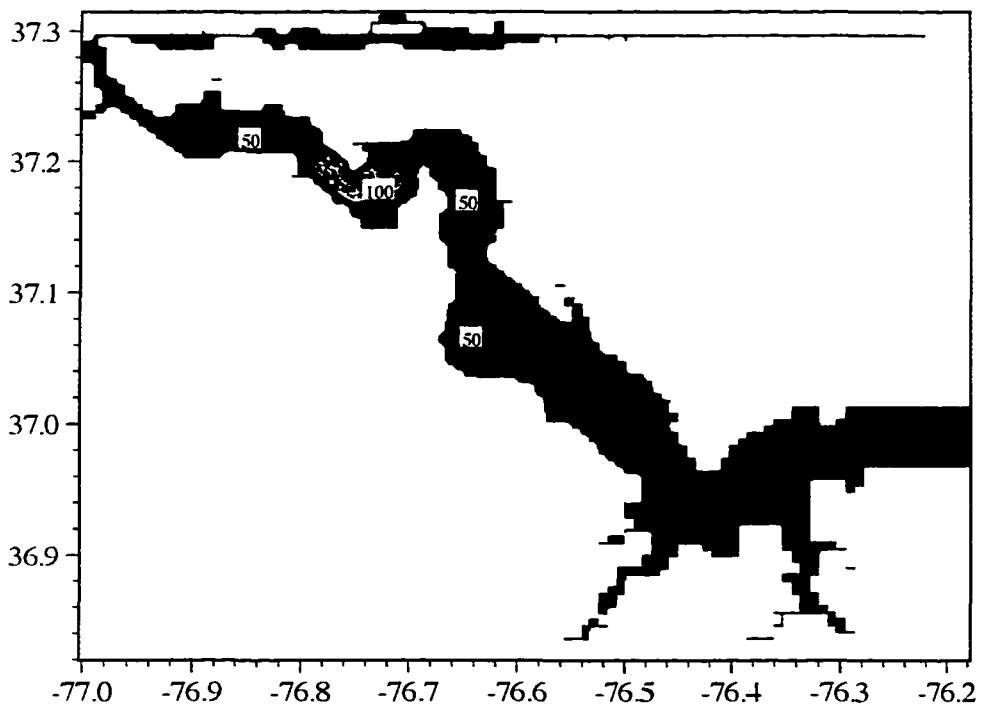
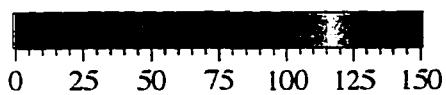
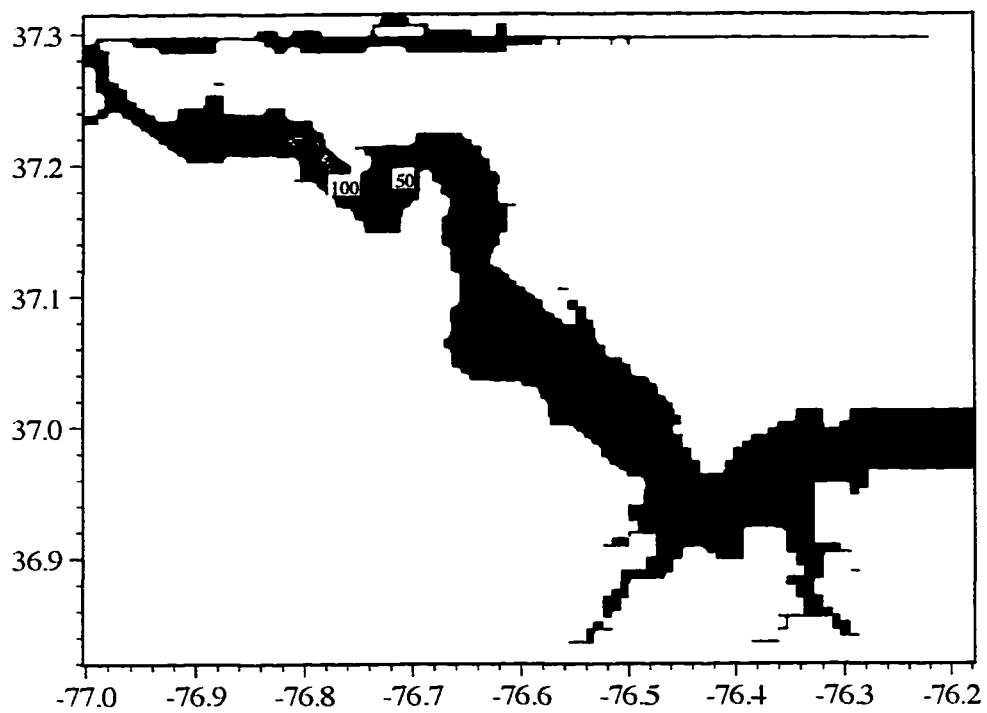


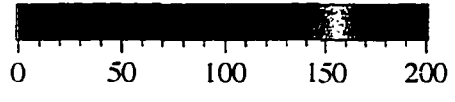
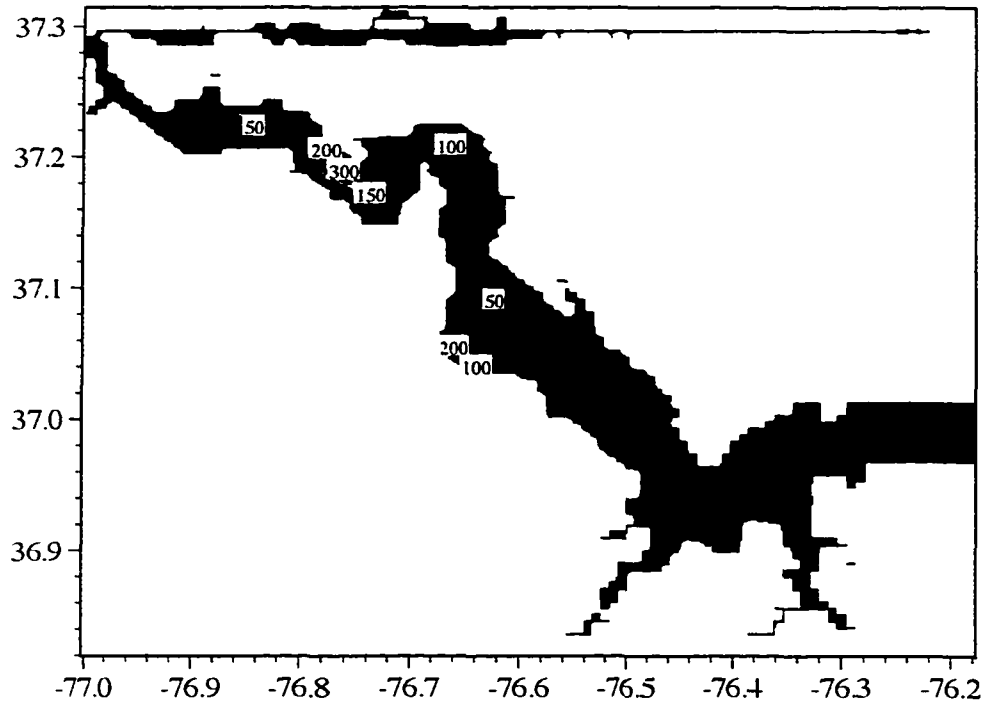
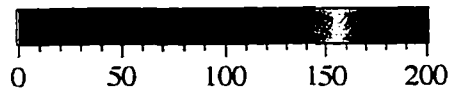
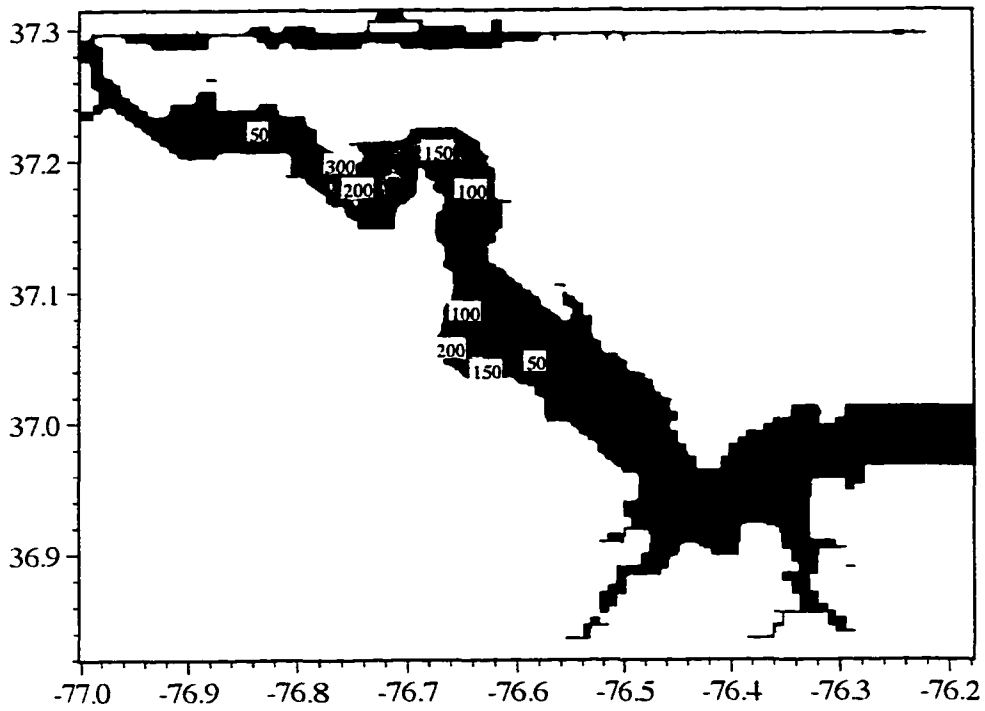
Fig. 52. Observed vertical profile of salinity (ppt) at slack water before flood in the James River in June 19, 1985 (from Hepworth and Kuo, 1989).

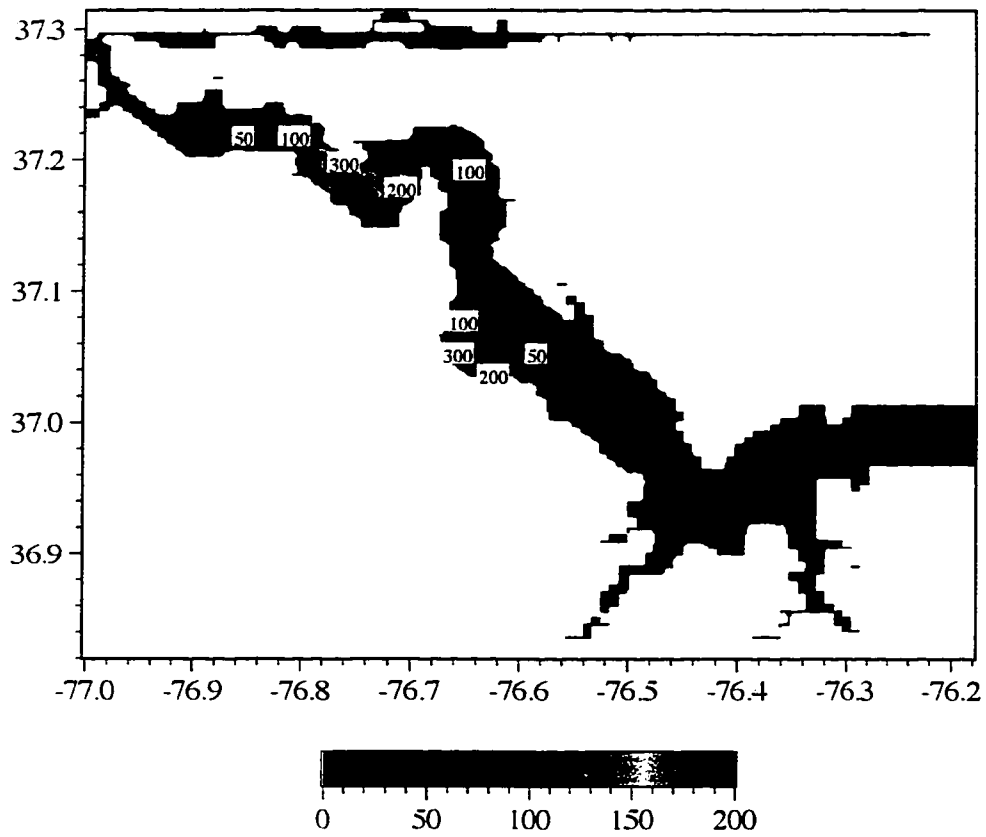
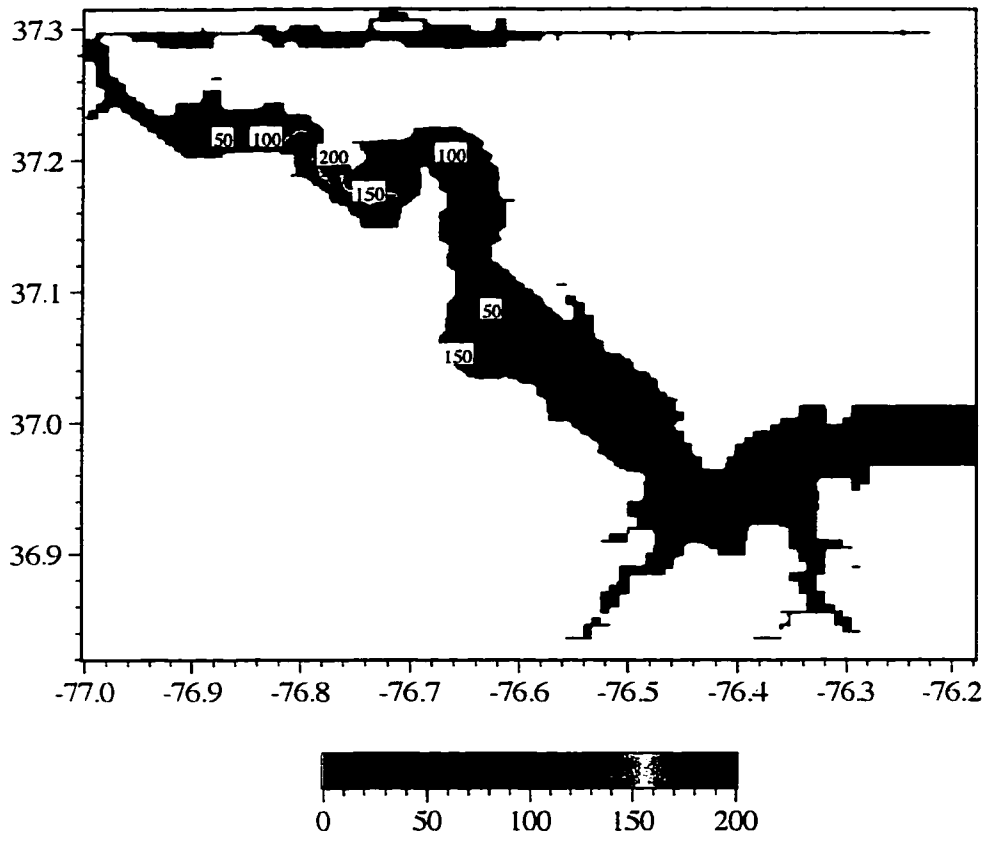
**Fig. 53. "Observed" surface suspended sediment distribution (mg/l)  
at four tidal phases (T/4, T/2, 3T/4, T) in the James River.**





**Fig. 54 "Observed" bottom suspended sediment distribution (mg/l)  
at four tidal phases (T/4, T/2, 3T/4, T) in the James River.**







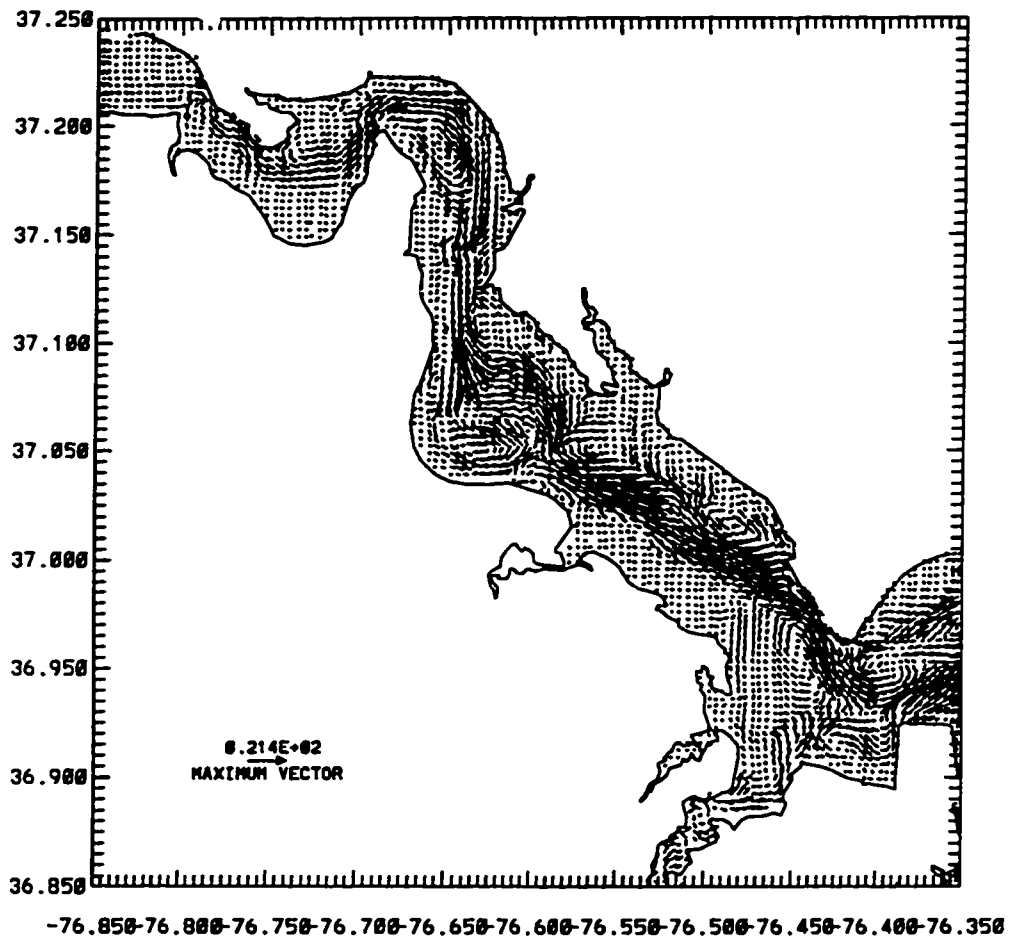


Fig. 55 The Eulerian mean velocity (cm/s) at the surface layer in the James River

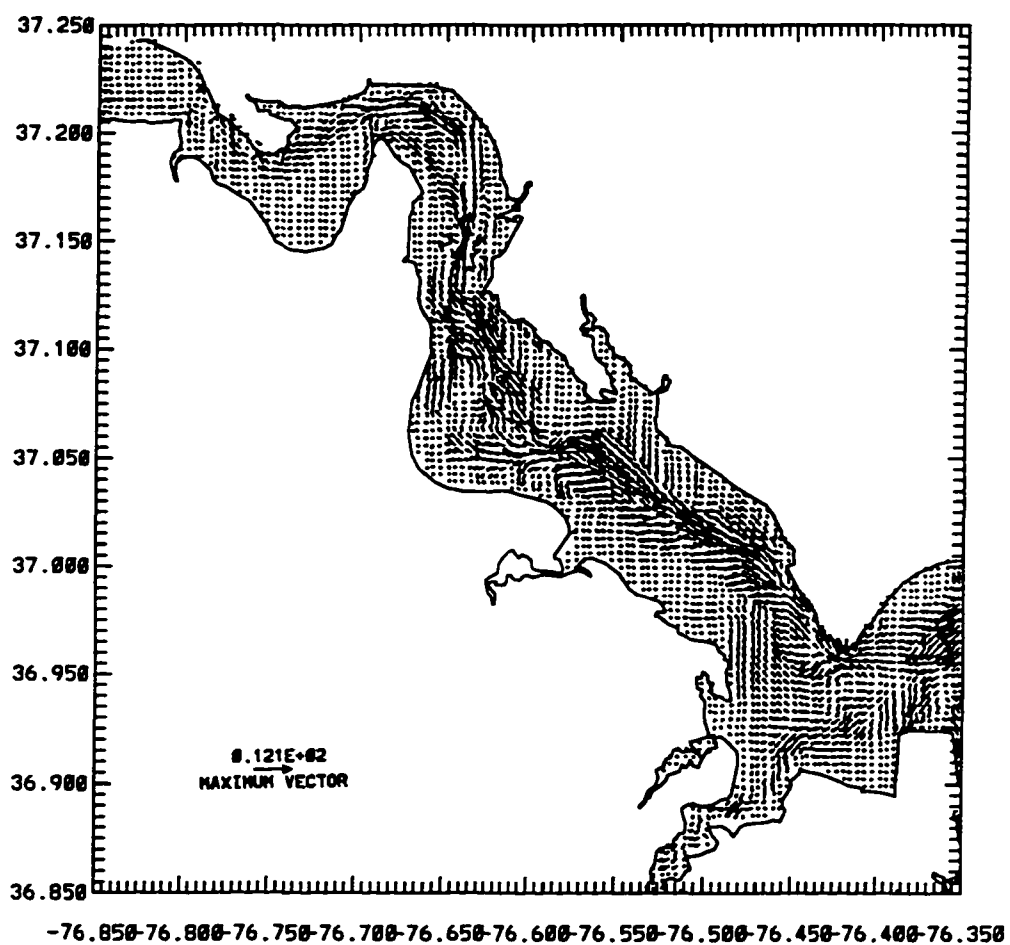


Fig. 56 The Eulerian mean velocity (cm/s) at the bottom layer in the James River

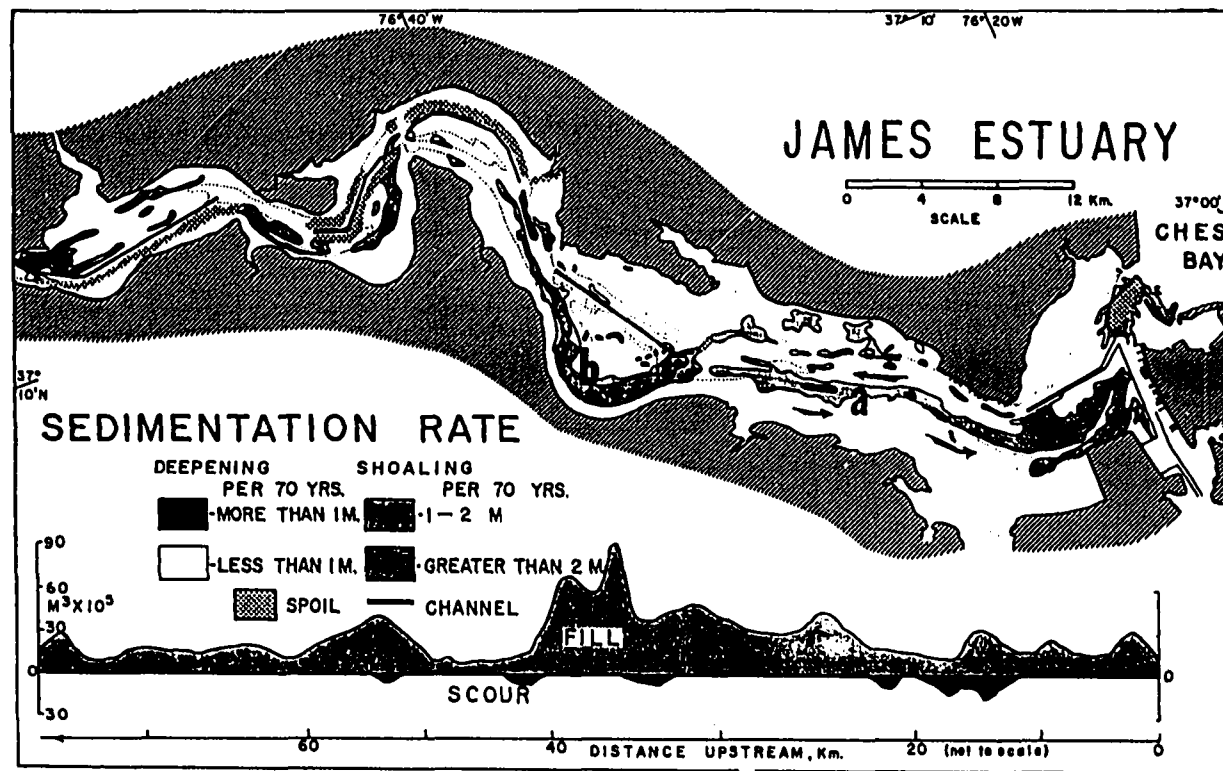


Fig. 57 Patterns of deposition and erosion in the James River estuary determined from depth change over a 70-year period

(from M. M. Nichols, 1972)

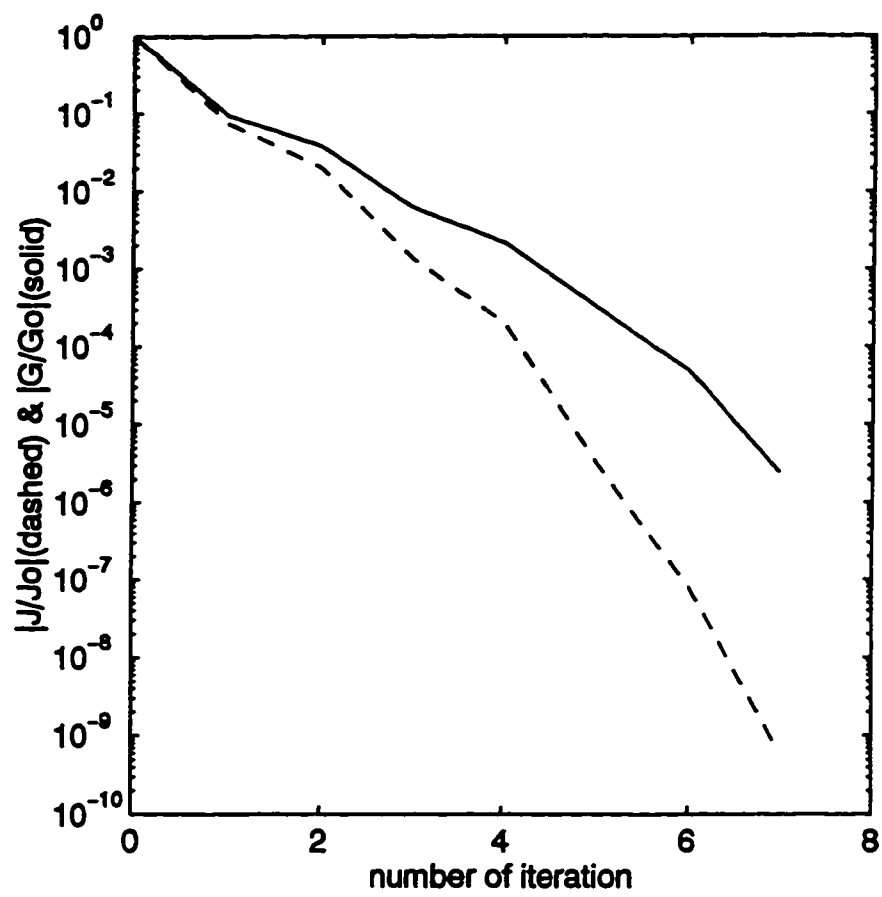


Fig. 58 Variations of  $|J/J_0|$  and  $|\nabla J/\nabla J_0|$  (initial guess I)

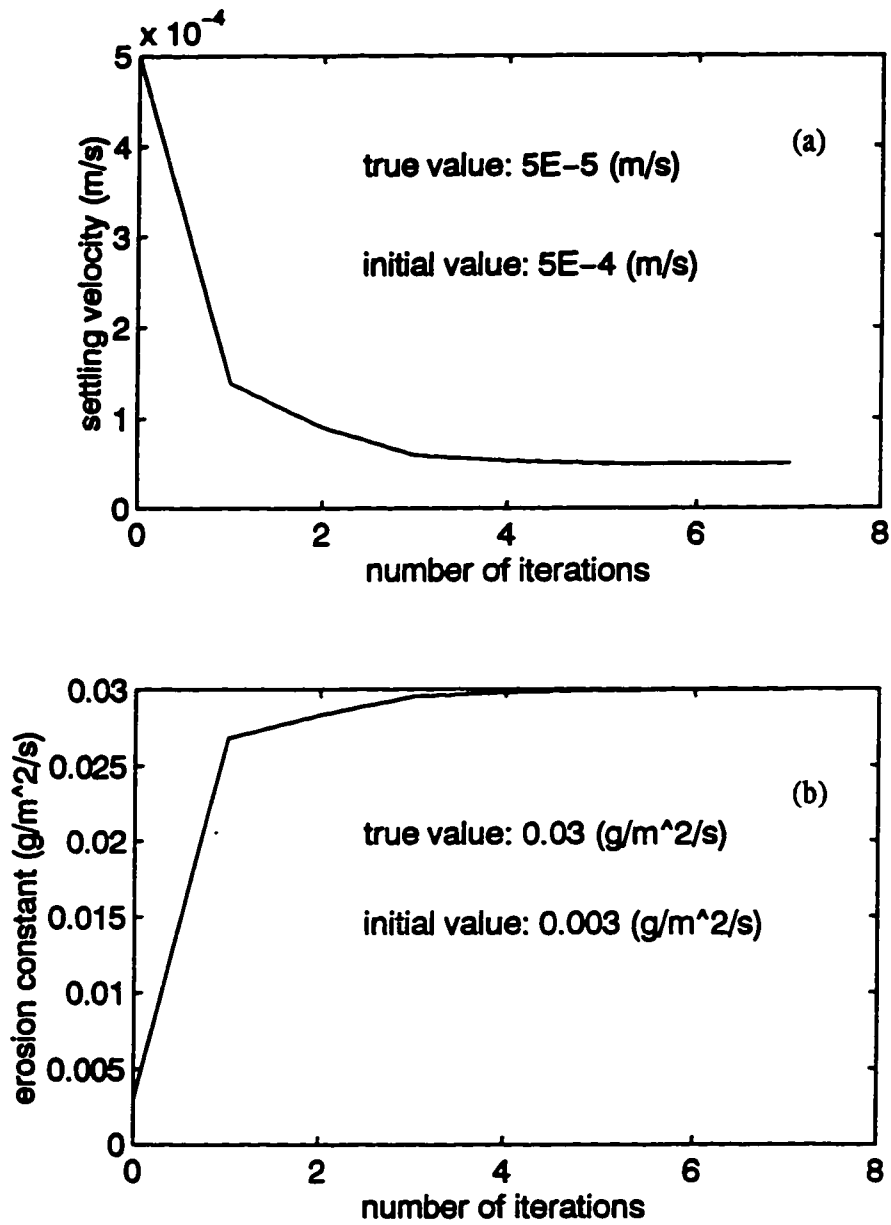


Fig. 59. Variations of settling velocity  $w$ , (a) and erosion constant  $M_o$ , (b)

(initial guess I)

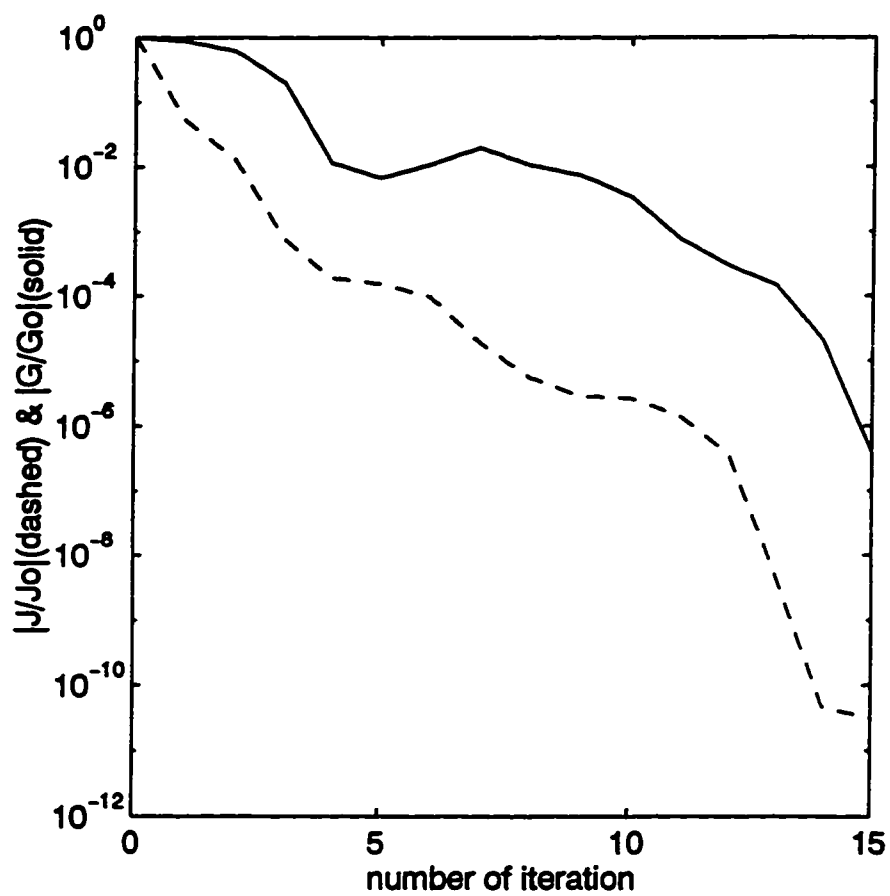


Fig. 60 Variations of  $|J_n/J_0|$  and  $|\nabla J_n/\nabla J_0|$  (initial guess II)

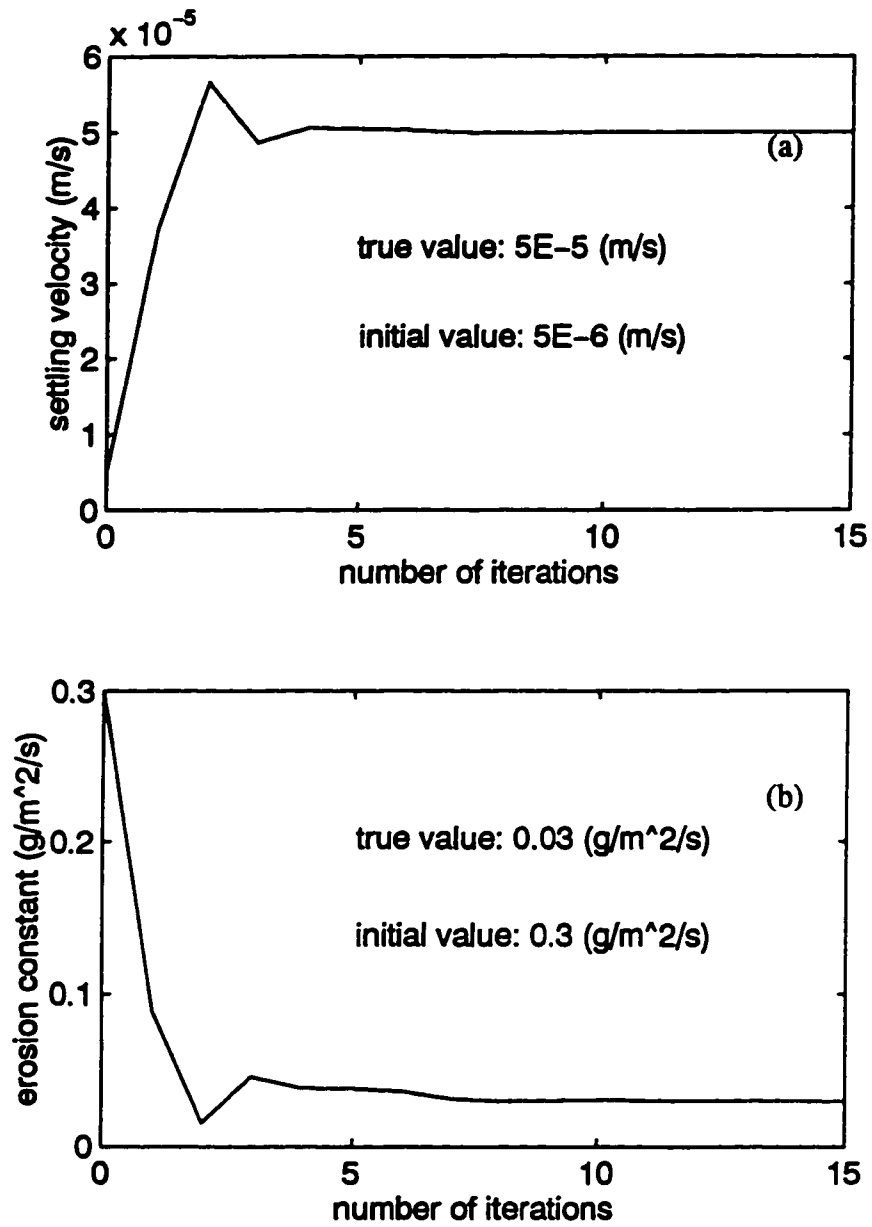


Fig. 61. Variations of settling velocity  $w$ , (a) and erosion constant  $M_o$ , (b)

(initial guess II)

## 6. SUMMARY AND FUTURE STUDIES

In this study, variational inverse models have been developed and tested to identify poorly known parameters in transport problems in estuarine and coastal waters. Three types of parameter identification problems are studied: 1) the Lagrangian mean transport velocity in a long-term transport model; 2) the inflow salinity open boundary condition in a salinity transport model and 3) the settling velocity and erosion rate in a sediment transport model. The variational inverse models were tested by a series of twin experiments using model generated data in an idealized estuary for all three types of problems. The inverse model for the sediment transport problem is also tested in a real prototype, the James River tributary of the Chesapeake Bay. The transport model used in the study is a 3-D advection-diffusion transport equation. The velocity field and vertical diffusivity are calculated from a hydrodynamic model. The VIMS 3-D hydrodynamic/transport model EFDC was used for all the numerical experiments.

The idea of variational inverse methods is to minimize a cost function which measures the error between model predictions and field observations. The optimal values of parameters are retrieved when the cost function is minimized. The gradients of the cost function with respect to control variables are obtained by the adjoint method and the optimization algorithm used in the study is the limited memory quasi-Newton method.

In the long-term advective transport problem, the mean transport flow field is assumed to consist of two parts: the Eulerian mean transport and a correction in the form of a vector potential term. A rough estimate of the Eulerian mean transport can be



calculated from the hydrodynamic model while the vector potential transport is assumed to be unknown and can be identified by the variational inverse model using tracer observations within the computational domain. Twin experiments, conducted in a vertical 2-D idealized estuary, show that the vector potential transport can be retrieved successfully using the inverse model. However, it is found that in the three-dimensional case information for two different tracers is necessary to retrieve the mean transport velocity. Sensitivity studies also show that advective transport is only important in the region where the velocity direction is not parallel to the tangential direction of the tracer contours. When data are not available at every grid cell or the data contains noise signals, reasonable results can still be obtained when a penalty term is appended to the cost function. In real applications, the use of penalty terms requires careful consideration since true solution is unknown. Sensitivity analysis of the penalty weights is suggested.

For the inflow salinity open boundary problem, the maximum inflow boundary value and the recovery time are treated as control variables which are allowed to vary at each open boundary grid cell but remain as constant in the vertical. The inverse model was tested in an idealized 3-D estuary by twin experiments. Results show that the convergence rate for the inverse problem is strongly affected by the scaling of the control variables and the gradients of the cost function. Spatial oscillations appear on the tracer open boundary condition when a penalty term is not included in the cost function. This may be due to the discontinuous characteristic of the recovery time. Such oscillations can be eliminated when a penalty term is appended to the cost function.

For the cohesive sediment transport problem, forward simulation shows that the

sediment transport model can well produce the turbidity maximum zone in estuarine systems. A constant settling velocity  $w_s$  and erosion constant  $M_o$  are estimated by using a variational inverse method. The inverse model is tested in a idealized 3-D estuary and the James River, a tributary of the lower Chesapeake Bay. Identical twin experiments indicate that the inverse model can successfully recover both parameters and the minimization procedure converges within 20 iterations. Sensitivity studies show that when the number of observations is reduced to one, satisfactory results can still be obtained. This may be due to the use of only two control variables in the inverse problem.

Even though some satisfactory results are obtained in present study, future studies should address the following issues. First, in present study all the observations are model-generated, so it would be desirable to use real field observations to test the inverse models for the three types of transport problems to determine how well the inverse models behave in real applications. Scaling of control variables and preconditioning of the minimization problem are two important issues in the minimization procedure. More sophisticated methods might be considered to determine better scaling and preconditioning factors.

Future studies could also address specifics of each of the three problems. For the long-term advective transport velocity problem, the variational inverse model was only tested in an vertical 2-D idealized estuary. Even though theoretically, distributions of two different tracers are required to retrieve a 3-D velocity field, it would be worthwhile to investigate that how well the 3-D transport velocity can be recovered using the variational

inverse model based on single tracer information. It is also important to investigate that what kind of tracer besides salinity would be the best candidate to provide additional information for recovering the 3-D transport velocity field.

For the salinity open boundary condition problem, the inverse model is tested by twin experiments in an 3-D idealized estuary in the present study. It is desirable to test the inverse model in a real prototype estuary. As mentioned in Section 4.5, more practical vertically-varied salinity open boundary conditions should be considered in the future. In the present study, even though the data are sampled along the estuary at a horizontal scale similar to slack water surveys, they are sampled simultaneously. A more realistic sampling strategy is to make all the observations at slack water before flood or before ebb so that the observations distribute similarly to the real slack water run survey both in spatial and temporal domains. Sensitivity studies should be also carried out with respect to 1) the locations of the observation; 2) the duration of the forward simulation required for information changes in the open boundary condition to propagate to the locations of observations; 3) the number of observations required for the inverse model to retrieve true or satisfactory solutions.

For the suspended sediment transport problem, we only consider a simple case in present study, *i.e.*, a single class of sediment. For more practical purposes, multiple classes of sediments should be considered in the forward model. In the present study, the settling velocity, the erosion constant and the critical shear stresses for deposition and erosion were assumed to be uniformly distributed in the whole model domain. In the inverse model, only the settling velocity and the erosion constant are treated as control

variables. The critical shear stresses for deposition and erosion should be included in the variational inverse procedure in future studies. The sediment transport parameters could also be allowed to vary slowly in space and time. In the twin experiments, observations are obtained from 5 locations near the turbidity maximum simultaneously. However, in many realistic cases, we don't know where the turbidity maximum is before we make observations in a large region. So sensitivity tests should be made by subsampling the data in different regions and see how the inverse process responds to different sampling schemes.

## LITERATURE CITED

- Ariathurai, R. and Krone, R. B., 1976: Finite element model for cohesive sediment transport. *Proc. Amer. Soc. Civil Eng.*, 102, 323-338.
- Ariathurai, R. O. and K. Arulanandan, 1978: Erosion of cohesive soils, *J. Hydraulic Division, ASCE*, 104, 279-283.
- Aris, R., 1989: *Vectors, tensors, and the basic equations of fluid mechanics*, 286 pp., Dover Publications, New York.
- Bedford, K. W., O. Kai, C. M. Libicki and R. Van Evra, III., 1987: sediment entrainment and deposition measurements in Long Island sound. *J. Hydraul. Eng.*, 113: 1325-1343.
- Bennett, A., 1992: *Inverse Methods in Physical Oceanography*. Cambridge University Press, 346 pp.
- Bennett, A. and P. McIntosh, 1982: Open ocean modelling as an inverse problem: Tidal theory. *J. Phys. Oceanogr.* 12, 1004-1018.
- Brasseur, P., 1991: A variational inverse method for the reconstruction of general circulation fields in the Northern Bering Sea. *J. Geophys. Res.*, 96, 4891-4907.
- Cancino, L. and R. Neves, 1994: 3D-numerical modeling of cohesive suspended sediment in the Western Scheldt Estuary (The Netherlands). *Netherlands Journal of Aquatic Ecology*, 28, 337-345.
- Cheng, R. T. and V. Casulli, 1982: On Lagrangian residual currents with application in South San Francisco Bay, California. *Water Resour. Res.*, 18, 1652-1662
- Cheng, R. T. and V. Casulli, 1992: Dispersion in tidally-averaged transport equation. In: *Dynamics and Exchanges in Estuaries and the Coastal Zone*, D. Prandle, ed., American Geophysical Union, Washington DC., 409-428.
- Courtier, P., J. N. Thepaut and A. Hollingsworth, 1994: A strategy for operational implementation of 4D-Var, using an incremental approach. *Q. J. R. Meteorol. Soc.*, 120, 1367-1387.
- Das, S. and R. W. Lardner 1991: On the estimation of parameters of hydraulic models by assimilation of periodic tidal data. *J. Geophys. Res.*, 96, 15187-15196.
- Derber, J. C., 1985: The variational 4-D assimilation of analyses using filtered models as constraints, Ph. D. thesis, University of Wisconsin-madison, 142pp.

- Derber, J. C., 1987: Variational four-dimensional analysis using quasi-geostrophic constraints. *Mon. Wea Rev.*, 115, 998-1008.
- Derber, J. C. and A. Rosati, 1989: A global oceanic data assimilation system. *J. Phys. Oceanogr.*, 19, 1333-1347.
- DeVries, J. W., 1985: Field measurements of the erosion of cohesive sediments. *J. Coastal Res.*, 8, 312-318.
- Dyer, K. R., 1979: Estuaries and estuarine sedimentation. In *Estuarine hydrography and sedimentation*, Dyer, K. R. ed., Cambridge University Press, 1-18.
- Dyer, K. R., 1986: *Coastal and Estuarine Sediment Dynamics*. Wiley, New York, 342pp.
- Ezer, T and G. L. Mellor, 1993: Continuous Assimilation of Geosat Altimeter Data into a Three-Dimensional Primitive Equation Gulf Stream Model. *J. Phys. Oceanogr.*, 24, 832-847.
- Evensen, G., 1993: Open boundary conditions for the extended Kalman filter with a quasi-geostrophic ocean model. *J. Geophys. Res.*, 98, 16529-16546.
- Feng, S., R. T. Cheng, and P. Xi, 1986b: On tidal-induced residual current and residual transport: part 1. Lagrangian residual current. *Water Resour. Res.*, 22, 1623-1634.
- Feng, S., R. T. Cheng, and P. Xi, 1986b: On tidal-induced residual current and residual transport: part 2. residual transport with application in South San Francisco Bay, California. *Water Resour. Res.*, 22, 1635-1646.
- Festa, J. F. and D. V. Hansen, 1978: Turbidity maxima in partially mixed estuaries: A two-dimensional numerical model. *Estuarine Coastal Mar. Sci.*, 7, 347-359.
- Galperin, B., L. H. Kantha, S. Hassid and A. Rosati, 1988: A quasi-equilibrium turbulent energy model for geophysical flows, *J. Atmos. Sci.*, 45, 55-62.
- Ghil, M. and P. Malanotte-Rizzoli, 1991: Data assimilation in meteorology and oceanography. *Adv. Geophys.*, 33, 141-265.
- Gibbs, J. R., 1985: Estuarine floc: Their size, settling velocity and density. *J. Geophys. Res.*, 90, 3249-3251.
- Gill, P. E., W. Murray and M. H. Wright, 1981: *Practical optimization*, Academic Press, Inc., New-York, 401pp.
- Glenn, S. M. and W. D. Grant, 1987: A suspended sediment stratification correction for

- combined wave and current flows. *J. Geophys. Res.*, 92, 8244-8264.
- Greenberg, D. A. and C. L. Amos, 1983: Suspended sediment transport and modeling in the Bay of Fundy, Nova Scotia -- a region of potential tidal power development. *Can. J. Fish. Aquat. Sci.*, 40 (sppl. 1), 20-34.
- Hamrick, J. M., 1990: The dynamics of long-term mass transport in estuaries, In *Residual Current and Long-Term Transport*. Cheng, R. T. ed., Springer-Verlag, 17-33.
- Hamrick, J. M., 1992a: A three-dimensional environmental fluid dynamics computer code: Theoretical and Computational Aspects. Virginia Institute of Marine Science, Special Report 317, 63 pp.
- Hamrick, J. M., 1992b: Estuarine environmental impact assessment using a three-dimensional circulation and transport model. In *Estuarine and Coastal Modeling, Proceedings of the 2nd International conference*. Spaulding, M. L. et al, eds., American Society of Civil Engineers, 292-303
- Hamrick, J. M., 1994: Linking hydrodynamic and biogeochemical transport models for estuarine and coastal waters. In *Estuarine and Coastal Modeling, Proceedings of the 3rd International conference*. Spaulding, M. L. et al, eds., American Society of Civil Engineers, 591-608.
- Hamrick, J. M. and T. S. Wu, 1996: Computational design and optimization of the EFDC/HEM3D surface water hydrodynamic and eutrophication models, *Computational Methods for Next Generation Environmental Models*, Delick, G. ed., Society of Industrial and Applied Mathematics, Philadelphia, (in press).
- Harland, Jr., J. and J. J. O'Brien, 1986: Assimilation of scatterometer winds into surface pressure fields using a variational method. *J. Geophys. Res.*, 91, 7816-7836.
- Hayter, E. J., 1983: Prediction of cohesive sediment transport in estuarial waters. Ph.D. Dissertation, University of Florida, Gainesville, Florida.
- Hayter, E. J. and A. J. Mehta, 1986: Modelling cohesive sediment transport in estuarial waters. *Appl. Math. Modelling*, 10, 294-303.
- Hepworth, D. and A. Y. Kuo, 1989: James River seed oyster bed project: physical data report I, 1984-1987. Virginia Institute of Marine Science, Data Report 31.
- Hestenes, M. R. and E. Stiefel, 1952: Methods of conjugate-gradients for solving linear systems. *J. Res. Nat. Bureau of standards*, 48, 409-436.
- Hoffman, R. N., 1986: A four-dimensional analysis exactly satisfying equations of motion.

- Mon. Wea. Rev.*, 114, 388-397.
- Hurlburt, H. E., 1986: Dynamic transfer of simulated altimeter data into subsurface information by a numerical ocean model. *J. Geophys. Res.*, 91, 2372-2400.
- Kuo, A., M. Nichols and J. Lewis, 1978: Modeling sediment movement in the turbidity maximum of an estuary. *Virginia Water Resources Research Center, Bulletin* 111.
- Krone, R. B., 1962: Flume studies of the transport of sediment in estuarial shoaling processes. Final Report, Hydraulic Eng. Lab. and Sanitary Eng. Res. Lab., Univ. California, Berkeley.
- Lardner, R. W., 1993: Optimal control of open boundary conditions for a numerical tidal model. *Computer Methods in Appl. Mechs. & Eng.*, 102, 367-387.
- Lardner, R. W. and S.K. Das, 1994: Optimal estimation of eddy viscosity for a quasi-three-dimensional numerical tidal and storm surge model, *Inter. J. for Numer. methods in Fluids*, 18, 295-312.
- Lavelle, J. W., H. O. Mofjeld and E. T., Baker, 1984: An in situ erosion rate for a fine grained marine sediment. *J. Geophys. Res.*, 89, 6543-6552.
- Le Dimet, F.X. and I. M. Navon, 1988: Variational and optimization methods in meteorology, a review. SCRI Technical Report, FSU, Tallahassee, FL 32306-4052, 100.
- Lee, C. H., 1995: Resuspension behavior of natural estuarine sediments. PhD dissertation, Virginia Institute of Marine Science/School of Marine Science, College of William and Mary, Gloucester Point, VA.
- Li, Y., I. M. Navon, P. Courtier and P. Gauthier, 1993: Variational data assimilation with a semi-Lagrangian semi-implicit global shallow water equation model and its adjoint. *Mon. Wea. Rev.*, 121, 1759-1769.
- Li, Y., I. M. Navon, P. W. Yang, X. Zou, R. Bates, S. Moorthi, R. W. Higgins, 1994: 4-D Variational data assimilation experiments with a multilevel semi-Lagrangian semi-implicit GCM, *Mon. Wea. Rev.*, 122, 966-983.
- Longuet-Higgins, M. S., 1969: On the transport of mass by time-varying ocean current. *Deep Sea Res.* 16, 431-447.
- Liu, D. C. and J. Nocedal, 1989: On the limited memory BFGS method for large scale optimization. *Mathematical Programming*, 45, 503-528.



- Malanotte-Rizzoli, P. and W. R. Holland, 1986: Data constraints applied to models of the ocean general circulation. Part I: The steady case. *J. Phys. Oceanogr.*, 16, 1665-1682.
- Malanotte-Rizzoli, P. and W. R. Holland, 1988: Data constraints applied to models of the ocean general circulation. Part II: The transient, eddy-resolving case. *J. Phys. Oceanogr.*, 18, 1093-1107.
- Marotzke, J and C. Wunsch, 1993: Finding the steady state of a general circulation model through data assimilation: Application to the North Atlantic Ocean. *J. Geophys. Res.*, 98, 20149-20167.
- Marshall, J. C., 1985: Determine the ocean circulation and improving the geoid from satellite altimetry. *J. Phys. Oceanogr.*, 16, 72-86.
- McIntosh, P. and G. Veronis, 1993: Solving underdetermined tracer inverse problems by spatial smoothing and cross validation. *J. Phys. Oceanogr.*, 23, 716-730.
- Mellor, G. L. and T. Yamada, 1982: Development of a turbulence closure model for geophysical fluid problems, *Rev. Geophys. Space Phys.*, 20, 851-875.
- Mehta, A. J., 1981: Review of erosion function for cohesive sediment beds. *Proc. of First Indian Conf. on Coastal Eng.*, Madras, India, 122-130.
- Mehta, A. J., E. J. Hayter, W. R. Parker, R. B. Krone and A. M. Teeter, 1989: Cohesive sediment transport part I: Process description. *J. Hydr. Eng.*, 115, 1076-1093
- Moore, A. M., 1991: Data assimilation in a quasi-geostrophic open-ocean model of the gulf stream region using adjoint method. *J. Phys. Oceanogr.*, 21, 398-427.
- Navon, I. M., 1986: A review of variational and optimization methods in meteorology, in *Festive Volume of the International Symposium on Variational Methods in Geosciences*. Sasaki, Y. K., ed., Elsevier Science Pub. Co. Developments in Geomathematics, Vol.5, 29-34.
- Navon, I. M. and R. de Villiers, 1983: Combined penalty multiplier optimization methods to enforce integral invariant conservation. *Mon. Wea. Rev.*, 111, 1228-1243.
- Navon, I. M. and D. M. Legler, 1987: Conjugate-gradient methods for large-scale minimization in meteorology. *Mon. Wea. Rev.*, 115, 1479-1502.
- Navon, I. M., X. Zou, J. Derber and J. Sela, 1992: Variational data assimilation with an adiabatic version of the NMC spectral model. *Mon. Wea. Rev.*, 120, 1422-1446.

- Navon, I. M., X. Zou, M. Berger, P. K. H. Phua, T. Schlick, and F. X. Le Dimet, 1992a: Numerical experience with Limited Memory Quasi-Newton and truncated Newton Methods, *Optimization Techniques and Applications, Vol 1, Edited by K. H. Phua et al., World Scientific Publishing Co., 1232pp, 33-48.*
- Navon, I. M., X. Zou, M. Berger, P. K. H. Phua, T. Schlick, and F. X. Le Dimet, 1992b: Testing for reliability and robustness of optimization codes for large scale optimization problems, *Optimization Techniques and Applications, Vol 1, Edited by K. H. Phua et al., World Scientific Publishing Co., 1232pp, 445-480.*
- Navon, I. M., 1996: Practical and theoretical aspects of adjoint parameter estimation in meteorology and oceanography, *Dynamics of Atmospheres and Oceans.*
- Nichols, M. M., G. H. Johnson and P. C. Peebles, 1991: Modern sediments and facies model for a microtidal coastal plain estuary, the James estuary, Virginia. *J. Sed. Petr.*, 6, 883-899.
- Nichols, M. M., 1972: Sediments of the James River estuary, Virginia. In *Environmental framework of coastal plain estuaries*, Nelson, B. W., ed., Geological Society of America, Memoir, 196-211.
- Nicolson, J. and B. A. O'Connor, 1986: Cohesive sediment transport model. *J. Hydr. Eng.*, 112, 621-640
- Nocedal, J., 1980: Updating quasi-Newton matrices with limited storage. *Math. Comput.*, 35, 773-782.
- Odd, N. V. M. and M. W. Owen, 1972: A two-layer model for mud transport in the Thames Estuary. *Proceedings, Inst. of Civil Engineers*, London. Paper 75175, 175-205.
- Onish, Y., 1981: Sediment-contaminant transport model. *J. Hydr. Div.*, ASCE, 107, 1089-1107.
- Owen, M. W., 1970: A detailed study of the settling velocities of an estuary mud. Report No. INT 78, Hydraulics Research Station, Wallingford, United Kingdom.
- Owen, M. W., 1977: Problems in the modeling of transport erosion and deposition of cohesive sediments. In *The Sea*, Goldberg, E. D., et al., eds., John Wiley, New York, 515-537.
- Panchang, V. and J. J. O'Brien, 1988: On the determination of hydraulic model parameters using adjoint state formulation. *Modeling Marine Syst.*, I, 5-18.

- Panchang, V. and J. E. Richardson, 1993: Inverse adjoint estimation of eddy viscosity for coastal flow models. *J. Hydr. Eng.*, 119, 506-524.
- Parthenaides, E., 1962: A study of erosion and deposition of cohesive soils in salt water. PhD dissertation, University of California, Berkeley, CA.
- Pearlstein, A. J. and B. N. Carpenter, 1995: On the determination of solenoidal or compressible velocity fields from measurements of passive or reactive scalars, *Phys. Fluids*, 7(4), 754-763.
- Prichard, D.W., 1952: Salinity distribution and circulation in the Chesapeake Bay estuarine system. *J. Mar. Res.*, 11, 106-123.
- Provost, C. and R. Salmon, 1986: A variational method for inverting hydrographic data. *J. Mar. Res.* 44, 1-34.
- Sanford, L. P. and J. P. Halka, 1993: Assessing the paradigm of mutually exclusive erosion and deposition of mud, with examples from upper Chesapeake Bay. *Mar. Geol.*, 114, 37-57.
- Sasaki, Y., 1955: A variational study of the numerical prediction based on the variational principle. *J. Meteor. Soc. Japan*, 32, 262-275.
- Sasaki, Y., 1958: An objective analysis based on the variational method. *J. Meteor. Soc. Japan*, 36, 738-742.
- Sasaki, Y., 1970: Some basic formalism in numerical variational analysis. *Mon. Wea Rev.*, 98, 875-883.
- Schlitzer, R., 1993: Determining the mean, Large-scale circulation of the Atlantic with the adjoint method. *J. Phys. Oceanogr.*, 23, 1935-1952.
- Schroter, J. and C. Wunsch, 1986: Solution of nonlinear finite difference ocean models by optimization methods with sensitivity and observational strategy analysis. *J. Phys. Oceanogr.*, 16, 11855-1874.
- Schroter, J., 1989: Driving of nonlinear time-dependent ocean models by observation of transient tracers: a problem of constrained optimization. In: *Oceanic Circulation Models: Combining Data and Dynamics*, Anderson, D. and J. Willebrand, eds., Kluwer Academic Publisher, 257-285.
- Seiler, U., 1993: Estimation of the open boundary conditions with the adjoint method. *J. Geophys. Res.*, 98, 22855-22870.

- Shanno, D. F., 1978a: Conjugate gradient methods with inexact searches, *Math. Operations Res.*, 3, 244-256.
- Shanno, D. F., 1978b: On the convergence of a new conjugate-gradient method, *SIAM J. Numer. Anal.*, 15, 1247-1257.
- Shanno, D. F. and K. H. Phua, 1980: Remark on algorithm 500 -- a variable method for unconstrained nonlinear minimization. *ACM Transactions on mathematical software*, 6, 618-622.
- Sheng, Y. P. and W. Lick, 1979: The transport and resuspension of sediments in a shallow lake. *J. Geophys. Res.*, 84, 1809-1826.
- Sheng, Y. P., 1986: Modeling bottom boundary layer and cohesive sediment dynamics in estuarine and coastal waters. In: *Estuarine Cohesive Sediment Dynamics*, Mehta, A., ed., 360-400.
- Sheng, Y. P., D. E. Eliason and X. J. Chen, 1992: Modeling three-dimensional circulation and sediment transport in lakes and estuaries. In *Estuarine and Coastal Modeling, Proceedings of the 2nd International conference*. Spaulding, M. L. et al, eds., American Society of Civil Engineers, 105-115.
- Shulman, I. and J. Lewis, 1995: Optimization approach to the treatment of open boundary conditions. *J. Phys. Oceanogr.*, 25, 1006-1011.
- Smedstad, O. M. and J. J. O'Brien, 1991: Variational data assimilation and parameter estimation in the equatorial Pacific Ocean model. *Prog. Oceanogr.* 26, 179-241.
- Spitz, Y. H., 1995: A feasibility study of dynamical assimilation of tide gauge data in the Chesapeake Bay. CCPO Technical Report No. 95-08. PhD dissertation, Old Dominion University, Norfolk, Virginia.
- Sternberg, R. W., K. Krank, D. A. Cacchione and D. E. Drake, 1988: Suspended sediment transport under estuarine tidal channel conditions. *Sediment. Geol.*, 57, 257-272.
- Stommel, H. and F. Schott, 1977: The beta spiral and determination of the absolute velocity field from hydrographic data. *Deep Sea Res.*, 24, 325-329.
- Ten Brummelhuis, P. G. J., A. W. Heemink and H. P. F. Van Den Boorgaard, 1993: Identification of shallow sea models. *Int. J. Numer. Methods Fluids*. 17, 637-665.
- Thacker, W. C., 1987: Three lectures on fitting numerical models to observations. GKSS Forschungszentrum Geesthacht GmbH, Geesthacht, Federal Republic of Germany, External Report GKSS87/E/65, 64 pp.

- Thacker, W. C., 1988: Fitting models to inadequate data by enforcing spatial and temporal smoothness. *J. Geophys. Res.*, 93, 10655-10665.
- Thacker, W. C. and R. B. Long, 1988: Fitting dynamics to data. *J. Geophys. Res.*, 93, 1227-1240.
- Thacker, W. C., 1990: Large least-squares problems and the need for automating the generation of adjoint codes. In: *Lectures in Applied Mathematics*, 26, Allgower, E. L. and K. George, eds., American Mathematical Society, Providence, RI, 645-677.
- Tziperman, E. and W. C. Thacker, 1989: An optimal-control/adjoint-equations approach to studying the oceanic general circulation. *J. Phys. Oceanogr.*, 19, 1471-1485.
- Tziperman, E., W. C. Thacker, R. B. Long and S. M. Hwang, 1992a: Oceanic data analysis using a general circulation model. Part 1: Simulations. *J. Phys. Oceanogr.*, 22, 1434-1457.
- Tziperman, E., W. C. Thacker, R. B. Long, S. M. Hwang and S. R. Rintoul, 1992b: Oceanic data analysis using a general circulation model. Part 2: a North Atlantic model. *J. Phys. Oceanogr.*, 22, 1458-1485.
- Valle-Levinson, A. and K. M. M. Lwiza, 1995: Effects of channels and shoals on the exchange between the lower Chesapeake Bay and the adjacent ocean, *J. Geophys. Res.*, 100, 18551-18563.
- van Leussen, W. and J. M. Cornelisse, 1993: The role of large aggregates in estuarine fine-grained sediment dynamics. In: *Nearshore and estuarine cohesive sediment transport*. Mehta, A. J. ed., American Geophysical Union, 75-91.
- van Rijn, L. C., 1989: The state of the art in sediment transport modeling. In: *Sediment Transport Modeling*, Wang, S. S. Y. ed., ASCE, 13-32.
- Webb, D. J. and A. Moor, 1986: Assimilation of altimeter data into ocean models. *J. Phys. Oceanogr.*, 16, 1901-1913.
- Wunsch, C., 1978: The North Atlantic general circulation west of 50°W determined by inverse methods, *Rev. Geophys.*, 16, 583-620.
- Wunsch, C., 1985: Can a tracer field be inverted for velocity? *Amer. Meteor. Soci.*, 15, 1521-1531
- Yang, W. , I. M. Navon, and P. Courtier, 1996. A new Hessian preconditioning method applied to variational data assimilation experiments using a NASA general

- circulation model, *Mon. Wea. Rev.*, 124, 1000-1017.
- Yu, L. and J. J. O'Brien, 1991: Variational Estimation of the wind stress drag coefficient and the oceanic eddy viscosity profile. *J. Phys. Oceanogr.*, 21, 709-719.
- Zimmerman, J.T.F., 1979, On the Euler-Lagrangian transformation and the Stokes drift in the presence of oscillatory and residual currents, *Deep Sea Res.*, 26A, 505-520.
- Zou, X., I. M. Navon and F. X. LeDimet, 1992a: Incomplete observations and control of gravity waves in variational data assimilation. *Tellus*, 44A, 273-296.
- Zou, X., I. M. Navon and F. X. LeDimet, 1992b: An optimal nudging data assimilation scheme using parameter estimation. *Quar. J. Roy. Meteor. Soc.*, 118, 1163-1186.
- Zou, X., I. M. Navon, M. Berger, K. H. Phua, T. Schlick and F. X. LeDimet, 1993a: Numerical experience with limited-memory quasi-newton and truncated Newton methods. *SIAM J. Optimization*, 3, 582-608.
- Zou, X., I. M. Navon and J. Sela, 1993b: Control of gravitational Oscillations in Variational Data Assimilation, *Mon. Wea. Rev.*, 121, 272-289.
- Zou, J. and G. Holloway, 1995: Improving steady-state fit of dynamics to data using the adjoint equation for gradient preconditioning, *Mon. Wea. Rev.*, 123, 199-211.
- Zou, J., W. W. Hsien, and I. M. Navon, 1995: Sequential open boundary control by data assimilation in a limited area model, *Mon. Wea. Rev.* , 123, 2899-2909.

**VITA****Zhaoqing Yang**

Born in Zhanjiang, a southern city in the People's Republic of China, October 21, 1960. Earned B.S. in Mathematics and Fluid Mechanics from Zhongshan University, P. R. China in 1982, M.S. in Physical Oceanography from the Second Institute of Oceanography, P. R. China in 1986. Worked in the Estuarine and Coastal Division of the Institute from 1986 to 1990 as an assistant researcher and then came to United States in the fall of 1990. Earned M.S. in Ocean Engineering from the University of Rhode Island in 1992. Entered the Ph.D program in the Virginia Institute of Marine Science, College of William and Mary in the fall of 1992.